THE HONG KONG POLYTECHNIC UNIVERSITY

DEPARTMENT OF
MECHANICAL ENGINEERING

DIRECT FORCE MEASUREMENTS OF A TWO-DIMENSIONAL AIRFOIL UNDERGOING DYNAMIC STALL

KIT YING KEZIA TSANG

A THESIS SUBMITTED IN PARTIALFULFILLMENT OF THE
REQUIREMENTS FOR THE DEGREE OF

MASTER OF PHILOSOPHY

MARCH 2006

CERTIFICATE OF ORGINALITY

I hereby declare that this thesis is my own work and that, to the best of my knowledge and belief, it reproduces no material previously published or written, nor material that has been accepted for the award of any other degree or diploma, except where due acknowledgement has been made in the text.

Tsang, Kit Ying Kezia

DEDICATION

To my family.

ABSTRACT

A direct force measurement technique is designed to investigate experimentally a two-dimensional airfoil undergoing dynamic stall at low Reynolds number (Re). Two servomotors and two piezoelectric load cells are installed at each end of a NACA 0012 airfoil mounted horizontally across the test section in a wind tunnel. Thus designed, the servomotors can pitch the airfoil sinusoidally about its one-quarter chord at various mean angles of attack and amplitudes, while the load cells give the force responses of the airfoil during oscillations in two directions in the plane normal to the airfoil axis. All experiments are carried out at a Re based on the airfoil chord of $7.7 \text{x} 10^4$. Total five cases covering the range of airfoil pre-stall, light stall, and deep stall are tested. They are Case 1: $\alpha = 0^\circ + 5^\circ \sin(\omega t)$ and Case 2: $\alpha = 5^\circ + 5^\circ \sin(\omega t)$ in the pre-stall region, Case 3: $\alpha = 10^\circ + 5^\circ \sin(\omega t)$ in the light-stall region, and Case 4: $\alpha = 10^\circ + 10^\circ \sin(\omega t)$ and Case 5: $\alpha = 15^\circ + 10^\circ \sin(\omega t)$ in the deep-stall region. Four relatively low reduced frequencies, $k = 0.005$, 0.01, 0.02, and 0.04 are tested for each case. Flow visualization is also performed using the same airfoil in a water tunnel at the same Re and k.

Phase-averaged lift of the airfoil undergoing dynamic stall is presented. Hysteresis loops of the lift occur both when the airfoil is being pitched to exceed its static stall limit and when it is still within its static stall limit. It is observed that both the dynamic stall angle and the maximum lift increase with increasing k at the same pitching mean angle of attack and pitching amplitude for the stall cases. Flow visualization pictures at various phases of different oscillations are also presented.

The time series of the lift response signals are analyzed using fast Fourier transform and wavelet analysis. Nonstationary and nonlinear characteristics of the lift time series of both the light-stall and deep-stall cases are observed.

PUBLICATIONS ARISING FROM THE THESIS

Tsang, K.K.Y., So, R.M.C., Leung, R.C.K, and Wang, X.Q. Dynamic Stall Behavior from Unsteady Force Measurements. *AIAA Journal*, Submitted in June 2006.

ACKNOWLEDGEMENTS

My sincere thanks to my supervisor Professor Ronald So for his expertise, understanding, support and guidance, and for stretching his patience for me over the past years. A clear path of research he has guided me through, and confidence he has given me on the significance of my work. Discussions with Professor So have always inspired me not only on my research but also life in general.

I am grateful to Dr. Randolph Leung for being my co-supervisor, a brother and a friend. His technical knowledge and constant encouragement are always appreciated.

I would like to thank Dr. See Chun Kot of The Hong Kong University of Science and Technology and Professor Earl Dowell of Duke University for serving on the Examination Committee, and Professor K.Y. Fung for serving as the Committee Chairman.

I would like to thank Lily Tam for listening to my endless requests of help and for her care and encouragement. Chatting with her is always a relief from the stress of work. I would also like to thank the technicians at the Project Laboratory, Mr. Ng, Mr. Lam, Mr. Chan, Mr. Shum, Mr. Wu, and Mr. Mo, and Mr. Tang from Acoustics Lab, and their supervisor Mr. Lo for all their assistance on my experimental setup. Without them, the experiments would not have been possible.

My appreciation would also go to my friends from X-block; Sze-Hing, Ah Him, Dorothy, Joanna, Marc, Dan Dan, Carrie, and Jenny. They have made our office a fun place to work. I will always miss hanging with you guys.

Special thanks to Yu Kin Fung and Kenneth. I still remember it was the third day of Chinese New Year. It was 7°C in the lab and Kenneth came in to help and had just returned to HK on that day. Fung, thanks again for spending hours in the lab with me and all the help in running the tests and as my two-time Trailwalker teammate.

Thanks to my family and extended family. Your love and support of my study (both undergraduate in the US and post-graduate here in HK) is always deeply appreciated.

Funding support from the Research Grants Council of the HKSAR Government given under Grant Nos. PolyU5272/04E is gratefully acknowledged.

TABLE OF CONTENTS

LIST OF FIGURES

LIST OF TABLES

NOMENCLATURE

a	speed of sound
a	pitch axis location relative to the mid-chord of the airfoil
b	half chord
c	airfoil chord
C_D	drag coefficient
C_L	lift coefficient
C_{Lmax}	maximum lift coefficient
C_M	moment coefficient
C_N	normal force coefficient
D_{net}	calculated true drag
E_a	measured voltage of hotwire anemometer
E_{corr}	temperature corrected voltage of hotwire anemometer
f	pitching frequency
f_{eq}	equivalent Fourier frequency
f_n	natural frequency
f_n	normalized equivalent Fourier frequency
h	vertical position of the hotwire probe
k	reduced frequency
L_{net}	calculated true lift
M	Mach number
P_n	normalized power spectral density
Re	Reynolds number
s	span
s	scaling factor of continuous wavelet transform
T	period of one cycle of oscillation
T_0	ambient reference temperature
T_a	ambient temperature during measurement
T_w	sensor temperature
t_n	normalized time
U	streamwise flow velocity of the wake
U_1, U_2	orthogonal velocity components in the wire coordinates
U_{ms}	streamwise flow velocity of the wake measured at mid-span

U_n	normalized flow velocity of the wake
U_∞	free stream velocity
V	transverse flow velocity of the wake
$w(t)$	data to be analyzed with continuous wavelet transform
X, Y, Z	coordinates of load cell reference frame
x, y, z	coordinates of airfoil trailing edge at mid-span at $\alpha = 0°$

Greek Symbols

α	angle of attack
α_{ss}	static stall angle
α_{mean}	mean angle of attack of oscillation
α_{amp}	amplitude of oscillation
ρ	air density
τ	translating factor of continuous wavelet transform
ν	kinematic viscosity
ω	angular frequency
$\psi(t)$	mother wavelet of continuous wavelet transform

CHAPTER 1 INTRODUCTION

When an airfoil undergoes a rapid increase in the angle of attack, large overshoots in lift, drag, and pitch moment take place. Loss of lift occurs, and lift stall and moment stall are delayed to higher angles of attack compared to the quasi-steady stall values. This phenomenon is referred to as “dynamic stall”. When dynamic stall occurs, the flow separates from the airfoil, and the loss of lift is more abrupt and more persistent than that of static stall. Once the flow is separated, reattachment takes place only when the airfoil is pitched down to an angle of attack, α, much lower than the static stall angle, α_{ss}, or when the airfoil is being pitched up again. Owing to this large hysteresis in the flow development, dynamic stall is accompanied by a large phase variation in the unsteady air load. Hence, the value of the unsteady air load is dependent on whether the flow is separating, fully separated, or reattached (Leishman, 2000).

Due to increasing demand on performance, there is enhanced interest in making use of the large excursion of maximum lift to improve maneuverability of fighter aircraft (Carr, 1998). Conversely, the nonlinearities in air load associated with dynamic stall can induce a torsional air load, and a vibration and control load on the airfoil. This phenomenon is called “stall flutter”. Severe structural damages could result and the consequence could be catastrophic. Therefore, dynamic stall is one of the limiting factors governing helicopter rotor performance. In view of this, an understanding of the characteristics of dynamic stall is necessary for the sake of safety and for the enhancement of maneuverability of aircraft and rotorcraft.

A relatively more in-depth understanding of dynamic stall and its associated process could be achieved by first attempting to explain the dynamic stall process, then surveying the literature on past experimental studies and the techniques used to measure the stall phenomena and the associated force and moment. With this background, work necessary to add further understanding to the dynamic stall phenomenon could be identified. Therefore, the objectives of the present study can be defined.

1.1 Dynamic Stall Process

In past decades, much progress has been made in analyzing and predicting dynamic stall and the associated stall process. It is believed that dynamic stall is related to the formation, development, and shedding of a leading-edge vortex. However, before the vortex could affect the pressure distribution around the airfoil, the process of dynamic stall has already begun (Carr, 1998).

The dynamic stall process is briefly described in Figure 1.1. Broadly speaking, the process could be classified into five stages. During Stage 1, the airfoil is pitched to exceed α_{ss}. Flow reverses near the surface towards the trailing edge of the airfoil and progresses up to the leading edge. During Stage 2, the flow separates from the surface starting from the leading edge and a dynamic stall vortex forms near the leading edge and moment stall occurs. During Stage 2-3, the vortex moves streamwise and provides additional lift on the airfoil. During Stage 3-4, lift stall occurs when the vortex is shed behind the airfoil and the flow is fully separated from the surface of the airfoil. Finally, during Stage 5, when the airfoil is being pitched down, the flow reattaches to the airfoil surface at an angle below α_{ss} (Carr, 1977, Leishman, 2000).

It has been shown that three primary unsteady phenomena cause the delay in the onset of flow separation under unsteady conditions. When an airfoil undergoes pitching motion, the unsteadiness of the circulation that is shed into the wake induces a reduction in the lift and a decrease in the adverse pressure gradient. Further reduction in the adverse pressure gradient is produced by the induced-camber effect of the kinematics of positive pitch rate. With the occurrence of flow reversal in the absence of a significant flow separation, flow separation is delayed to a higher α and so is the onset of dynamic stall. A significant lag is also observed on flow reattachment under unsteady conditions. This is due to the time lag of the reorganization of the fully separated flow to reattach, and the reverse kinematic "induced camber" effect by the negative pitch rate (Leishman, 2000).

1.2 Aerodynamic Measurements of Dynamic Stall

Experimental investigations have been conducted to examine the aerodynamics associated with dynamic stall and its delay, as well as the influence of stall parameters on the dynamic stall process and its characteristics (Carr, 1998; Carr *et al.*, 1977; McAlister *et al.*, 1978). Some of the more important parameters are: airfoil geometry, mean angle of attack, α_{mean}, and the amplitude of oscillation, α_{amp}, reduced frequency, $k = \pi fc/U_\infty$, Reynolds number, $\mathrm{Re} = U_\infty c/\nu$, and Mach number, $M = U_\infty/a$, where f is the pitching frequency in Hz, c is the airfoil chord length, ν is the kinematic viscosity, a is the speed of sound and U_∞ is the free stream velocity.

Most experimental studies have opted to investigate forced-oscillating airfoils in two-dimensional (2-D) flow field in a wind tunnel (or occasionally in a water tunnel) to simulate the dynamic stall phenomenon. Some of the commonly used experimental techniques to study dynamic stall behavior include measuring the surface pressure using pressure transducers, measuring the velocities of the flow around the airfoil using constant temperature anemometry (CTA), and examining the flow field around the airfoil using particle image velocimetry (PIV). The force and moment responses of the oscillating airfoil are often computed from the quantities measured using the aforementioned techniques. In other studies, researchers used a combination of different measuring techniques to study the various characteristics of the dynamic stall process. A few representative studies using these techniques are briefly described below.

1.2.1 Pressure Measurements Using Transducers

Numerous researchers studied dynamic stall behavior by obtaining surface pressure data from an oscillating airfoil using pressure transducers flush-mounted on the airfoil model surface. The data thus obtained were used to calculate the pressure coefficient and occasionally force coefficients were also deduced by integrating the pressure distribution around the airfoil.

Walker *et al.* (1985) examined the unsteady aerodynamics surrounding a pitching airfoil. The parameters studied were Re and the non-dimensional pitch rate of the airfoil. Miniature pressure transducers were installed close-coupled to the surface ports. The transducer signals acquired were amplified and the pressure data were used to calculate the pressure and lift coefficients. The authors found that increasing the pitch rate increased the maximum lift coefficient, C_{lmax}, and the angle of attack, α, at which C_{lmax} occurred. Furthermore, the increase was found to be more prominent at lower Re.

Conger and Ramaprian (1994) measured the unsteady pressure over a NACA 0015 airfoil in an open-surface water channel in the Re range of $5.2\text{x}10^4$ to $2.2\text{x}10^5$. Pressure data were obtained using a differential diaphragm-type pressure transducer which was connected between a reference static pressure tap and a surface pressure port via a scanning valve. Both steady-state experiments and pitch-up tests were performed. Aerodynamic force and moments were calculated by integrating the measured surface pressure distribution. It was found that the magnitude of the measured pressure and aerodynamic force coefficients were much larger than those obtained from earlier studies at similar Re and pitch rates. The authors conjectured that the relatively high freestream turbulence in the water channel was the cause of this noted discrepancy.

Albertson *et al*. (1987) conducted surface pressure measurements on a NACA 0015 airfoil pitching at a constant pitching rate. Enhanced flow visualization images were also taken in order to study the development of the dynamic stall vortex (DSV) in conjunction with the surface pressure levels. Lift coefficients were computed from the pressure measurements. The authors showed that the DSV did not enhance the instantaneous lift. Later rapid growth of the stall vortex indeed occurred with a decrease in lift and the detachment of the DSV was found to correspond to a simultaneous decrease in the pressure drag of the airfoil.

Piziali (1994) performed a comprehensive experimental investigation of the pressure distribution over a cantilever wing undergoing pitching motions. Miniature strain gage temperature-compensated differential pressure transducers were used and both 3-D and 2-D wing configurations were tested. A complete set of data including 3-D static and dynamic pressure distribution, micro-tuft surface flow visualization, 2-D airfoil data from the same model and installation were archived. Cycle-averaged lift, drag and pitching moment coefficients versus angle of attack obtained from the instantaneous pressure data for the 3-D wing and the 2-D airfoil were also reported.

1.2.2 Velocity Measurements Using Constant Temperature Hotwire Anemometry

Hotwire anemometry or hot-film gages were employed by many researchers to measure the flow velocity around the airfoil and in the airfoil wake. Analysis of the velocity signals helped to determine the events and process of boundary layer separation during dynamic stall. Some of the anemometry studies also used the velocity information to calculate vorticity distribution around an oscillating airfoil and thus a deduction of the lift and drag.

Panda and Zaman (1992) carried out phase-averaged vorticity measurements to examine the evolution and the shedding of DSV. Measurements of the axial and transverse velocity components over many oscillation cycles were made using a single or a crossed hotwire probe mounted on a traversing mechanism. The velocity components were captured both in the wake and on the suction side of the airfoil. The signals from the crossed hotwire probe acquired at various chordwise and transverse locations were processed to get the phase-averaged distributions of velocity components and from which the spanwise vorticity component was calculated. The authors also presented the method of estimating the unsteady lift component from the vorticity flux measured in the wake. From the flow field measurements, along with flow visualization results, the authors found that an intense vortex of opposite sense formed near the trailing edge (TEV) just when the DSV was shed. The DSV and TEV grew in size and formed the shape of a "mushroom" as they were convected away from the airfoil. It was found that the large lift occurred during the formation of the DSV was associated with an accumulation of positive vorticity on the upper surface of the airfoil and a depletion of positive vorticity in the wake. They also found that variation of oscillation amplitude for a given *k* did not change the shape of the lift hysteresis loop.

Martin *et al.* (1974) used multiple measuring techniques to study the effects of *k*, Re, and amplitude variation on the dynamic stall process of an oscillating airfoil. Several single hot-wire probes mounted at various chordwise locations gave qualitative information of the flow near the surface. Miniature pressure transducers were used to measure the pressure difference between the tunnel static pressure and the surface pressure at different chord locations of the airfoil. Normal force coefficients were then calculated by integrating the measured pressure distribution. Flow visualization studies using smoke were also carried out to help interpret the velocity and pressure measurements. The authors reported that the angle for stall initiation decreased with increasing Re, while the angle at which maximum lift occurred increased with increasing Re. The hotwire data further showed the occurrence of a short bubble during both the upstroke and downstroke of the pitching and the angle of bubble passage decreased with increasing Re. The authors further found that maximum pressure and maximum velocity at the leading edge did not always occur at the same angle of attack. Indeed, the occurrence of maximum velocity at the leading edge usually preceded that of maximum pressure. From the pressure data and flow visualization, the authors also concluded that increasing k increased the stall delay.

Carr *et al.* (1977) carried out experiments using miniature hotwire anemometer probes and differential pressure transducers. Pressure data obtained were used to calculate normal force and pitching moment and the hotwire signals were analyzed to determine the onset of boundary-layer flow reversal, separation, and the passage of the DSV over the upper surface of the airfoil model. Flow visualization using smoke was also performed to deduce quantitative measurements of the location, size and movement of the DSV. Tufts were attached at five chordwise stations to provide a separate set of indicators about the activities within the boundary layer as a complement to the flow visualization result. The authors presented chronologies of the events for a full cycle of oscillation for a NACA 0012 airfoil, a cambered airfoil, and a sharp leading-edge airfoil. It was shown that the overall character of the normal force coefficient, C_N, and the moment coefficient, C_M, versus α for the trailing-edge stall was qualitatively similar for the NACA 0012 and the cambered airfoil. However, flow reversal and stall inception were fundamentally different for the two airfoils. Furthermore, the leading-edge bubble bursting for the sharp leading-edge airfoil was both qualitatively and quantitatively different from the stall types on the NACA 0012 airfoil and the cambered airfoil. Effects of other parameters on the dynamic stall process were also presented.

1.2.3 Flow Field Studies using Particle Image Velocimetry

Since hotwire anemometry technique can only provide point measurements, a technique that could yield field measurements would be most helpful in the study of the flow field around a stall airfoil. Wernert *et al.* (1996) investigated the dynamic stall process on a pitching NACA 0012 airfoil using particle image velocimetry (PIV). A double oscillator Nd:YAG pulse laser was used to generate laser pulses with a typical time delay of about 12 μs between two pulses. Olive oil droplets of size about 1μm mean diameter were injected into the flow. Photographic recordings were taken during the upstroke and downstroke motion of the airfoil at intervals of 1° and a rate of about one picture per second. The results showed the occurrence of a thin reverse-flow layer on the upper side of the airfoil when the flow was still attached. Small-scale vortices within the large DSV, strong non-reproducibility of the separated flow field during downstroke, and progressive reattachment of flow from the leading edge to the trailing edge were observed.

Oshima and Ramaprian (1992) presented the results of measurements of the instantaneous velocity and vorticity field of a NACA 0015 airfoil pitching at constant angular velocity about its quarter-chord axis in a 2-D flow using a PIV technique. Fluorescent particles of 2 μm diameter were used to seed the entire water channel. An argon laser was used to generate a thin light sheet to illuminate the mid-span section of the suction side of the airfoil. Instantaneous multiple-exposure pictures of the illuminated particles were taken at intervals of about 0.75˚ in pitch. Separate pictures of the forward, middle and aft regions, each covering an effective area of 12 cm x 12 cm of the flow field were taken. Each film was scanned using a 2-D traverse to obtain the velocity vectors over the 2-D flow field, from which the instantaneous vorticity field and streamlines were computed. From the PIV data, it was observed that the increase in lift experienced by a pitched airfoil was due to the production and concentration of vorticity close to the surface of the airfoil and the growth of the DSV was simply due to the conglomeration of all shear-layer vorticities.

1.3 Need for Direct Force Measurement

When an airfoil is oscillating sinusoidally as in most dynamic stall studies, energy is constantly input to the airfoil by the pitching mechanism. Since the motion is periodic, many of the studies investigate the phenomenon by examining the phase-averaged values of the lift. The implicit assumption is that the measured lift is time-stationary in a periodic sense. However, this assumption might not be able to stand up to scrutiny. Besides, despite the impressive progress made on the understanding of the dynamic stall phenomenon, scant attention has been placed on the investigation of the frequency content of the lift signal of a 2-D airfoil undergoing dynamic stall, which is associated with the energy content of the structure. Hence, the present study intends to examine the frequency content of the unsteady lift signal and the stationary nature of the aerodynamic responses of the pitching airfoil. To achieve this, it is most desirable to measure the lift directly.

In Section 1.2, various techniques used to measure lift are discussed. However, they are indirect methods whereby force information is deduced either from the measured pressure distribution or from the measured vorticity distribution. Since force and moment computation requires integration of the pressure distribution, the accuracy of such computation is highly dependent on the preciseness of the integration technique (McAlister *et al*., 1978) and the correctness of the pressure data. Any error in the pressure data also becomes a source of error in the force deduction. Besides, viscous shear, which plays an important role on aerodynamic responses at low Re, are not measured by pressure transducers; the accuracy of aerodynamic force data thus obtained are questionable. Vorticity in the flow is usually deduced from velocity measurements obtained from hotwire anemometry or laser Doppler velocimetry. These are point measurements. Therefore, force calculated from vorticity data is also affected by the same shortcomings as those outlined above. Consequently, it is not appropriate to use these data to deduce force power spectra and study their frequency contents and the possible occurrence of nonlinear behavior.

1.3.1 Direct Force Measurement Techniques

Most lift data is measured indirectly in the literature, i.e. lift is calculated from the measured quantity of the experiments, be it surface pressure or flow velocity. Integration of the measured quantity is required to obtain lift due to the discrete nature of the measurements. Irrespective of the frequency content of the measured signal, when integration is invoked, high frequency components of the signal are filtered out and only low frequency components are left in the resultant force signal. Therefore, certain important information concerning the behavior of the fluctuating force could be lost. It is for this reason that researchers have to resort to direct force measurement techniques to study dynamic stall and the associated linear/nonlinear, stationary/nonstationary behavior.

Compared to indirect measurement techniques, direct force measurement technique can better capture the actual aerodynamic responses of the test model. Besides, the frequency content of the measured signal is only limited by the frequency response of the measuring equipment, such as sensors and amplifiers. The aerodynamic response can be recorded as an analog or a digitized signal. Of course, the resolvable frequency range of the digitized signal will depend on the sampling rate. Either way, the raw force signal could be stored for later analysis without lost of information, such as the frequency content of the force power spectra related to the stall dynamics.

In the past, direct measurements of the mean and fluctuating forces acting on rigid and elastic structures are carried out using one of the several available methods, such as pressure transducers or balance method for mean force measurements, and resistance-wire strain gage for fluctuating force measurements. The strain gage technique has one drawback though, that in order to ensure reliably measurable strain, the structure needs to be sufficiently flexible. This conflicts with the requirement that the structure has to be rigid, or there is a danger of the results being contaminated by the structural dynamics.

With the development of piezo-electric transducers, this technique has been used by researchers to measure fluctuating pressure and force. The first study using piezo-electric load cell to directly measure the spanwise-averaged Strouhal force on circular cylinders was reported by Richter and Naudscher (1976). Their study shows that the technique can resolve the mean and root mean square force in both the lift and drag direction and together with their dominant frequencies. Thus, the experiment is able to show that the dominant drag force frequency is twice that of the lift. The measurements not only give the mean and fluctuating forces but also the statistics and the frequency content of the force signals. The technique was later used to measure the buffeting force on cylinders (Savkar *et al*. 1980 and So and Savkar 1981). They showed that the full spectra of the fluctuating lift and drag could be measured correctly. This technique was further extended to study the fluctuating forces on cylinder arrays (Lam *et al*. 2003) and on wavy cylinders (Lam *et al*. 2004). Improvement of the technique to measure local fluctuating forces on 2-D and 3-D cylinders has been made by Sin and So (1987) and the modified technique has been used to study the correlation between unsteady forces and wake flow of finite cylinder in a cross flow (Baban *et al*. 1989).

Recently, the technique has also been extended to study dynamic stall by measuring the unsteady force directly using piezo-electric force cells. Panda and Zaman (1994) attempted to measure directly the unsteady forces acting on an oscillating airfoil but they were only successful at small amplitude oscillations around $\alpha = 0^\circ$. The technique was applied to study insect flight behavior. In order to study the aerodynamic basis of insect flight, Dickinson *et al.* (1999) designed and built a dynamically scaled model of the fruit fly, equipped with a force cell at the base of one wing. Thus designed, the test model was capable of yielding direct measurements of the time history of the aerodynamic forces. Driven by an assembly of six computer-controlled stepper motors attached to a wing gearbox via timing belts and coaxial drive shafts, each of the two wings was capable of rotational motion about three axes. Using this model, the authors successfully measured the time-dependent force and studied the three interactive mechanisms of insect flight, namely delayed stall (dynamic stall), rotational circulation, and wake capture.

The fruit fly model proved that force cells could be used to measure the unsteady forces acting on wings undergoing dynamic stall. In other words, the force cell technique could be used to study dynamic stall where the amplitude of oscillations is not small. The present study attempts to apply the technique to study dynamic stall where the mean pitching angle varies from zero to 15˚ and the pitching amplitude could be as large as 10˚. If successful, this study represents a significant improvement over that of Panda and Zaman (1994) in terms of the range of the pitching angle and amplitude of the oscillations.

1.4 Scope of the Present Study

From the brief review of the experimental work carried out on dynamic stall, it is clear that direct measurement of the aerodynamic forces on an airfoil undergoing pitching oscillation and dynamic stall could shed further light on the stall process. This understanding could be augmented by visualization studies of the stall phenomenon under the same aerodynamic conditions. Therefore, the objectives of the present studies can be identified as:

1. to improve on the direct force measurement technique so that it could be used in wind tunnel testing of a pitched airfoil undergoing periodic pitching oscillation and dynamic stall,
2. to perform flow visualization on the same airfoil to identify the different stages of dynamic stall and corroborate these findings with the force measurements and,

3. to analyze the force data to identify the source of nonlinear behavior in an airfoil undergoing periodic pitching oscillation and dynamic stall.

1.5 Organization of the Thesis

Chapter 2 introduces in detail the direct force measurement technique and its setup, and the setup of the flow visualization experiments. Chapter 3 describes the test conditions of the experiments and the selection of test conditions. Methods used to analyze the experimental data as well as the flow visualization results are also described. Chapter 4 discusses the results of the force measurements, and the results of the flow visualization experiments. Due to the voluminous amount of data collected, careful selection has to be made to bring out the salient points of the present study. Since lift is the most telling of all the data collected, the present analysis will therefore focus on the power spectra of the lift signals only. Chapter 5 details the conclusions derived from the present study and some suggestions for future work.

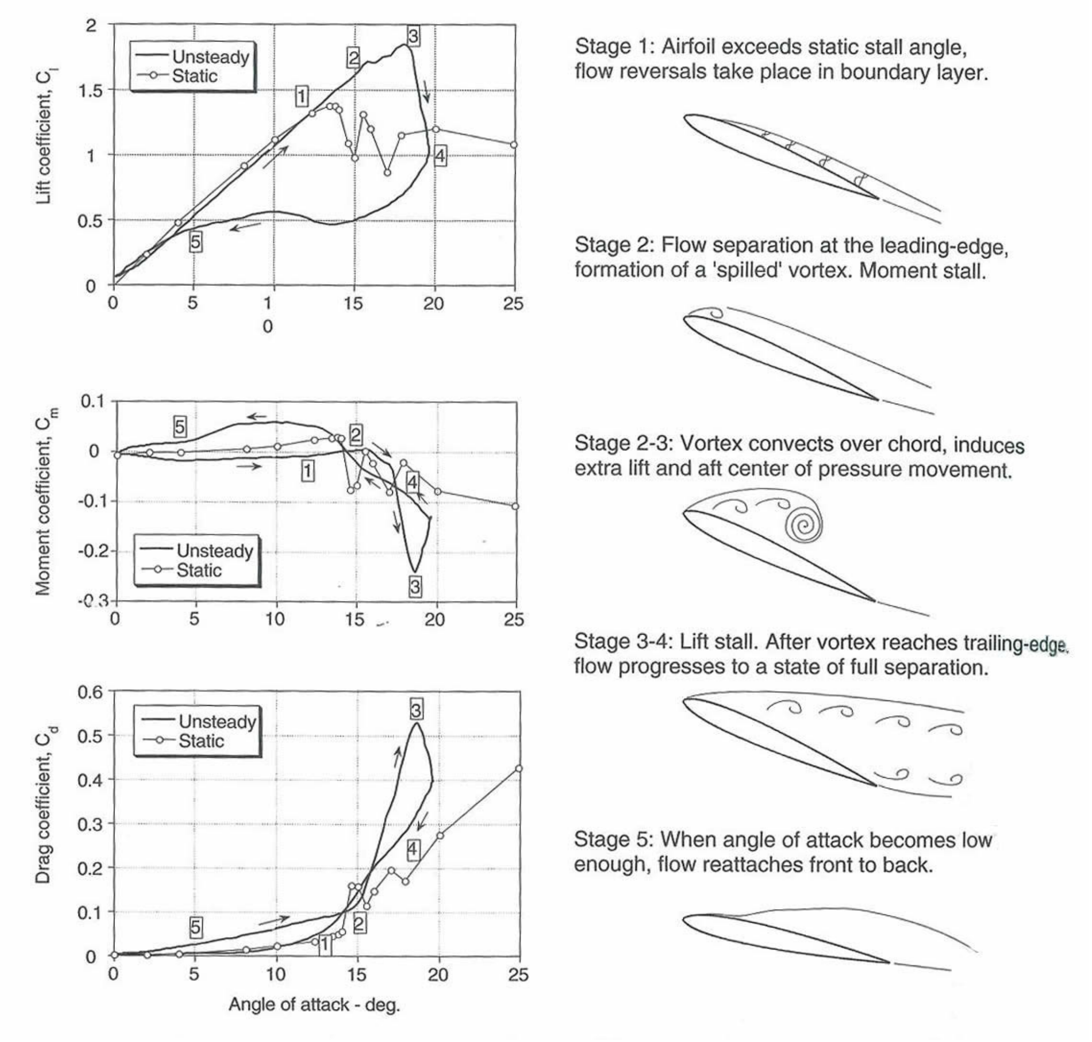

Stage 1: Airfoil exceeds static stall angle, flow reversals take place in boundary layer.

Stage 2: Flow separation at the leading-edge, formation of a 'spilled' vortex. Moment stall.

Stage 2-3: Vortex convects over chord, induces extra lift and aft center of pressure movement.

Stage 3-4: Lift stall. After vortex reaches trailing-edge, flow progresses to a state of full separation.

Stage 5: When angle of attack becomes low enough, flow reattaches front to back.

Figure 1.1 A pictorial representation of the dynamic stall process (adapted from Leishman, 2004)

CHAPTER 2 EXPERIMENTAL SETUP

This study proposes to investigate low Reynolds number dynamic stall by measuring the unsteady forces acting on an airfoil varying from pre-stall to stall conditions. In Chapter 1, the need for direct force measurements in the study of aerodynamic response of a pitching airfoil undergoing dynamic stall and the associated linear/nonlinear, stationary/nonstationary behavior is stated. Two different experiments are planned to obtain understanding under dynamic stall conditions. These experiments are the direct force measuring investigation and a flow visualization study to obtain qualitative flow information to corroborate the quantitative force measurements. The force measuring experiment is carried out in a wind tunnel while the flow visualization study is conducted in a water tunnel facility. The description of these two tunnel facilities is given separately. The design criteria of the 2-D airfoil model with direct force measurement capability are explained in terms of its ability to measure the force correctly and its ability to pitch without interfering with the proper measurements of the unsteady forces. Details of the airfoil model thus designed and fabricated, and the associated diagnostic instrumentation used to deduce the forces are described below. Finally, the water tunnel facility and the instruments used for the flow visualization experiments are specified and briefly described.

2.1 Wind Tunnel Facility and Flow around the Airfoil

All force measurements are carried out in the wind tunnel laboratory of the Department of Mechanical Engineering at the Hong Kong Polytechnic University

(Figure 2.1). The closed-circuit subsonic wind tunnel has a square test section of 600 mm x 600 mm. The length of the test section is 2.4 m and the contraction ratio of the wind tunnel is 9:1. The test section is made of removable panels for easy installation of the test model. The wind tunnel is powered by an axial flow fan which is driven by an AC 380 V, 60 Hz, 3-phase 60 hp motor. The speed of the motor is controlled by a Dynagen model S36-4060-686 inverter with a resolution of 0.3 rpm/0.01 Hz. The wind tunnel can produce a maximum flow speed of 40m/s in the test section. In the present study, all wind tunnel experiments are conducted at a free stream velocity, U_∞, of 18.8 m/s. The turbulence intensity measured along the axis passing through the test section centre at a distance 0.8 m downstream of the test section entrance at $U_\infty = 18.8$ m/s is 0.03%.

In order to determine the span of the airfoil where the flow is essentially 2-D, the streamwise flow velocity, U, of the wake at various spanwise locations is measured and compared to the streamwise flow velocity measured at mid-span, U_{ms}. Constant temperature hotwire anemometer is used to carry out the velocity measurements because of its good spatial resolution, high flow sensitivity and high frequency response. A Dantec Model 55P51 gold-plated X wire probe with straight prongs is used. The probe has two 5 μm-diameter and 3 mm-long platinum-plated tungsten wire sensors. This X-wire probe has a sensor plane parallel to the probe axis. The sensors can measure velocities from 0.2 m/s to 200 m/s and the frequency response is 90 kHz at 100 m/s. The working temperature of the sensor is determined by the overheat adjustment, which is calculated from the active sensor resistance, the probe resistance, and the overheat ratio.

The output of the hotwire anemometer is an analog voltage. Therefore, calibration of the hotwire output voltage against flow speed has to be carried out. The X-wire probe is placed in the middle of the test section at the location where the airfoil is mounted and varying the flow speed of the wind tunnel. The output voltage of the hotwire is recorded together with the flow speed. The voltage data collected from the two wires (M1 and M2) of the X-wire probe are first corrected with temperature using the following formula

$$E_{corr} = \left(\frac{T_w - T_0}{T_w - T_a} \right)^{0.5} E_a \ , \tag{2.1}$$

where E_{corr} = temperature corrected voltage, E_a = measured voltage, T_w = sensor temperature, T_0 = ambient reference temperature related to the last overheat ratio set-up before calibration, and, T_a = ambient temperature during measurement. In Figure 2.2, the corrected voltage data (*t1* and *t2*) are plotted against the flow velocity and the polynomial relation between the voltage data and flow speed is determined from this measured data.

Before the streamwise flow velocities (U) of the wake are measured at various locations along the span, the width of the airfoil wake must be determined. The location of the probe along the transverse direction relative to the trailing edge the measurement position must lie outside the wake. In other words, the probe has to be in a region where the flow velocity is essentially the same as U_∞. A computer-controlled traversing system powered by a step motor is used to move the hotwire probe up and down the y direction to traverse the wake flow and later for the flow velocity measurement. The xyz coordinate system is attached to the airfoil trailing edge at mid-span at $\alpha = 0^\circ$, where x is the stream direction, y is the transverse direction and z is the span direction as shown in the schematic of the wake flow measurement setup in Figure 2.3. The probe axis is set parallel to the direction of the main flow. The hotwire probe is traversed in the y direction at one-quarter chord behind the trailing edge at mid-span. The position of the chord of the airfoil fixed at $\alpha = 0^\circ$ is taken as the datum. In order to determine the wake width at different angles of attack, measurements were taken from a minimum of 40 mm below the datum (negative y direction) to a maximum of 40 mm above the datum (positive y direction) at $\alpha = 0^\circ$, 3°, 6°, 8°, 9°, and 12° with a sampling rate of 400 Hz. Via with a BNC-2110 BNC board, the output signal is collected using a 16-channel, 12-bit National Instrument A/D board (Model PCI-MIO-16E-1) installed on a Pentium II IBM-compatible computer in conjunction with the data acquisition software LabView. The record length is 10 seconds at all α tested. The mean value of each set of the collected voltage data is separately converted into velocity using the calibration curves shown in Figure 2.2. The converted data are then decomposed into velocity components along two orthogonal directions, U_1 and U_2, in the wire coordinates, and are subsequently converted to U and V along the x and y directions, respectively. The mean flow velocities U and V measured at all α tested are presented in Figure 2.4. A velocity defect in the x direction is observed at all α shown. The edge of the wake flow is clearly indicated and it can be seen that the wake width increases with increasing α.

Based on these results, the velocity measurements along the span of the airfoil are carried out with the hotwire probe placed at a vertical position h, such that it is outside of the wake flow at corresponding α. At $\alpha = 0^\circ$, measurements are taken at 21 points along the span at $c/4$ downstream of the trailing edge from $z = -200$mm (where a right hand screw convention is used for the xyz coordinates) to $z = 200$mm at 10mm increments. The origin of the coordinate system is taken to be located at mid-span of the trailing edge as shown in Figure 2.5. The measurement is repeated for $\alpha = 3^\circ, 6^\circ, 8^\circ, 9^\circ$, and 12°. From Figure 2.6 to Figure 2.10, two graphs are shown for each α. The upper graphs show the mean flow velocities U and V deduced from the voltage measurements of the two wires versus the spanwise distance from mid-span. The lower graphs show U normalized by its value measured at mid-span, i.e. $U_n = U/U_{ms}$ versus the spanwise distance from mid-span. According to the results in Figure 2.6 to Figure 2.11, $V \approx 0$ and the spanwise variation of U_n is less than 5% at $\alpha < \alpha_{ss}$ and is less than 12% at $\alpha > \alpha_{ss}$. The greatest variations are observed near the ends of the airfoil. The variation along the central 400mm span is found to be very small, less than 2% for all α tested. Hence, the span along which the flow is 2-D is determined to be $s = 400$ mm.

2.2 Design Criteria of a 2-D Airfoil Model with Direct Force Measurement Capability

Before designing a 2-D airfoil model with direct force measurement capability for dynamic stall studies, the criteria for the design have to be carefully considered. First, the airfoil model has to have a built-in pitching mechanism. Second, the load cell should move with the airfoil so that they can measure the instantaneous force directly in the direction normal to and along the chord of the airfoil. This ensures the measured unsteady forces could easily be resolved into lift and drag. Third, the airfoil has to be relatively stiff so that the natural frequency is far removed from the dominant frequency of the dynamic stall. Fourth, the mounting of the airfoil at both ends should be identical so that 2-D flow around the airfoil could be maintained. Besides, the instrumentation must be able to measure the instantaneous force directly in both the stream and transverse direction, and the dynamic range of the sensors and readout instruments must be reasonably high to capture the high frequency components of the aerodynamic force signals.

In addition to the above criteria, the boundary condition requirements of the model also have to be considered. Most experimental studies in the past the oscillating airfoil is mounted such that one end of the airfoil model is held by the pitching mechanism directly. The other end of the airfoil is held by a bearing or the airfoil is simply mounted as a cantilever. Either way, this type of mounting yields a mixed boundary condition for the test model; a clamped-end and a simply-supported (or free-end) boundary condition. Pitching an airfoil with only one end mounted therefore relies on the structural stiffness of the model to transfer the pitching moment to the other end. Under this mixed boundary condition, the 2-D flow around the airfoil would be approximately true only if the airfoil model is rigid. A rigid structure is one with infinite stiffness. However, in reality, all structures have finite stiffness. Lau *et al.* (2004) carry out wind tunnel experiments to study the wake-induced vibration of a NACA 0012 airfoil placed in tandem with an upstream circular cylinder. The authors show that the rigidity assumption is an approximation and torsional deformation of the model could result. Therefore, the 2-D flow assumption could be compromised and the force data obtained will be contaminated by 3-D flow effects.

In view of this, the 2-D airfoil model should be designed to have a driving mechanism to oscillate the airfoil at both ends where force cells are also installed to measure the spanwise-averaged forces. The driving mechanisms should be located outside the wind tunnel and not attached to its side walls in order to avoid signal contamination by tunnel wall vibrations. In this way, the weight of the two driving mechanisms is carried by a separate frame and the airfoil can undergo oscillation with minimum torsion. Furthermore, the load cells will move with the pitching airfoil and always measure the force components normal to and along the chord of the airfoil. If the airfoil model is designed properly, the load cell at each end of the airfoil will measure the same spanwise-averaged lift and drag forces and together they will give the total lift and drag forces acting on the airfoil (Savkar *et al*., 1980, and So *et al*., 1981).

2.3 Direct Force Measurement

2.3.1 The 2-D Airfoil Model and its Natural Frequency

A schematic of the direct force measurement setup is shown in Figure 2.12. The carbon fiber airfoil model used in the wind tunnel experiment is a NACA 0012 airfoil with a chord, c = 0.06 m and a span, s = 0.4 m (measured from end plate to end plate). Impulse tests are conducted to determine the natural frequencies of the airfoil from the vibration amplitude measured by a laser vibrometer. A schematic of the impulse test and measurement is shown in Figure 2.13. The power spectrum calculated from the measured displacements signal is shown in Figure 2.14. A very prominent peak is observed and the frequency at which the peak occurs is taken to be the first mode natural frequency, f_n, which is 74.6 Hz. The highest pitching frequency of the unsteady force experiment is set to be 4 Hz ,which will be explained in the next chapter, thus the measured frequency of the airfoil of 74.6 Hz is well beyond the expected dominant frequency of dynamic stall.

2.3.2 The Pitching Mechanism

Two Panasonic Model MSMA502A1H 5-kW low-inertia AC servo motors each driven by an MSDA503A1A driver are used to oscillate the airfoil by its two ends. Each motor is equipped with an internal incremental type encoder of 2500 P/r and has a revolution rating of 3000 r/min. The internal settings of the motors can be made manually on the driver or using a software PANATERM. A 380 V three-phase power supply is stepped down using a transformer to 200 V as required by the drivers. A NAIS programmable logic controller (PLC) FP Sigma Model FPG-C32T is used to control the motors. Programming tool software FPWIN GR Version 2 is used to program the PLC and the PLC is connected to the computer via a PC connection cable. The PLC has a high speed counter and pulse output functions which support pulse frequencies up to 100 kHz. Position control of the servo motors are done by sending pulses to the two motor drivers. When the two output channels of the PLC are connected to the two servo motors via the drivers, the response time of the two output channels to the PLC pulse input is 2 μs or less from off to on and is 8 μs or less from on to off at an input current of 15 mA or more, and the maximum output frequency of the PLC is 60 kHz. The two motors are programmed to apply a pitching motion simultaneously to the airfoil by its two ends.

2.3.3 The Piezoelectric Load Cells

Two Kistler Type 9251A three-component force piezoelectric load cells (shown in Figure 2.15) are used to measure the unsteady force acting on the airfoil. For ease of reference, the three directions are designated as X, Y and Z where X and Y lie in the plane of the load cell sensor and Z normal to the XY plane. The load cell measures the tensile force when the applied force is in the direction of the load cell axis (Z direction), and the shear force when the force is perpendicular to load cell axis (X and Y direction). Since friction is the only mechanism used to transmit shear forces to the load cells, a preload must be applied. A preload-to-maximum measured load ratio of 10 is recommended by the manufacturer to ensure linearity of charge output to the force measured and hence the accuracy of the measurements. For the present experiments, a preload of 13 kN compression force is measured and applied to the load cells through the installation of a Kistler Type 9461 preloading set and two stainless steel circular preload plates as shown in Figure 2.16. Since the maximum force measured is less than 15 N, the magnitude of the preload is more than sufficient for the present purpose. Figure 2.17 shows the setup of the preloading process.

2.3.4 Mounting of the 2-D Airfoil Model

In order to meet the design criteria, two separate frames, neither linked nor connected to the walls of the wind tunnel, are fabricated to hold the two motors, one to the right of and another to the left of the test section, to prevent contamination of the force signals by tunnel walls vibrations. Aluminum end-plates of 120 mm diameter (Figure 2.18) are installed at the two ends of the airfoil to minimize the flow effect created through the interaction between the wind tunnel wall boundary layer flow and the main flow along the airfoil span by essentially thinning the wall boundary layer developed around the airfoil.

The NACA 0012 airfoil model with end plates is held horizontally at mid-height and 0.46 m from the entrance of the test section through a hole on the tunnel walls. Two end walls each has a circular opening at mid height extended from the ceiling to the floor of the test section. They are aligned with the end plates of the airfoil model such that the end plates serve as part of the end walls. Two plastic sleeves circumscribe the openings of the end walls with a 1-mm gap left between the sleeves and the endplates (Figure 2.19) to shield the load cells from the oncoming flow and to prevent leakage of the flow to outside of the wind tunnel through the opening on the test section walls.

In the present setup, one of the preload plates of each piezo-electric load cell is housed inside the end plate at each end of the airfoil while the other preload plate of the load cells is housed inside a connecting socket, one at each end of the airfoil model as shown in Figure 2.20. The two connecting sockets are then installed onto the motor shafts. This airfoil assembly gives a clamp-clamp boundary condition. When the airfoil is pitched, the load cells installed at the two ends rotate with the airfoil. Thus designed, the X- and Y-axes of each load cell can measure the force normal to and along the chord of the airfoil respectively.

2.3.5 Amplification and Acquisition of the Force Signals

The load cells output electrical charges that are linearly proportional to the shear force measured in the X and Y direction. Four Kistler Type 5011B charge amplifiers (as shown in Figure 2.21) are used to convert the electrical charges from the load cells into a proportional voltage signal. Each charge amplifier has an upper frequency limit of 200 kHz and is equipped with an adjustable 8-stage low-pass filter which allows reduction of the upper frequency limit. Via a BNC-2110 BNC board, the voltage signals output by the charge amplifiers are then transmitted to a data acquisition system which is composed of a 16I/2O Nation Instrument DAQ card 6062E of 500 ks/s and 12-bit multifunction I/O installed on a Pentium III Notebook PC. The system is controlled by MATLAB using its data acquisition toolbox.

2.3.6 Calibration of the Load Cells

Due to the physical constraints of the wind tunnel section, static weight calibration of the load cells could not be done *in situ* without contaminating the load cell signals, therefore the static weight calibration is performed outside of the test section. The airfoil model with one load cell at each end is held stationary while static weights are added to one axis at a time and each axis of the load cells is calibrated separately. In order to avoid confusion, the load cell with serial number 624003 is designated as “L6” and the one with serial number 956056 is designated as “L9”. The outputs of each load cell are also named according to the load cell’s designation and the direction of the axis measured, i.e. “L6X”, “L6Y”, “L9X”, and “L9Y”. The output voltage of the charge amplifier is calibrated statically with calibration weights and the calibration results are found to be repeatable. It can be seen from Figure 2.22 that the output voltages vary linearly with increasing weights. The conversion of voltage to force for each axis is carried out using separate calibration curves.

2.4 Water Tunnel Facility and Flow Visualization

To corroborate the force measurements, flow visualization experiments are carried out to capture the images of the flow around the oscillating airfoil. By observing the flow detachment and reattachment to the airfoil from the flow visualization images, both α_{ss} and α at which the flow reattaches can be determined for static and pitching airfoil and can be compared with the results obtained from the wind tunnel force measurements at the same Re. The test conditions will be described in detail in the next chapter.

The flow visualization experiments are carried out in the Water Tunnel Laboratory located in the Mechanical Engineering Department of the Hong Kong Polytechnic University. The open-channel water tunnel has a test section of 0.3 m (W) x 0.6 m (H) x 2.0 m (L) as shown in Figure 2.23. The flow speed can be adjusted from 0.05 m/s to 4 m/s. As in the case of the wind tunnel, the entrance velocity is found to be unidirectional and uniform for the Re tested. The tunnel is powered by a 60 hp, 380 V AC, 3-phase, 6-pole motor. The test section of the water tunnel is composed of removable panels for installation of test model. In the present study, all the flow visualization experiments are carried out at U_∞ = 1.32 m/s.

An airfoil model of the same geometric shape (NACA 0012) and the same chord (c = 0.06 m) as the one used in the wind tunnel is fabricated for the flow visualization experiment. The airfoil has a span of 28 mm and is held at 1.45 m downstream of the test section entrance of the water tunnel. The airfoil spans the test section horizontally at mid-height with a 1-mm gap from the tunnel walls. Since the visualization images of the flow are acquired at mid-span, the gap effect is negligible for this span of the airfoil. With a 6-mm diameter steel shaft intruding the airfoil at its aerodynamic center at *c*/4, one end of the airfoil is clamped to the motor and the other end is rested on a slot on the tunnel wall of the test section. The 8mm-diameter slot allows the shaft to rotate without friction. Thus, the motion of the airfoil is constrained to pitching only. The same pitching system as the one used in the force measurement experiment is used to oscillate the airfoil in the water tunnel. However, a single motor installed at one end only is used to pitch the airfoil because the other end of the airfoil must be free of obstacle to allow image acquisition of the flow (Figure 2.24).

The hollow airfoil is modified to allow a set of rubber tubing to connect to pin holes installed at the leading edge of the airfoil at mid-span. Color dye is injected into the flow through this set of tubing. Illumination of the flow is generated by two New Wave standard pulse laser sources focus at the mid-span section of the airfoil. Each laser source has a wavelength of 532 nm and a maximum energy output of 120 mJ. Digital images are acquired using a HiSense type 13 CCD camera with a gain of 4, double frames, and a resolution of 1280×1024 pixels. Image acquisition and illumination of the flow by the lasers are synchronized through the use of the software Dantec FlowMap Processor PIV2100 and the trigger pulse of a voltage signal. The analog position reference signal from the PLC is modified to give the trigger pulse of 5 V when the airfoil reaches the maximum α of the pitching motion. Controlled by the software, the trigger pulse initiates the shutter of the camera and images are captured at set time interval.

Figure 2.1 Wind tunnel (adapted from Long Wind Science & Technology Co., Ltd)

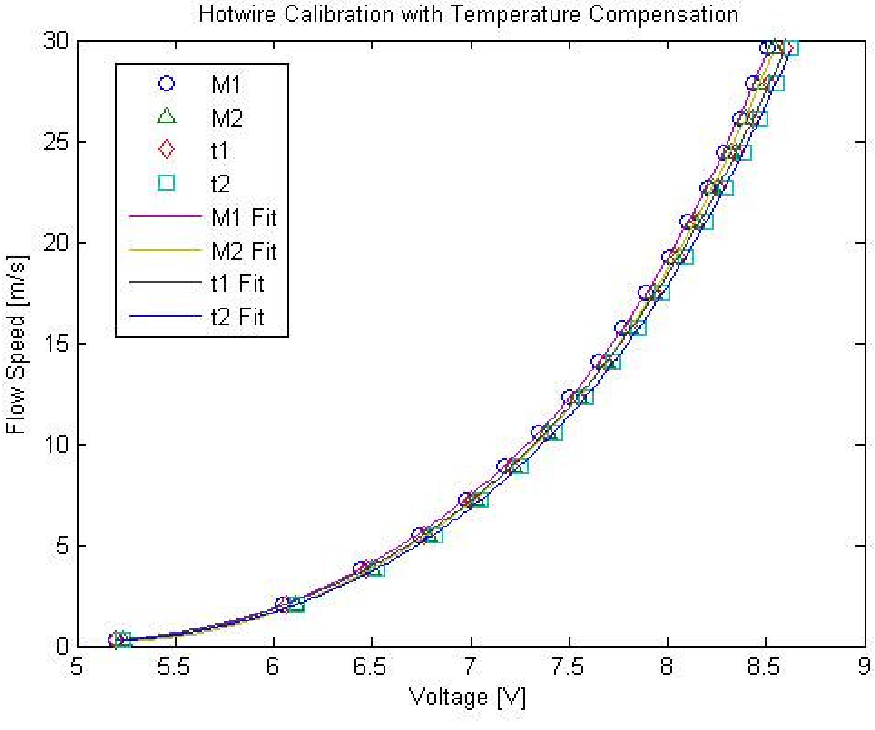

Figure 2.2 Hotwire calibration with temperature compensation

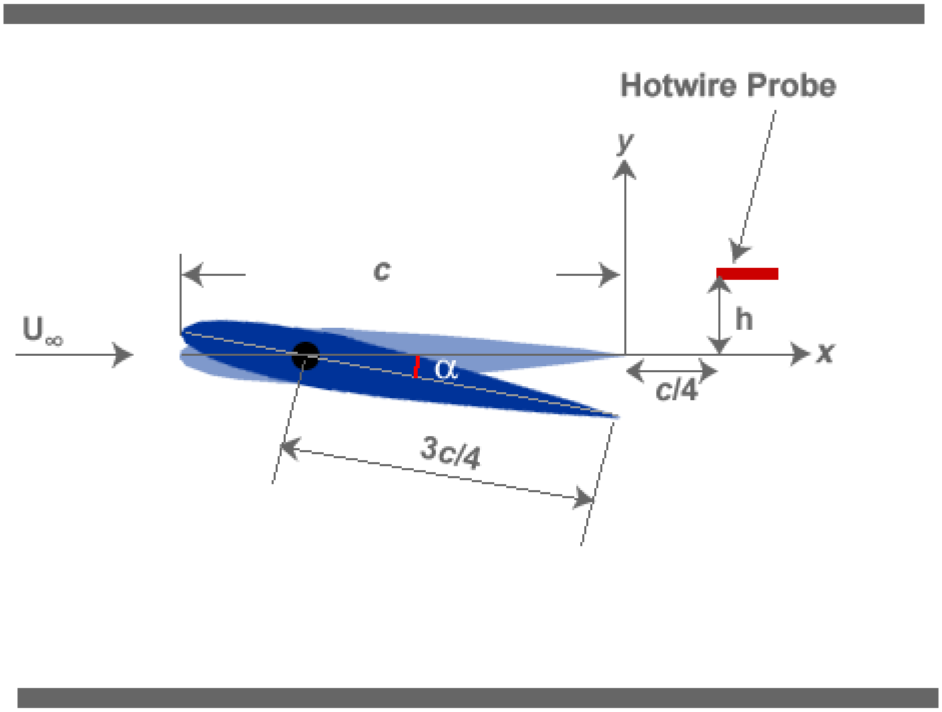

Figure 2.3 A schematic of wake flow measurement.

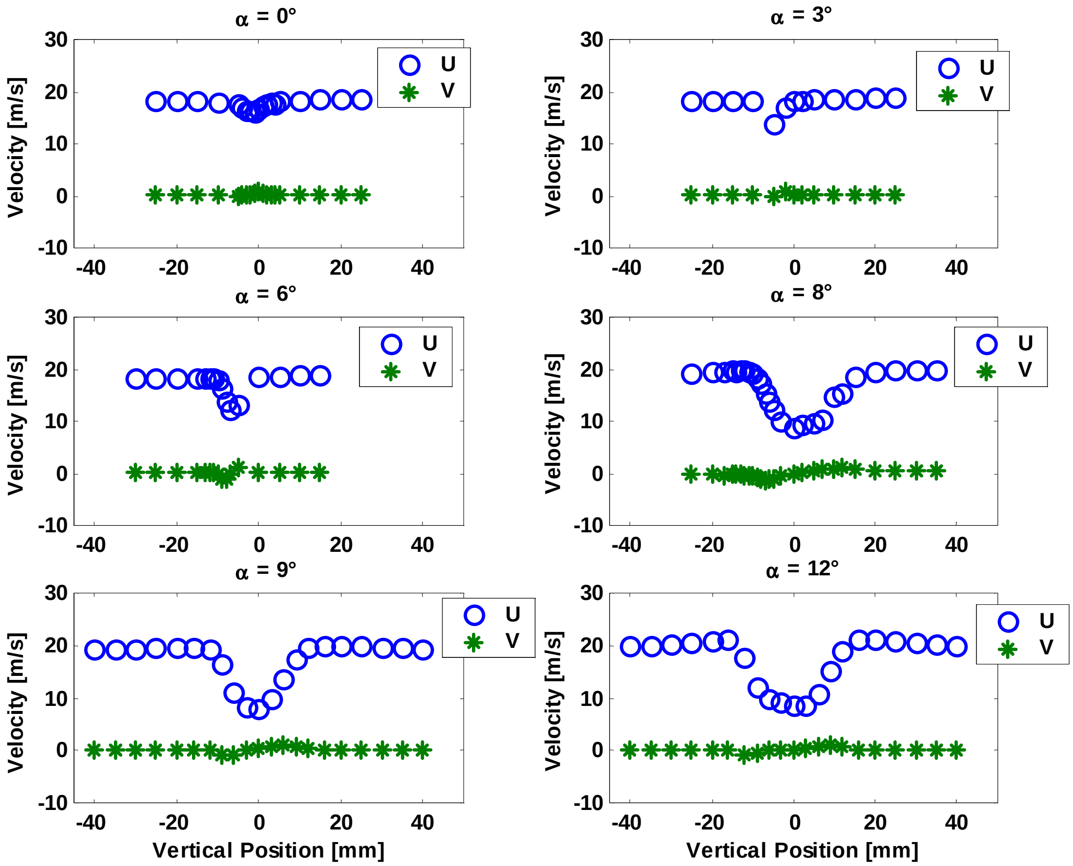

Figure 2.4 Measurement of wake width behind the airfoil.

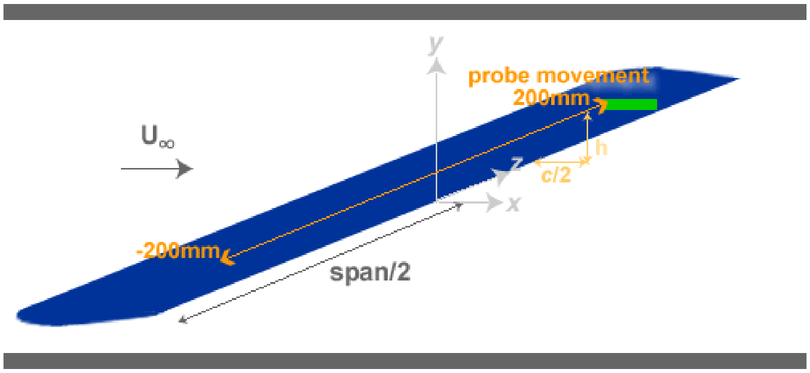

Figure 2.5 A schematic of velocity measurement along the span.

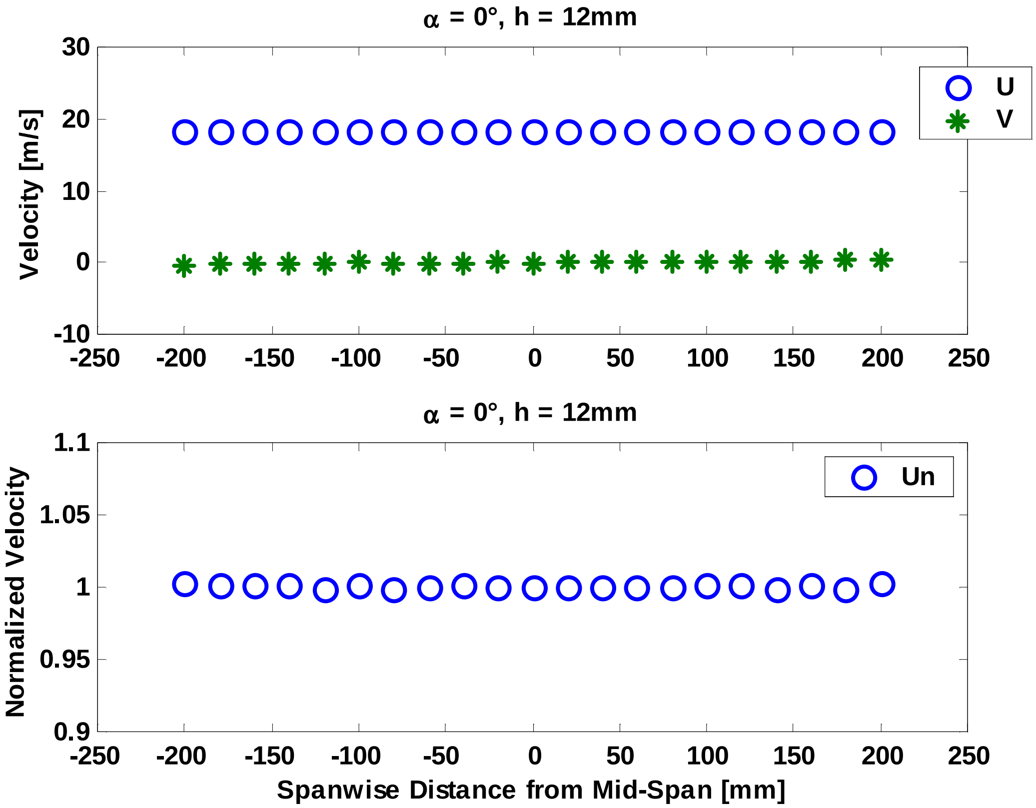

Figure 2.6 Spanwise flow velocity correlation, at $\alpha = 0^{\circ}$.

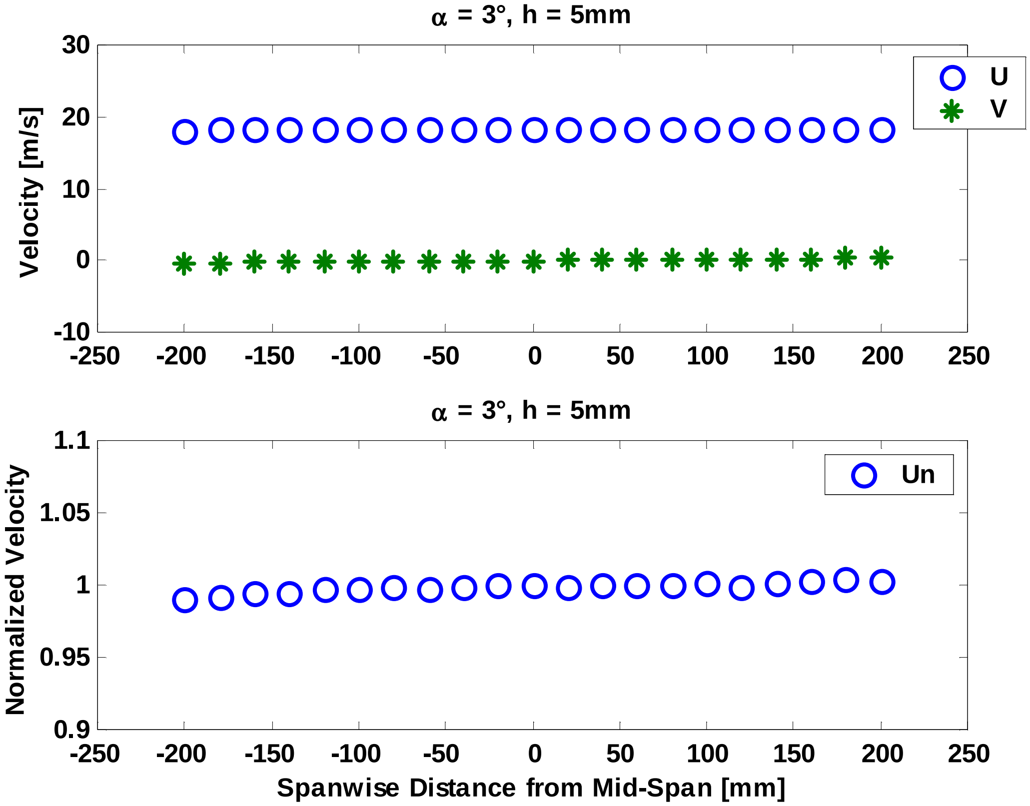

Figure 2.7 Spanwise flow velocity correlation, at $\alpha = 3^{\circ}$.

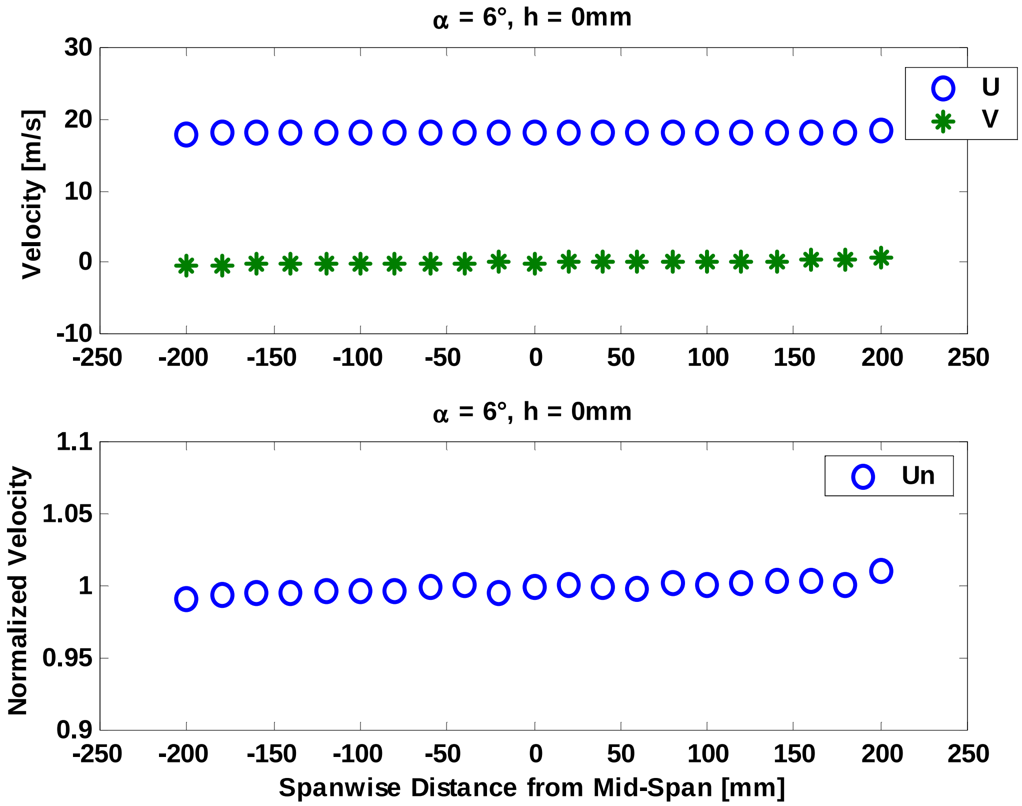

Figure 2.8 Spanwise flow velocity correlation, at *α* = 6˚.

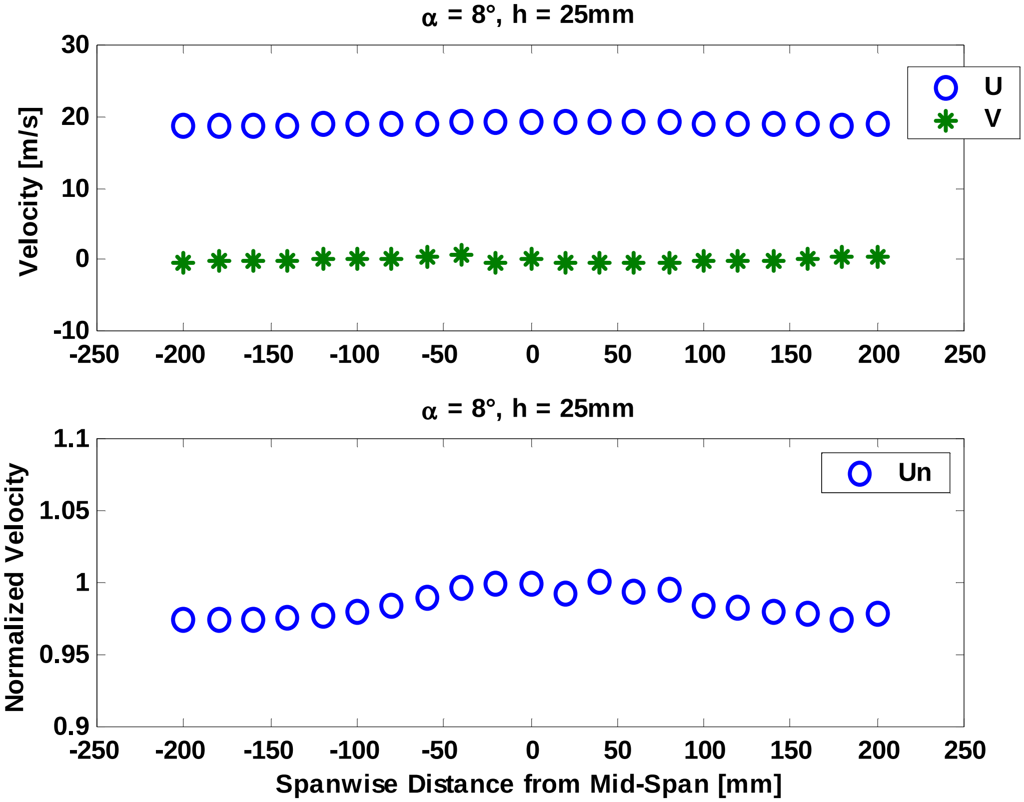

Figure 2.9 Spanwise flow velocity correlation, at $\alpha = 8^{\circ}$.

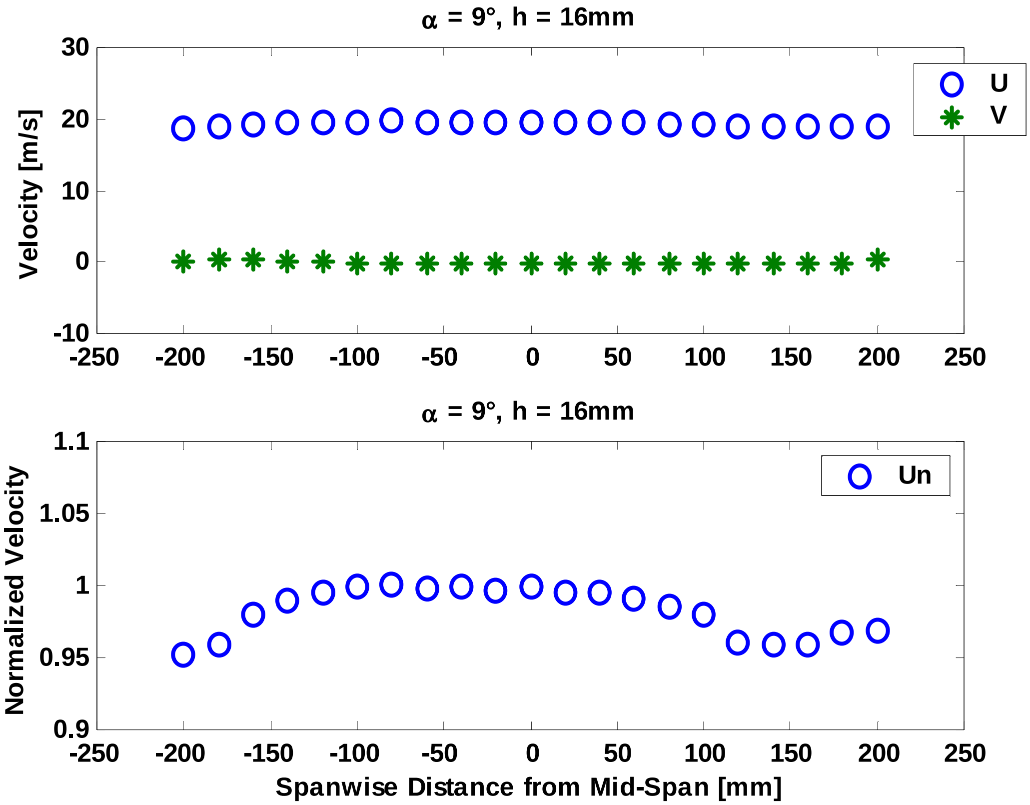

Figure 2.10 Spanwise flow velocity correlation, at $\alpha = 9^\circ$.

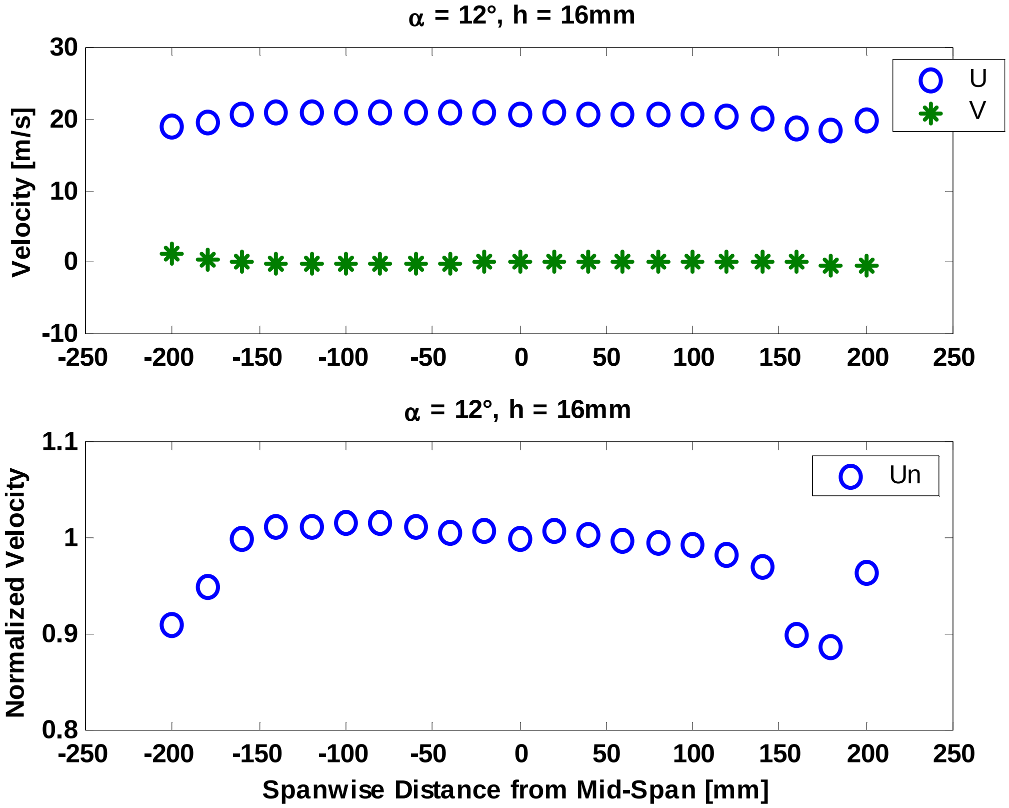

Figure 2.11 Spanwise flow velocity correlation, at *α* = 12˚.

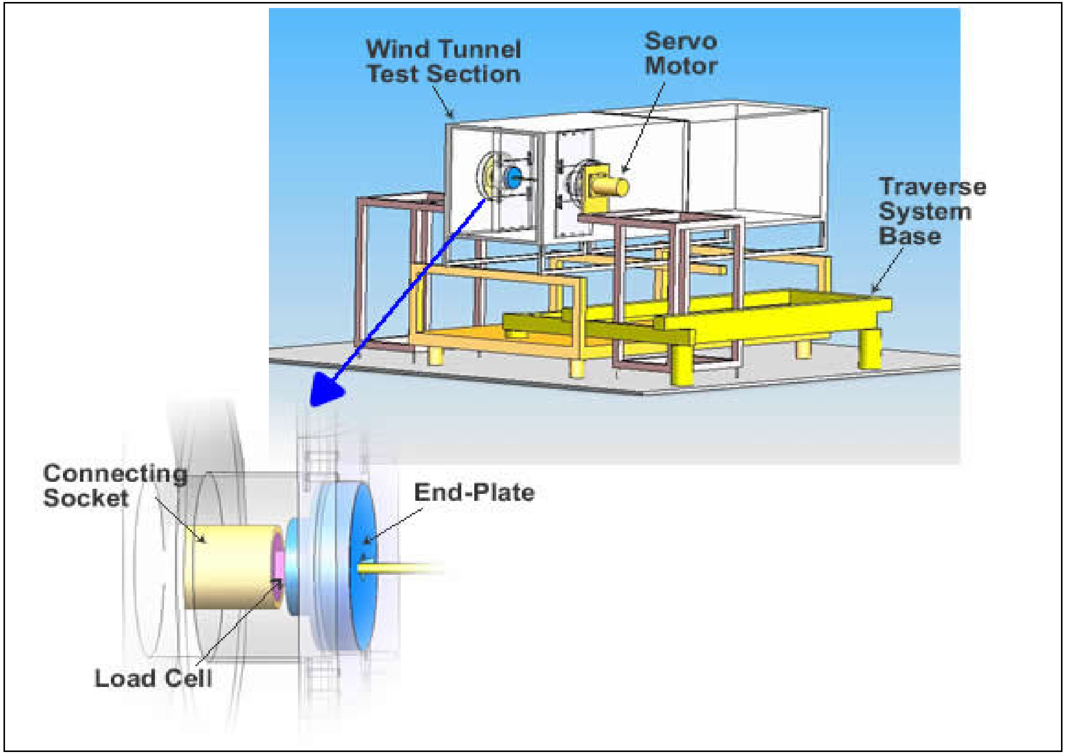

Figure 2.12 Schematic of direct force measurement setup

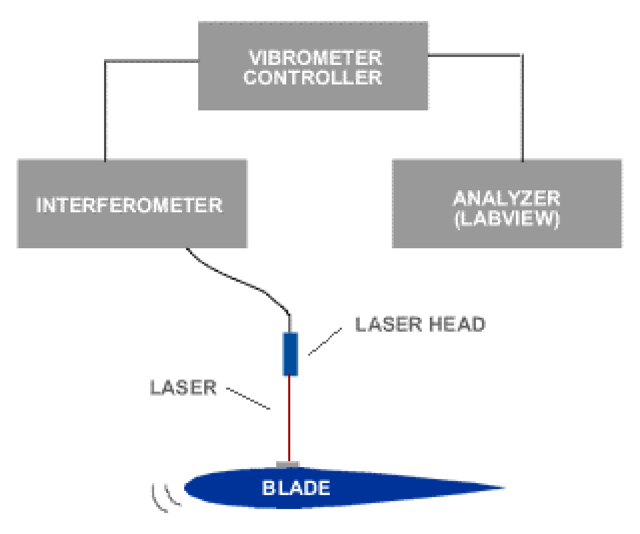

Figure 2.13 Schematic of airfoil natural frequency measurement.

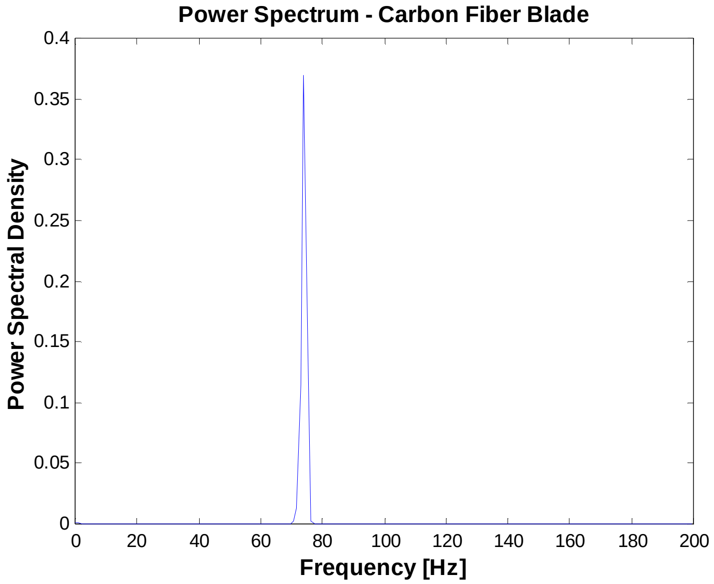

Figure 2.14 Spectrum analysis of carbon fiber airfoil.

Figure 2.15 Piezo-electric load cells.

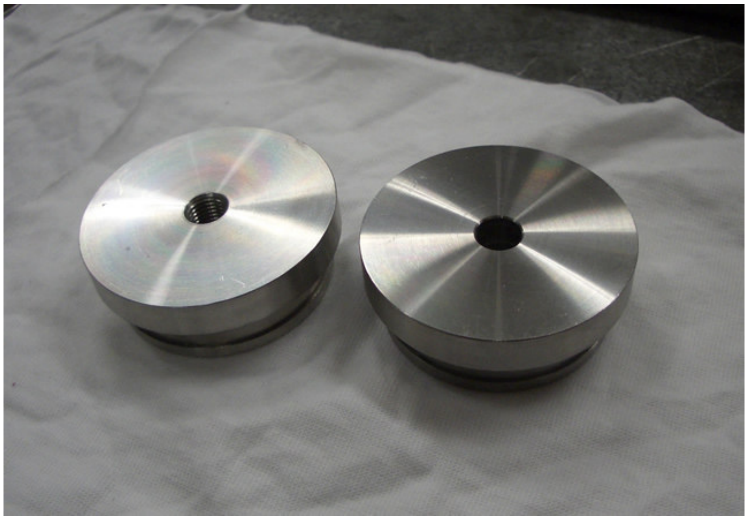

Figure 2.16 Stainless steel plates for preloading.

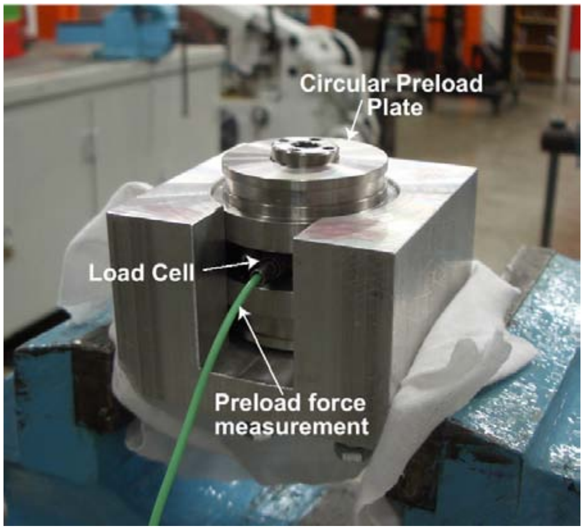

Figure 2.17 Preloading of a piezo-electric load cell in progress.

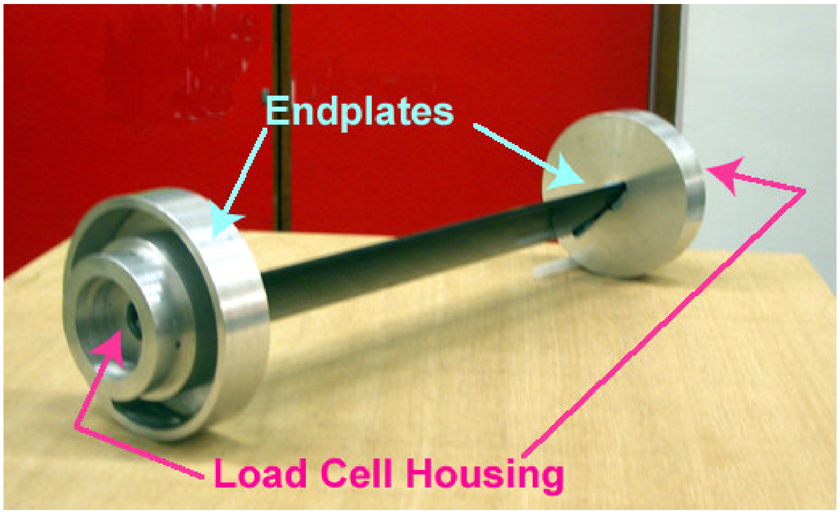

Figure 2.18 Airfoil with endplates

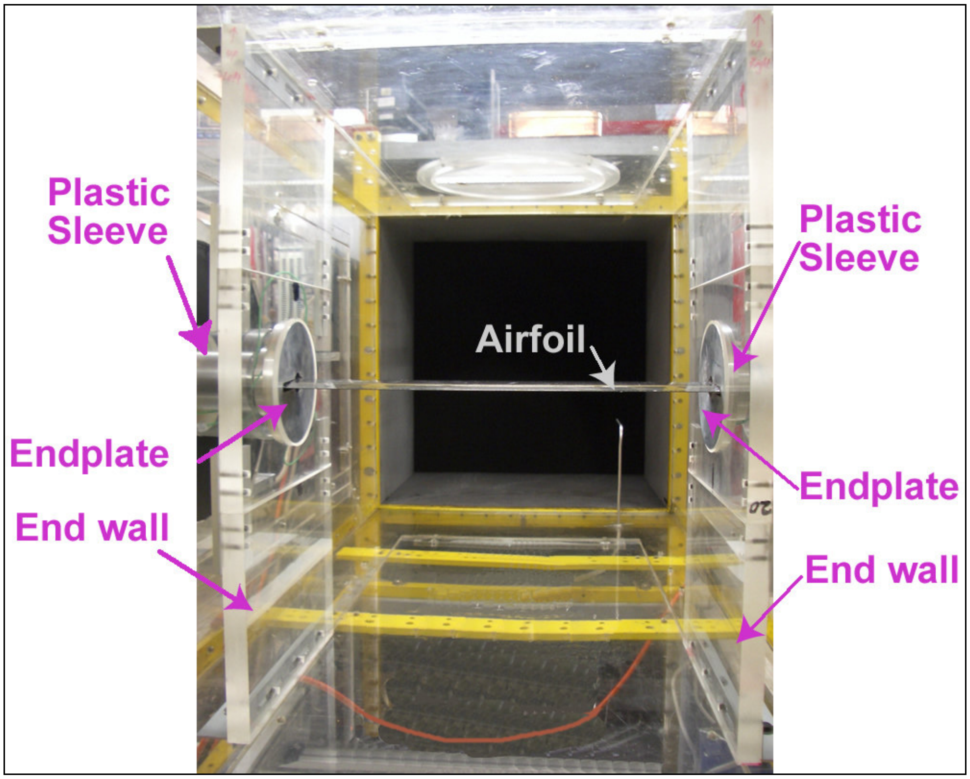

Figure 2.19 Airfoil model in the test section

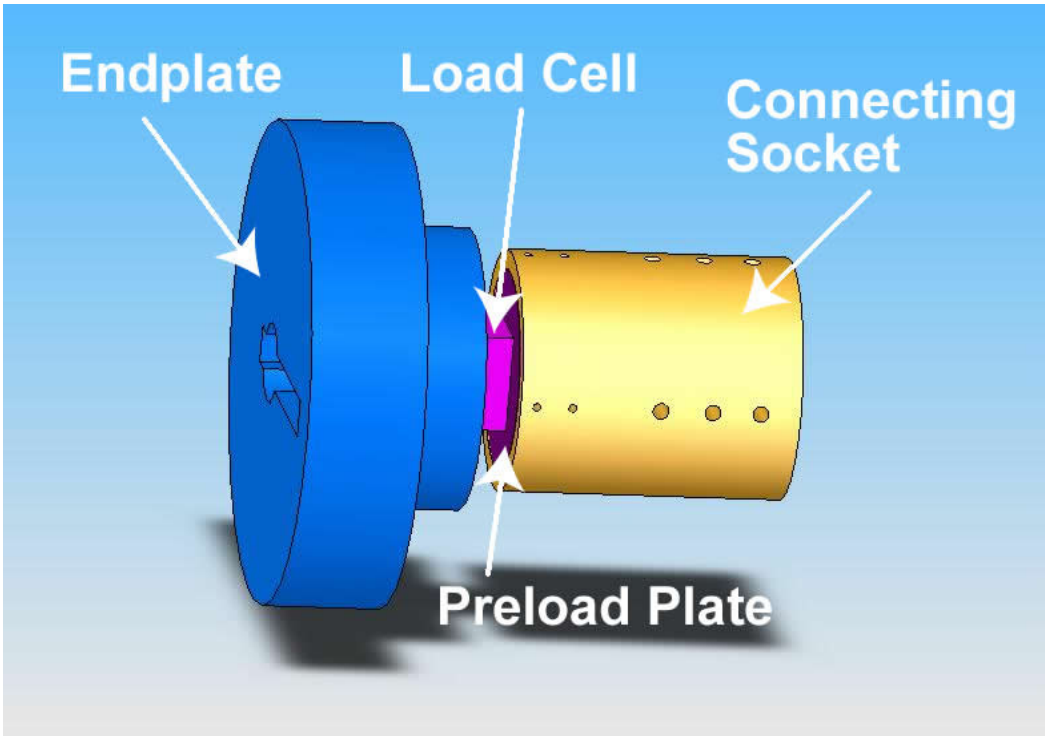

Figure 2.20 A schematic of load cell housings

Figure 2.21 The charge amplifiers of the piezo-electric load cells.

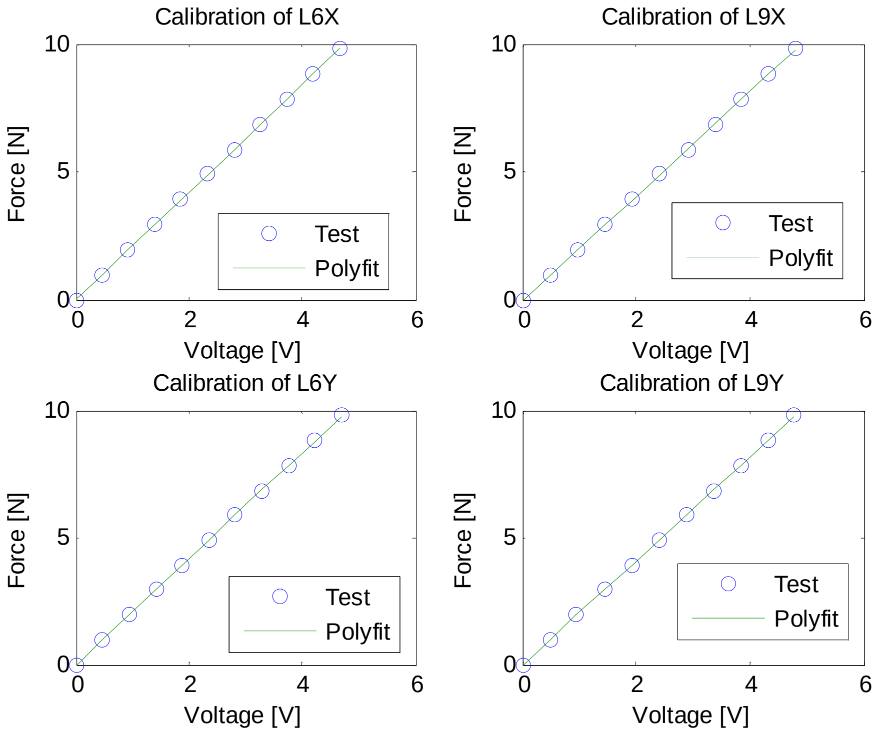

Figure 2.22 Calibration of load cell axes.

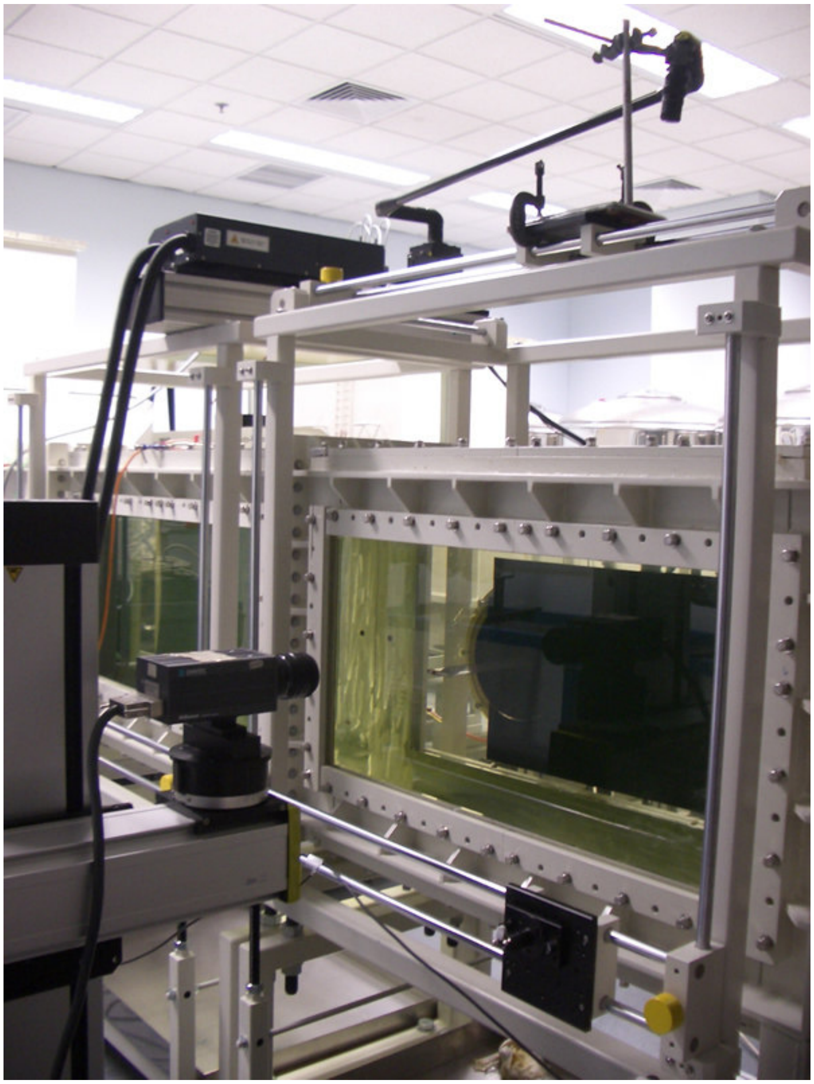

Figure 2.23 Test section of the water tunnel.

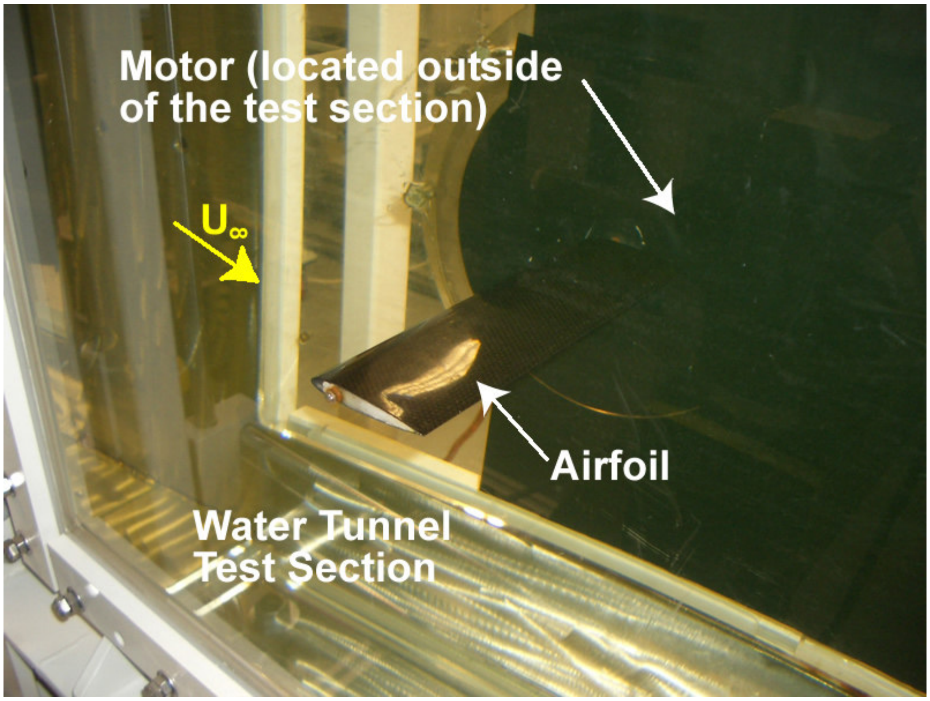

Figure 2.24 Airfoil in water tunnel test section.

CHAPTER 3 DATA ANALYSIS

The test conditions of steady and unsteady force measurements of a pitching airfoil undergoing dynamic stall and the test conditions and procedures of the flow visualization experiments are discussed in this chapter. Using the experimental setups for the force measurement and flow visualization techniques described in Chapter 2, both the steady and unsteady force data are obtained. Therefore, in this chapter, the data reduction and analysis methods used to study the aerodynamic response of the force measurements and the associated linear/nonlinear, stationary/nonstationary behavior of the pitching airfoil undergoing dynamic stall are also discussed. Two different data analysis techniques are described; one for the analysis of stationary signals, another for the analysis of nonstationary signals. In addition, the analysis technique of flow visualization results to corroborate the force measurements is described. This way, the true character of the unsteady force signals could be deciphered and, in the process, the physics of dynamic stall could be understood. It is hoped that through this study, the cause of the nonlinear behavior of dynamic stall could be identified by analyzing the measured force signals.

3.1 Wind Tunnel Test Conditions

Wind tunnel testing is carried out to obtain force measurements of a pitching airfoil undergoing dynamic stall. In order to maximize the signal to noise ratio of the load cells outputs, the highest possible flow speed under the physical constraints of the facilities is selected. The freestream velocity is set at 18.8 m/s since it corresponded to the maximum speed of the wind tunnel without significant increase of the flow's temperature over an extended period of wind tunnel operation. As mentioned in the previous chapter, the airfoil used in the present study has a chord c of 0.06 m. In the following choice of experimental conditions, the airfoil pitching angles and their associated pitching amplitudes are selected to avoid the maximum blockage of 10%. This corresponded to a maximum blockage of 10% by the airfoil at $\alpha = 30^\circ$ and defines the maximum pitching angle and its associated pitching amplitude in which the airfoil can be pitched. Therefore, this limits the deep-stall condition that this experimental setup can accomplish. All experiments are carried out at a Reynolds number based on chord length of $Re = 7.7\text{x}10^4$.

3.1.1 Steady and Unsteady Force Measurements

In all wind tunnel runs, the first experiment is to acquire steady force measurements and the second experiment is to collect unsteady force data. With the current setup, it is found that it takes only two seconds of data to determine a reliable value for the steady force. Hence, by programming the PLC to control the motors, the airfoil is pitched from $\alpha = -8^\circ$ to $\alpha = 30^\circ$ at one degree increment. At each α the airfoil is held fixed for 5 seconds and steady force measurements are taken.

After steady force measurements are obtained, unsteady force experiments are carried out. Since the static stall angle α_{ss} is found to be at 10˚, two oscillation motion cases are selected within the pre-stall region; these are Case 1: $\alpha = 0^\circ + 5^\circ \sin(\omega t)$ and

Case 2: $\alpha = 5^\circ + 5^\circ \sin(\omega t)$, where ω is the angular pitching frequency. Two other oscillation motion cases are selected around α_{ss}; these are Case 3: $\alpha = 10^\circ + 5^\circ \sin(\omega t)$ and Case 4: $\alpha = 10^\circ + 10^\circ \sin(\omega t)$. In order to complete the whole range of stall study, a fifth oscillation motion case is selected around $\alpha_{mean} > \alpha_{ss}$; this is Case 5: $\alpha = 15^\circ + 10^\circ \sin(\omega t)$. The selection of these cases covered the range of pre-stall (Case 1 and 2), light-stall (Case 3), and deep-stall (Case 4 and 5) of the airfoil. The reasons for the categorization of the cases will be made clear in Chapter 4. Four reduced frequencies, k = 0.005, 0.01, 0.02, and 0.04, are tested for each case. They are selected to essentially cover as wide a range of k as possible. The complete test matrix is shown in Table 3.1.

3.2 Data Analysis Methods

In view of the fact that the force cells are mounted in such a way that they move with the pitching motion of the airfoil, the X and Y axis of each load cell measures the force along and normal to the chord of the airfoil respectively as shown in Figure 3.1. Furthermore, the forces measured included both the aerodynamic force and the inertia force associated with the pitching motion of the airfoil. The lift and drag force components are required to be deduced from these measurements. In the following, the method and procedure used to measure and deduce the lift and drag force, including their mean and unsteady components, are discussed.

All signals measured in the wind tunnel experiments are essentially time series, be it the hot-wire signal or the force cell signals. Therefore methods such as FFT are used to analyze the measured signals to deduce their statistics as well as their associated power spectral densities in order to understand the characteristics of the signals. Since FFT and other similar methods are only valid for the analysis of time stationary signals, other methods have to be used to analyze nonstationary signals. Among the more promising methods used by previous researchers, wavelet analysis technique is found to be quite applicable for the analysis of unsteady nonstationary flow-induced forces (So *et al*. 2005). In particular, the continuous wavelet transform (CWT) can be used to analyze the power spectral density of the nonstationary signal to yield insightful results for the understanding of the physical phenomenon. This technique is used successfully by So *et al*. (2005) to study the three-dimensional (3-D) behavior of the wake flow behind a nominally 2-D cylinder in a cross flow. Their study reveals for the first time that no matter how large is the aspect ratio of the cylinder, the wake flow and vortex-induced forces on the cylinder are essentially 3-D in nature and 2-D behavior is not found anywhere along the cylinder span. In view of this, the CWT would be quite suitable for the present analysis of dynamic stall force signals. Both FFT and CWT will be used to analyze the measured force signals.

3.2.1 Time Series of Lift and Drag

Before discussing the unsteady lift measurements, two issues need to be addressed. The first is the determination of the true aerodynamic responses from the measured signals. This is necessary because the load cells measure the total load acting on the airfoil which includes the inertial response due to the pitching of the airfoil and the actual aerodynamic loading acting on the airfoil. In order to deduce the true aerodynamic responses, the inertial response due to pitching needs to be subtracted from the load cell signals. Once the measured signals are properly treated, the true aerodynamic responses can be determined. After this analysis, the true aerodynamic lift and drag acting on the airfoil is available. The method and procedure to deduce the lift and drag is discussed in this section.

During each run of the force measuring experiments, the time series of five signals are recorded. These include the voltage signals of the X and Y axes of each load cell, and an analog position reference signal of the motor shaft. As mentioned in the previous chapter, all data are sampled at a rate of 1000 Hz. Voltage signals from the load cells pass through a 300-Hz low-pass filter of the load cells' charge amplifiers and are converted to force signals separately using their respective calibration curves presented in Chapter 2. The recorded force data show that the each of two load cells measures half of the total force of the airfoil. Thus, the total normal force F_X, measured by the X axis of the load cells, and the total chord-wise force F_Y, measured by the Y axis of the load cells, are resolved to obtain the time series for the total lift force and the total drag force acting on the airfoil:

$$L = -F_X \sin\alpha + F_Y \cos\alpha\,, \tag{3.1}$$

$$D = F_X \cos\alpha + F_Y \sin\alpha\,. \tag{3.2}$$

Since the signals from the load cells are measured directly from the experiments, in view of the low-pass filtering of the force signals, the maximum frequency that can be resolved into the lift and drag components is 300 Hz. In other words, the dynamic range of the lift and drag signals is 0 to 300 Hz at best. The maximum value of this range is four times the static natural frequency of the airfoil.

The total force signals measured during the wind-on tests are composed of both aerodynamic forces and inertia forces. It is necessary to determine the inertia force arising from its oscillatory motion under wind-off conditions. Therefore, the same tests are repeated under wind-off conditions. Time series of lift signal under wind-off and wind-on conditions are obtained as such shown in Figure 3.2 and Figure 3.3. In Figure 3.2, time series of the resolved lift under wind-off and wind-on conditions of Case 2 at k = 0.04 are shown against the normalized time t_n, which $t_n = t/T$ and T is the period of one cycle of oscillation. Similarly, the time series of the resolved lift of Case 5 at k = 0.005 are shown in Figure 3.3. The aerodynamic force responses are obtained by subtracting the forces measured under wind-off condition from those measured under wind-on conditions.

It should be noted that when an airfoil undergoes oscillation in a fluid, additional pressure forces are required to accelerate the fluid in the vicinity of the airfoil (Leishman, 2000). This additional force is called the “apparent mass effect”. By using Theodorsen’s theory, the apparent mass effect of a thin airfoil undergoing pitching only motion is given by:

$$L_{apparent} = \pi \rho V^2 b \left[\frac{b}{U_\infty} \dot{\alpha} - \frac{b^2}{U_\infty} a \ddot{\alpha} \right], \tag{3.3}$$

where a is the pitch axis location relative to the mid-chord of the airfoil, which is (-1/2) in this case, b is half-chord, and ρ is the air density. In order to assess the apparent mass effect on the measurements of the present study, the lift due to apparent mass is computed for Case 5 at k = 0.04 and the result is shown in Figure 3.4. This case is chosen for its high α_{mean} and α_{amp} as the relatively high reduced frequency. Figure

3.4(a) shows both the time series of the net C_L and the net C_L corrected with lift due to apparent mass are compared. Figure 3.4(b) shows the net C_L corrected with lift due to apparent mass normalized by half of the maximum net C_L of the time series. It can be seen from the figure that the apparent mass effect is as large as 2% of half of the maximum net C_L, thus it is negligible and is not corrected for during data reduction.

The validated measurements of the true aerodynamic response of the airfoil by considering the force signals obtained under wind-on and wind-off conditions will be reported in the next chapter. Finally, time series of the spanwise-averaged lift and drag and their associated coefficients undergoing pitching motion are obtained by:

$$C_L = \frac{L_{net}}{\tfrac{1}{2}\rho U_\infty^2 sc} , \tag{3.4}$$

and

$$C_D = \frac{D_{net}}{\tfrac{1}{2}\rho U_\infty^2 sc} , \tag{3.5}$$

where L_{net} and D_{net} is the calculated true lift and drag respectively.

Phase-averaging of these deduced force data is then carried out to better characterize the aerodynamic responses as a function of α. According to the instantaneous reference position signal, ten oscillations of each set of data are extracted for the averaging process and later for power spectral analysis. The results of phase averaging are shown in the form of lift or drag variation with the instantaneous α. Therefore, the recorded data for each cycle of oscillations will show the airfoil beginning with the minimum α, pitch up to the maximum α, and then return to the minimum α.

3.2.2 Power Spectral Analysis

Power spectral analysis of the time series is carried out to investigate the frequency content of the aerodynamic responses. The present study intends to investigate the aerodynamic response of a pitching airfoil undergoing dynamic stall and the associated linear/nonlinear, stationary/nonstationary behavior. Since dynamic stall is characterized by the distinct features of lift stall, focus is placed on analyzing the time series of lift only and power spectral density (PSD) analysis of the lift signal is carried out. The airfoil is pitched about its one-quarter chord where the forces are measured; therefore, the torque about its center of mass is given by the normal force multiplied by the moment arm *r*, which is a constant as shown in Figure 3.5. Hence, the PSD results of the lift signal also represent the PSD of the energy.

If the signals are stationary, conventional methods such as FFT can be used to analyze them because normal FFT-based spectral analyses could only indicate the power of the signal at certain frequencies, while power variation of frequencies in the time domain is lost completely. This drawback would not matter if the signals are stationary, since the power of the signal does not vary with time.

On the other hand, if the signals are nonstationary, a different method, such as wavelet analysis, has to be used for the analysis if the characteristic features of the signals are meant be recovered correctly. Wavelet spectral analysis decomposes a time series into time-frequency space and is able to resolve the power variation of a set of frequencies within a time-series. In the present analysis, continuous wavelet transform (CWT) is carried out to investigate the nonstationary character of the lift time series. The CWT is defined as

$$\mathrm{CWT}(s,\tau)=\frac{1}{\sqrt{s}}\int_{-\infty}^{\infty}w(t)\psi^{*}\left(\frac{t-\tau}{s}\right)dt \quad , \tag{3.6}$$

where $w(t)$ is the data to be analyzed, $\psi(t)$ is called the mother wavelet, s is the scaling factor, and τ is the translating factor. The result of the wavelet analysis is the PSD of a series of equivalent Fourier frequency (f_{eq}) local to instantaneous time. In order to facilitate easy comparison of the PSD of various test cases, unless stated otherwise, in each case, the PSD is normalized by the maximum power of the concerned period of time ($P_n = PSD/PSD_{max}$), and the f_{eq} are normalized by the pitching frequency (f) of that particular case, ($f_n = f_{eq}/f$).

In the present analysis, the CWT with the Morlet wavelet as mother wavelet is used as suggested by Farge (1992). The Morlet wavelet is expressed as,

$$\psi(t)=\pi^{-1/4}e^{i\omega_0 t}e^{-t^2/2} \tag{3.7}$$

and the CWT of the lift time series is performed using the MATLAB algorithm developed by Torrence and Combo (1998). In this algorithm, the temporal scaling factor s is used rather than the normal frequency employed in conventional Fourier analysis. In order to interpret the results of wavelet analysis in the conventional way, the scaling factor needs to be converted into an equivalent Fourier frequency. The basic idea of conversion is to substitute a single-frequency wave of a known frequency into the wavelet transform and then find the temporal scaling factor at which the wavelet spectrum takes its maximum value. Repeating this procedure for a series of frequencies, the relation between the temporal scaling factor and the equivalent Fourier frequency can be established. For the Morlet wavelet, the relation is given by

$$f = \frac{1}{1.03s} \ . \qquad (3.8)$$

This is the equivalent Fourier frequency adopted in the present CWT analysis of the lift time series. A detail description of the CWT can be found in So *et. al* (2005).

Results of both the FFT and wavelet analysis will be shown in the next chapter. This comparison will allow the nonstationary nature and nonlinear behavior of the signal to be analyzed and studied in detail.

3.3 Flow Visualization

In order to corroborate the results from direct force measurements of the airfoil undergoing various stages of dynamic stall in the wind tunnel, flow visualization is carried out in the water tunnel. Images of the flow around the airfoil at mid-span are captured for each of the five cases investigated in the wind tunnel and at the same *k*. The flow speed of the water tunnel is 1.32 m/s to give the same Reynolds number as the force measurement in the wind tunnel, i.e., Re = $7.7\text{x}10^4$. Thus, both flow visualization and force measurement are carried out at the same Re and dynamic similarity between the two different sets of experiments could be maintained.

As mentioned in Chapter 2, when the airfoil reaches the maximum α of the pitching motion, a trigger pulse is sent to initiate the shutter of the camera and images are captured at set time interval. However, due to the occurrence of a time lag between the trigger and the initiation of the images capture, the angle of attack α cannot be determined from the motion of the airfoil and the time interval. Therefore, α must be determined geometrically from the images. The images of maximum and minimum α

could easily be recognized from each set of images in the test cases. From this α of the intermediate images can be determined using interpolation of the function of the motion and the time interval between images.

From the flow visualization images, the flow around the airfoil at mid-span at difference phases of the oscillation is observed. Hence, the angle α at which the flow starts to separate from the suction surface, to detach and to reattach are also observed. This flow visualization results could be used to compare to those obtained from force measurements, as well as to further extend the understanding of the dynamic stall behavior deduced from force measurements.

Stall Range	Case No.	α_{mean}	α_{amp}	k
Pre-stall	1	0°	5°	0.005, 0.01, 0.02, 0.04
	2	5°	5°	0.005, 0.01, 0.02, 0.04
Light Stall	3	10°	5°	0.005, 0.01, 0.02, 0.04
Deep Stall	4	10°	10°	0.005, 0.01, 0.02, 0.04
	5	15°	10°	0.005, 0.01, 0.02, 0.04

Table 3.1 Complete test matrix of unsteady force measurements

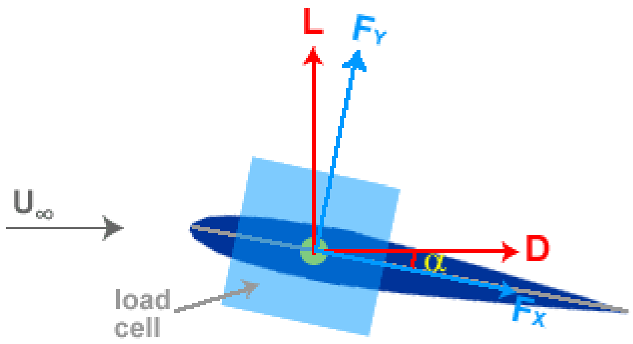

Figure 3.1 A schematic of load cell orientation

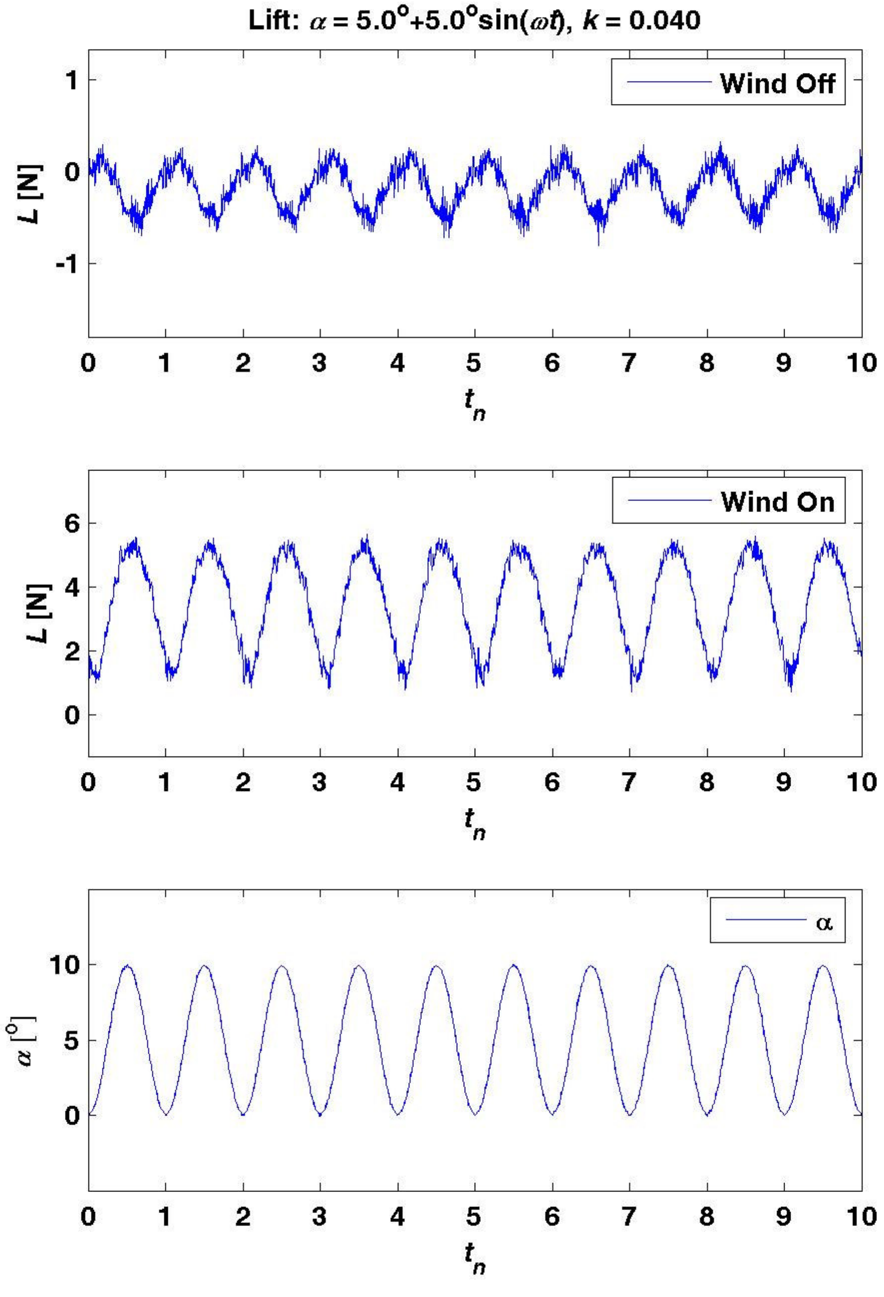

Figure 3.2 Lift time series under wind-off and wind-on conditions for Case 2 with *k* = 0.04

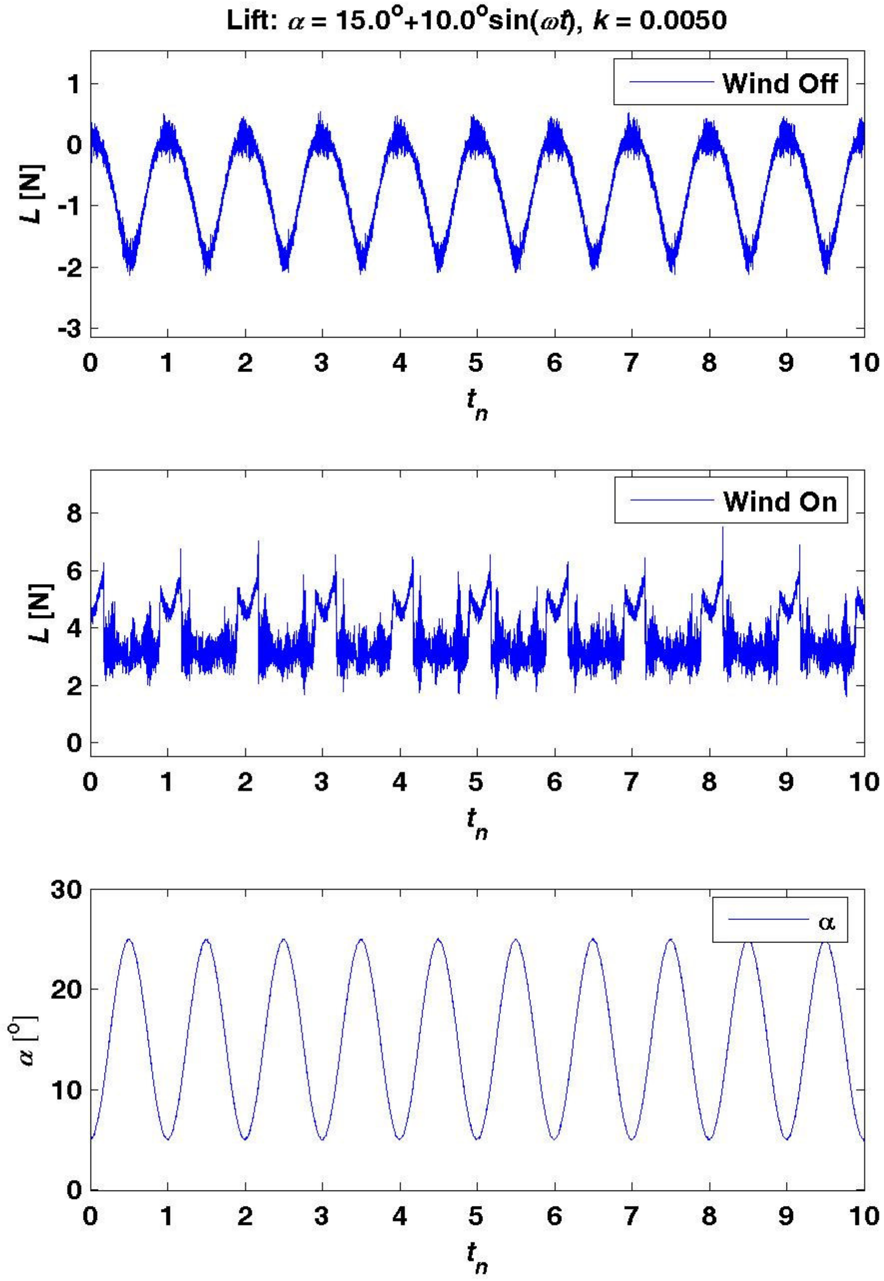

Figure 3.3 Lift time series under wind-off and wind-on conditions for Case 5 with *k* = 0.005

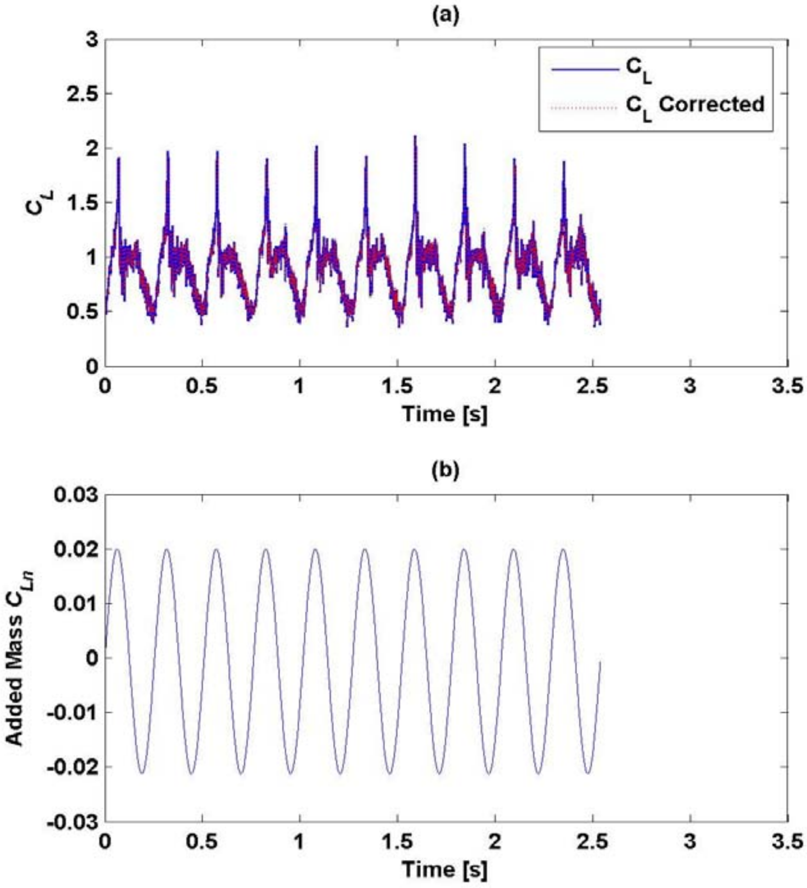

Figure 3.4 (a) Net C_L compared with net C_L corrected with apparent mass effect (b) net C_L corrected with apparent mass effect normalized by (1/2)*maximum net C_L

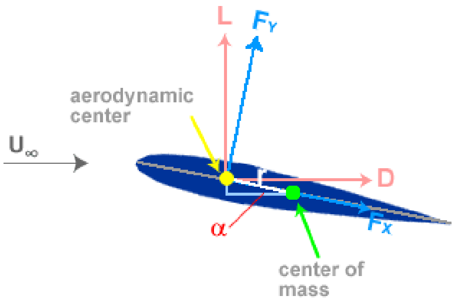

Figure 3.5 Torque about aerodynamic center of the airfoil

CHAPTER 4 RESULTS AND DISCUSSIONS

The present experiment is carried out at a relatively low Reynolds number, namely, Re = $7.7\text{x}10^4$, while most experiments on dynamic stall are carried out in Re much higher than 10^5. This choice of Re is important for the study of micro aerial vehicles (MAV) where the Re ranges from 10^4 to slightly larger than 10^5. Since there are few reported measurements of dynamic stall in this lower Re range, the present investigation intends to provide some insight into the behavior of dynamic stall at low Re. In view of this, it is important to examine the steady lift as well as the unsteady lift experienced by the airfoil as a function of the angle of attack α. Therefore, this chapter will focus only on the measured lift results, steady as well as unsteady lift, and the nonstationary and nonlinear behavior of the lift when the airfoil undergoes dynamic stall at low Re. The drag results will not be analyzed in this thesis, but they will be reported in subsequent papers arising from this research.

Flow visualization images are used to corroborate the lift results and the corresponding flow visualization results are presented along with the lift force data for representative cases. Since the experiment is carried out at Re = $7.7\text{x}10^4$, the behavior of the steady lift at this Re needs to be examined first. Consequently, the steady lift measurement results are first discussed with an objective to show that the theoretical lift curve is recovered, even at this Re. This is followed by a discussion of the unsteady lift measurements and their spectral contents, and finally the stationary/nonstationary and linear/nonlinear behavior of the lift signals.

Both FFT-based spectrum analysis and continuous wavelet analysis (CWT) of the lift signals are carried out in order to decipher the true character of the unsteady force signals. A single time-stationary (periodic) energy is input to the airfoil by the pitching system in all cases. It is expected that this input energy will show up prominently in any force spectrum. While the results of the FFT-based spectral analysis show peaks at the pitching frequency as well as the dominant frequency of lift (or drag) and at other higher harmonics (if present) on the power spectra density plots of the stall cases, the results of the CWT analysis of the same signals show power variation during one pitching cycle. This indicates that the measured force signals for the stall cases are essentially nonstationary. On the other hand, similar analysis of the force signals of the pre-stall cases reveals that the CWT and FFT results are identical, thus suggesting that the signals are essentially time stationary. The interaction of frequencies and energy transfer between frequencies are analyzed in the stall cases. It is hoped that, through this analysis, a deeper understanding of the aerodynamic response of the airfoil at dynamic stall could be gained and a better understanding of the nonlinear nature of dynamic stall could be obtained.

4.1 Steady Lift Measurements

The results of the steady lift measurements and flow visualization are shown in Figure 4.1 and Figure 4.2, respectively. Lift increases progressively with α and with a slope comparable to the theoretical slope of of 2π. It is clear that stall occurs at $\alpha = 10^\circ$ (Figure 4.1). The corresponding flow visualization images of the airfoil being held at fixed angles in the flow at Re = $7.7\text{x}10^4$ are shown in Figure 4.2. It should be pointed out the resolution of the images is not fine enough to indicate the formation of a separation bubble on the suction surface at $\alpha < \alpha_{ss}$. This does not mean that such a separation bubble does not exist (Mary and Sagaut, 2002). Nonetheless, according to these images, they show that the flow remains attached to the suction surface up to $\alpha = 10^\circ$. At $\alpha = 11^\circ$, the flow clearly separates from the suction surface. This observation is in agreement with the steady lift measurements and indicates that the lift of the airfoil reaches its maximum at $\alpha = 10^\circ$ before stall starts to set in. At first glance, this static stall angle seems to be small compared to other stall angles measured and reported in the literature (Carr ***et al.***, 1977, Martin ***et al.***, 1974). However, it should be noted that the Re for these other experiments ($10^5 < \text{Re} < 10^6$) are much higher than the present Re, which is set at Re = $7.7\text{x}10^4$. According to Leishman (2000), inertial effect in the flow increases with Re. It dominates over the viscous effect and thins the boundary layer at higher Re. In other words, the flow has more energy to overcome the momentum deficit created by viscosity. Consequently, the onset of flow separation is delayed to a higher α and a higher lift coefficient is measured at stall. Therefore, a higher static stall angle of the same airfoil ($\alpha_{ss} = 15^\circ$) is observed at higher Re as reported in most literature. Since the present experiments are conducted at Re = $7.7\text{x}10^4$, a measured $\alpha_{ss} \approx 10^\circ$ is reasonable. Furthermore, this value is consistent with that reported by White (1979).

4.2 Evaluation of the True Aerodynamic Response

Two important issues must be addressed before moving on to the discussion of the unsteady lift measurements. The first is the determination of the true aerodynamic responses from the measured signals. As mentioned in Chapter 3, in order to obtain the pure aerodynamic response of a pitching airfoil, both wind-on and wind-off experiments are carried out. In this section, the presence of the aerodynamic response in the wind-on signals is studied. The time series of the wind-on and wind-off signals are compared in terms of their shape and magnitude. Power spectral analysis via CWT is also carried out to observe their difference in frequency content thus to validate the presence of aerodynamic response in wind-on signals. Hence by subtracting the wind-off signals from the wind-on signals, the true aerodynamic responses can be obtained. After this analysis, the true aerodynamic lift acting on the airfoil is available. The method and procedure to deduce the lift is also discussed in this section.

The second is the classification of the numerous runs carried out during the course of this experiment so that the lift signal can be analyzed to gain insight into the low Re dynamic stall behavior. From Table 3.1, the five runs can be classified into two different groups: the pre-stall cases and the stall cases. This classification uses α_{ss} to define stall. Therefore, the term pre-stall cases referred to those cases in which the airfoil is oscillated below, or up to, the static stall angle, i.e., $\alpha_{ss} = 10^\circ$, and no lift stall is observed. This group includes Cases 1 and 2 in the present study. The stall cases referred to those cases in which the airfoil is pitched to beyond α_{ss} (Cases 3, 4 and 5). Within this group, the various cases can be further classified into the light stall case (Case 3) and the deep stall cases (Cases 4 and 5). Since the light stall case is inherently different from the deep stall cases, the following discussion will consider the cases of pre-stall, light stall and deep stall separately. The characteristics of the aerodynamic lift response of the pre-stall, light stall and deep stall cases are discussed in the next section.

4.2.1 The Actual Aerodynamic Lift Response

Time series of the lift signals of selected cases are shown in Figure 4.3 to Figure 4.5. Clearly, all wind-on signals are much greater in magnitude compared to their wind-off counterparts. For Case 2 at k = 0.04 in Figure 4.3, both wind-on and wind-off signals of the pre-stall cases resemble the shape of a sinusoidal signal, but the peak-to-trough magnitude of the wind-on signal is four times of that of the wind-off signal. Figure 4.4 and Figure 4.5 shows that the wind-on signals of the light stall (Case 3) and deep stall (Case 5) cases no longer resemble a sinusoidal signal; instead sharp peaks of the signals are observed. These sharp peaks are not observed in the wind-off signals of the corresponding cases; hence undoubtedly, these sharp peaks in the wind-on signals are caused by aerodynamic responses of the airfoil.

Further evaluation of the aerodynamic response in the wind-on signals are carried out by implementing CWT analysis on both wind-on and wind-off lift signals to observe the difference in their frequency content. The results of the wavelet analysis of the lift signals are presented in Figure 4.6 to Figure 4.8 in the form of time-frequency spectra, or spectrograms. In order to directly compare the power of the wind-on and wind-off signals, the magnitude of power is not normalized by the maximum power of each signal. These contour maps show power variation of frequencies of the force signals from t_n = 0 to t_n = 10.

Figure 4.6 shows the spectrogram of the pre-stall case of Case 2 at k = 0.04. Under wind-off conditions, the only observable peak is found at f_n = 1 (pitching frequency), which clearly is due to the pitching motion of the airfoil driven by the pitching mechanism. Under wind-on condition, a peak is also observed at f_n = 1, but its magnitude is higher than its counterpart in the wind-off condition. Moreover, peaks of higher frequencies are observed. It is obvious that the wind-on signals have captured the aerodynamic responses of the airfoil. These details of the spectral content are revealed in the spectrogram of the wind-on cases but are not seen in the wind-off cases.

Similar to the pre-stall cases, a higher power peak is observed at f_n = 1, under both wind-off and wind-on conditions, in the spectrograms of the lift signals of Case 3 and Case 5 in Figure 4.7 and Figure 4.8 respectively. In addition, some higher frequency peaks are observed under wind-off condition for Case 5. Nonetheless, the same peaks are also present under wind-on condition of the same case. Under wind-on condition, power peaks are found at frequencies other than f_n = 1, which are not observed under wind-off condition. Effects on power concentrations contributed by aerodynamic responses are pronounced in these cases, and the presence of aerodynamic responses in wind-on signals is therefore ascertained.

The net lift of all cases is then obtained by subtracting the wind-off lift from the wind-on lift, as described in Section 3.2.1 and frequency analysis is carried out. By studying the net lift spectra, power of different frequencies and its variation over time due to aerodynamic forces can also be examined and the results will be presented in later sections.

4.3 Unsteady Lift Measurements

All load cell force signals are analyzed to obtain the true lift signal as suggested in the former section. Once the true lift signals are obtained, they are classified into three groups; the pre-stall cases, the light-stall case and the deep-stall cases. In this section, the lift signals for these three different groups are analyzed and reported accordingly.

4.3.1 Pre-stall

The true lift signals for Case 1 and Case 2 are shown in Figure 4.9 and Figure 4.10. These plots give the variation of C_L with the instantaneous α of the airfoil. There are four panels in each figure and each panel is meant for one reduced frequency k of the pitching motion. Altogether four pitching frequencies have been investigated for Case 1 (Figure 4.9) and Case 2 (Figure 4.10). The behavior in Case 1 and Case 2 is essentially the same. At $k = 0.005$, which is the lowest k tested, the unsteady lift follows the static lift curve during both upstroke and down-stroke. However, C_L is lower in the upstroke than its corresponding down-stroke value during one cycle of the oscillation of the airfoil.

At higher k, the departure of C_L from the static lift curve becomes more significant. The lift during upstroke further decreases in magnitude with increasing k, while the C_L during down-stroke further increases in magnitude. Figure 4.11 shows the flow visualization images of Case 2 at $k = 0.04$. It is observed that a flow reversal occurs when the airfoil is being pitched to above 5° but the flow remains attached to the suction surface of the airfoil during the entire cycle of oscillation.

According to Theodorsen's theory as described in Leishman (2000), the unsteady lift curves for pre-stall cases with small k are shown in Figure 4.12. When $k = 0$, the model yields the static lift curve. As k increases, the lift plots evolve into counterclockwise hysteresis loops with the instantaneous lift lower than the steady value when the pitching is upward and higher than the steady value when the pitching is downward. Theodorsen's function takes into account the flow acceleration effects (i.e. a non-circulatory or apparent mass effect) and the creation of circulation around the airfoil (i.e circulatory effect) for an airfoil undergoing a simple harmonic motion. The curves displayed in Figure 4.12 are for the same sinusoidal variation of α as in Case 2 but with greater values of k. It can be seen that the characteristics of the measured lift curves for Case 2 are in good agreement with that given by Theodorsen's model (Figure 4.12).

4.3.2 Light Stall

When dynamic stall occurs, the lift stalls and the flow remains separated until the airfoil is pitched down to an angle lower than the static stall angle α_{ss}. At a lower angle in the down-stroke, the flow reattaches and the lift readjusts to its pre-stall level. Dynamic stall of the airfoil is observed in Cases 3, 4, and 5 when the airfoil is pitched to α beyond α_{ss} at 10˚ with a significant increase in C_L and is followed by an equally abrupt drop.

In Case 3, an increase in the delay of the stall angle is noted with an increasing k (Figure 4.13). When $k = 0.005$, the airfoil stalls at about $\alpha = 11.5$˚; this is followed by a drop in C_L to the same level as the steady lift curve and remains with the steady lift curve for the rest of the upstroke motion. At this k, the unsteady C_L returns to its pre-stall value at 8° in the down-stroke, which is below α_{ss} = 10°, and continues for the rest of the pitching down-stroke motion with C_L higher than its steady state counterpart. Flow Visualization images at this k are shown in Figure 4.14. From the images, it can be seen that at α = 11.3°, during upstroke, the flow is still attached to the suction surface of the airfoil. Again, it should be pointed out that possibly a separation bubble could be formed on the suction surface, but the flow visualization images fails to properly resolved it. However, at α = 12.2°, it is clear that the flow has separated from the airfoil suction surface. It is evident that dynamic stall is associated with flow separation from the airfoil surface and this separation that brings about a reduction in C_L.

At k = 0.01, the lift behavior is very similar to that of the case at k = 0.005. However, the stall angle is further delayed to beyond α = 12.1° and C_L does not return to its static value until the airfoil is being pitched down to 8°. At k = 0.02, the stall is delayed to α = 13.1°, C_L returns to its pre-stall value at α = 6° and finishes the rest of the pitching down-stroke motion with C_L higher than the corresponding steady C_L.

At k = 0.04, lift stall is delayed to α = 14.2°, which is the highest stall angle for all k values of Case 3. During upstroke, C_L is lower than the corresponding steady C_L. However, as the airfoil pitches up to right before stall, C_L overshoots substantially and this is followed by an abrupt stall. It can be seen from the flow visualization images in Figure 4.15 that the flow completely separates from the suction surface of the airfoil at $\alpha = 14.2^\circ$. In this case, the lift rarely readjusts to its pre-stall value during the entire down-stroke and the C_L curve takes the shape of a big loop.

4.3.3 Deep Stall

Similar behavior is observed in Case 4 (Figure 4.16) and Case 5 (Figure 4.17). In Case 4, at k = 0.005 and k = 0.01, the unsteady C_L in the pre-stall regime is higher than its steady state values during upstroke (Figure 4.16). After the airfoil stalls at α_{ss} C_L follows closely the post-stall steady state values. However, the occurrence of lift recovery is delayed to $\alpha = 5^\circ$. At k = 0.01, C_L overshoots and stall occurs at $\alpha = 11.2^\circ$, while the flow reattaches at $\alpha = 4^\circ$ during the down-stroke of the pitching motion. At k = 0.02, lift stall is further delayed to $\alpha = 13.6^\circ$ but the flow does not reattach until the airfoil is pitched down to $\alpha = 2^\circ$. At k = 0.04, the unsteady C_L in the pre-stall region has a lower value compared to the steady state value at the same instantaneous α. After passing a_{ss}, C_L continues to climb and reaches its maximum at $\alpha = 18.0^\circ$. After the abrupt drop from its maximum, the unsteady C_L remains low until the airfoil completes the entire down-stroke motion.

In Case 5, for k = 0.005 and k = 0.01, the C_L characteristics resemble those of Case 4 at the same k (Figure 4.17). As k increases to k = 0.02, the unsteady C_L has higher values than those of the steady C_L throughout the entire pre-stall regime during upstroke. The increase in C_L becomes steeper at $\alpha = 12^\circ$ and C_L reaches its maximum value at about $\alpha = 13^\circ$ where stall occurs. The C_L does not recover to its pre-stall value for the remainder of the down-stroke. Further increase of k to k = 0.04 leads to the unsteady C_L slope resembling that of the steady C_L slope during upstroke. A sudden increase of C_L occurs at $\alpha = 15^\circ$ which is followed by a maximum lift at $\alpha = 16.2^\circ$. Similar to the $k = 0.02$ case, the C_L does not return to its pre-stall value for the remainder of the down-stroke.

4.3.4 Effects of Reduced Frequency on Stall Angle, Maximum Lift and Lift Recovery

The pitching motion depends on three parameters; these are the mean angle, the amplitude of the oscillation and the frequency of oscillation or k. Having examined the behavior of C_L for different pitching motions and during one pitching cycle for different k, the next step is to investigate the effect of these three parameters on the dynamic stall behavior. The first task is to examine the effect of k on the dynamic stall angle. Using the information obtained from the previous analysis, a plot of the dynamic stall angle versus k can be made for the three stall cases investigated above. The plot is shown in Figure 4.18. From this figure, it can be observed that the stall angle increases as k increases. It is also observed that the stall angle does not vary linearly with reduced frequency except for Case 4. An increase in k indeed does not guarantee a significant delay in stall angle as it is in Case 5 with $k = 0.005$ and $k = 0.01$. Nonetheless, the underlying reasons of this behavior are not known and further investigation is required.

The next step is to examine the effect of k on C_{Lmax}, the maximum lift. A plot of C_{Lmax} versus k is shown in Figure 4.19. For Case 1 and Case 2, the results show that k has little or no effect on C_{Lmax}. Once α has passed α_{ss}, dynamic stall occurs and increasing k gives rise to increasing C_{Lmax}. The increase is essentially linear for the three stall cases studied; however, the slope for Case 3 is much smaller than that for Case 4 and Case 5.

It can be seen increasing k also has an effect on C_L recovery. A plot of the C_L recovery versus k made for the three stall cases studied is shown in Figure 4.20. As k increases, the airfoil has to be pitched down to a lower α before the flow reattaches. Increasing k essentially further delays the C_L recovery from stall and enlarges the hysteresis loops. Indeed, in Case 3 at k = 0.04 and in Case 5 at k = 0.02 and k = 0.04, C_L does not recover to its pre-stall value during down-stroke and lift recovery occurs when the airfoil is being pitched up again. Therefore no lift recovery angle is shown in the figure for these two cases at the corresponding k's.

Besides this result, other observation can be made concerning dynamic stall behavior as k increases. In general, the magnitude of C_L in the pre-stall regime during upstroke decreases with increasing reduced frequency, from k = 0.005 to k = 0.04. The only exception is Case 5.

4.3.5 Effects of Mean Angle and Amplitude of Oscillation on Dynamic Stall

Having examined the effect of k on dynamic stall, the next task is to focus on the effect of the mean angle, α_{mean}, and the amplitude of the pitching oscillation, α_{amp}, on dynamic stall. The α_{mean} and the α_{amp} determine the excursion of the airfoil beyond α_{ss} before stall actually occurs. There are two stall cases where the α_{mean} is the same but the α_{amp} is different. These two cases are Case 3 and Case 4 which the latter case has a larger α_{amp}. A comparison of these two cases therefore could shed light on the effect of α_{amp} on dynamic stall. Comparing Case 3 and Case 4, it can be seen that the lift hystereses are comparable in shape at the same k, but the lift hystersis loops are larger in Case 4 (Figure 4.16) than in Case 3 (Figure 4.13). At higher k, C_{Lmax} of Case 4 is significantly higher than that of Case 3 (Figure 4.19), and lift stall of Case 4 is delayed to higher angle of attack, while in Case 3, stall occurs almost at the maximum α (= 15°) the airfoil could reach (Figure 4.18). Indeed, the lift stall of Case 3 at k = 0.04 is a forced stall. At all k investigated for Case 4, lift is able to recover to its pre-stall values during down-stroke, while in Case 3, even at k = 0.04, lift fails to replicate the same trend (Figure 4.20).

Two cases have the same α_{amp} but different α_{mean}; they are Case 4 and Case 5. Therefore, a comparison of these two cases will shed light on the effect of α_{mean} on dynamic stall. It is found that the C_L curves exhibit similar trend at the same k (Figure 4.16 and Figure 4.17). Figure 4.18 and Figure 4.19 show that α_{mean} has a slight effect on the dynamic stall angle but little or no effect on C_{Lmax}. However, for all k investigated in Case 4, after the airfoil stalls, it is able to regain the C_L magnitude of its pre-stall value during down-stroke, while in Case 5, even at higher k, the airfoil stalls and is not able to regain the C_L magnitude of its pre-stall values (Figure 4.20). Hence, single loops of lift curves are formed when the airfoil is pitched at higher k, and maximum C_L and maximum α_{ss} occur in k = 0.04 for both cases.

4.4 Power Spectral Analysis

The dynamic stall behavior as exemplified by the lift curve during one cycle of pitching has been examined in detail in the preceding section. More detailed information of the energy transfer between fluid and airfoil and between different frequencies will have to be obtained from an analysis of the spectral contents of the measured lift signals. In the present study, the airfoil undergoes forced-pitching oscillation. During one cycle of oscillation of the airfoil, energy is constantly supplied to the airfoil by the pitching system. This is evident by the prominent peak at the pitching frequency observed in the power spectrum of the lift responses at all time during one cycle of oscillation of all cases under both wind-on and wind-off conditions as seen in Section 4.2.1. The aim of the present analysis is to characterize the unsteady force signal and thus the physics of dynamic stall through a detailed analysis of the spectral contents of the lift signals.

As mentioned before, two different spectral analysis methods are used to carry out the investigation; one is the FFT which is most suited for stationary signals, another is the CWT which is used to study nonstationary signals. In the latter technique, as explained in previous sections, spectrograms are calculated to show the true nature of the analyzed signal. If the signal is stationary, the spectrogram will not vary with time. In other words, the same spectrum will be obtained for all periods of time investigated. The extent of the variation indicates the nonstationary nature of the analyzed signal. In the following, the FFT-based spectral analysis is first used to analyze the signals and this is followed by a CWT analysis. This way, the true nonstationary nature of the lift signal could be discovered and verified.

4.4.1 FFT-Based Power Spectral Analysis

Some sample results of the FFT-based power spectral analysis of the lift signals over ten cycles of oscillation (from $t_n = 0$ to $t_n = 10$) are shown in Figure 4.21 to Figure 4.25.

These representative plots cover Case 1 to Case 5; the *k* values chosen are indicated in the plots. As expected, a prominent peak is observed in all the power spectra of the lift signals at f_n = 1 for both pre-stall cases and stall case due to the energy input at the pitching frequency. For the pre-stall cases, very small amplitude peaks are discernable at f_n = 3 in Figure 4.21 and at f_n = 2 in Figure 4.22. In spite of these very small peaks at different frequencies, the spectra are fairly typical of those obtained from stationary signals. Further analysis of these signals will be carried out using CWT to ascertain the true stationary nature of the lift signals for the re-stall cases.

As for the light-stall and deep-stall cases, some interesting results could be gleaned from these FFT-based power spectra. Again, their stationary nature will be analyzed using CWT. Peaks are observed at higher harmonics of f_n for all three stall cases investigated. For Case 3 at *k* = 0.02, high power peaks are observed at f_n = 1, 2 and 3 with smaller peaks observed at other higher harmonics of f_n (Figure 4.23) For Case 4 at *k* = 0.04, high power is seen at the pitching frequency and its first and second harmonics, with other observable peaks at higher harmonics of f_n (Figure 4.24). As for Case 5 at *k* = 0.005, power is highly concentrated at f_n = 2 and f_n = 5, while the peak at f_n = 1 is only of moderate power (Figure 4.25). Other peaks are also observed at higher harmonics of f_n. These multiple frequency contents tend to indicate that the signals are not quite stationary, therefore, further analysis of them need to be carried out using CWT.

Since the airfoil is pitched sinusoidally by the pitching mechanism at f_n = 1, a single time-stationary energy is being input to the system, and one and only one peak should be observed, i.e. f_n = 1, on the power spectra. This is the case for Case 1 and

Case 2, where energy is being supplied to the system by the pitching mechanism at f_n = 1. On the other hand, for Case 3, Case 4 and Case 5 at the reduced frequencies shown, besides a single time-stationary energy input, peaks at higher harmonics are observed in the power spectra. Since results of FFT-based spectral analysis show only the frequencies where high power can be found, variations of power with time cannot be determined. It is not known whether the higher power occurring at higher harmonics persist during the entire cycle of oscillation or only exist for some portion of the cycle. There is insufficient information to indicate the stationary nature of lift at these higher harmonics. Hence, further investigations of the lift at higher frequencies are carried out using CWT.

4.4.2 CWT-Based Power Spectral Analysis

Selected spectrograms of the wavelet analysis of 10 cycles of oscillation (from t_n = 0 to t_n = 10) of the lift signal are illustrated in Figure 4.26 to Figure 4.30. A frequency range up to ten times of f_n is examined. For the pre-stall cases, spectrogram results are in good agreement with the FFT-based power spectra. The spectrograms essentially show no variation within one cycle and over the 10 cycles of oscillation examined. This is a clear indication that the lift signals are stationary. A persistent peak of lift shows up at f_n = 1 for Case 1 at k = 0.01 (Figure 4.26) and for Case 2 at k = 0.04 (Figure 4.27) as expected. This shows that while energy is input into the airfoil at f_n = 1, the resulting lift at f_n = 1 dominates the spectra. In addition, this peak at f_n = 1 persists during the entire pitching cycle and the magnitude of the peak remains unchanged. Furthermore, the behavior is not affected by k. Thus the signal is typical of that observed for the lift measured ahead of α_{ss}, which is stationary and there is no energy transfer between frequencies. These results imply that the dynamic phenomenon is essentially a linear one and is consistent with the linear airfoil theory; consequently, the C_L slope is 2π. However, the same behavior is not observed for the stall cases analyzed; the spectrograms clearly show variations with respect to time within each cycle of oscillation and over the 10 cycles examined (Figure 4.28 to Figure 4.30).

For Case 3 at $k = 0.02$, high power is observed at $f_n = 1$ as expected (Figure 4.28). But some peaks are also observed at $f_n = 2$ and at $f_n = 3$, although these peaks do not persist for all 10 cycles of the time series examined. A band of higher power is also found at frequencies stretching from $f_n = 4$ to $f_n = 10$. However, the power level of these higher frequencies alternates from high to low and to high again. Similarly, for Case 4 at $k = 0.04$, alternate bands of higher power is also found at frequencies stretching from $f_n = 3$ to $f_n = 10$, along with the persisting peaks observed at $f_n = 1$ and at $f_n = 2$ (Figure 4.29). At a frequency near $f_n = 3$, higher power are also observed but this peak is not present for all 10 cycles of time series examined. For Case 5 at $k = 0.005$, at a frequency near $f_n = 5$, high power is observed but it is not present in each of the 10 cycles of time series examined (Figure 4.30). Alternate bands of high power are also found.

Close examination of the spectrogram reveals that the higher power, i.e. higher frequencies, indeed occurs periodically. From these results, it can be seen that the higher power are associated with higher harmonics of f_n observed in the power spectrum computed using FFT-based analysis. However, they are not present in each of the 10 cycles examined. Therefore, these spectrograms indicate that the lift signals for both light stall and deep stall cases are nonstationary and possibly nonlinear. In order to further ascertain this nonstationary/nonlinear behavior, a more detailed analysis of these lift signals is given below.

4.5 Further Analysis of the Lift Signals

In view of the observed power variation of the lift signals at higher frequencies, further investigations are made to study the nonstationary and nonlinear nature of the lift, thus energy, of the pre-stall and stall cases. Interesting observations are made when studying the location of the peaks as a function of instantaneous α within one cycle of oscillation. Slices of the spectrograms at selected instantaneous time give the power spectral density with frequency at that time. Temporal variation of the spectrum can thus be examined in detail. In the following, selected stall cases are examined first to ascertain the nonstationary and nonlinear nature of the lift signals. This is followed by a more detailed analysis of both the pre-stall and stall cases.

4.5.1 Nonstationary Behavior of the Stall Cases

In order to identify nonstationary behavior of the deep-stall cases, the power spectra of these cases are studied first. The power spectra at nine selected instantaneous times during one cycle of oscillation for Case 4 at k = 0.04 and for Case 5 at k = 0.005 are shown in Figure 4.31a to Figure 4.31i and Figure 4.32a to Figure 4.32i, respectively. Each of the nine selected times are separated by one-eighth of a period within each cycle of oscillation.

For Case 4 at $k = 0.04$, peaks are observed at $f_n = 1$, $f_n = 2$, and $f_n = 3$ at all selected times within one cycle of oscillation (Figure 4.31a-i). However, the peak at $f_n = 3$ becomes less and less prominent as α increases during upstroke, but regains its sharpness in the down-stroke. Consider the peak between $f_n = 4$ and $f_n = 5$ occurring at $\alpha = 0.0^\circ$, the magnitude of the peak decreases with increasing α and the peak becomes non-distinguishable at $\alpha = 17.1^\circ$ and beyond. During down-stoke, a peak between $f_n = 5$ and $f_n = 6$ appears at $\alpha = 17.3^\circ$ and $\alpha = 10.5^\circ$, but it flattens out at $\alpha = 3.0^\circ$. Finally, when the airfoil reaches its minimum α at 0.0°, a peak reappears at between $f = 4$ and $f_n = 5$. This variation is evidence that the lift signal is essentially nonstationary within one cycle of oscillation of the airfoil.

For Case 5 at $k = 0.005$, prominent peaks are observed at $f_n = 1$, $f_n = 2$, and $f_n = 3$ at all selected times within one cycle of oscillation (Figure 4.32a-i). At the minimum α, a pronounced peak is found at around $f_n = 5$, while a smaller peak is observed between $f_n = 8$ and $f_n = 9$. As α increases, both peaks lose their magnitude and at $\alpha = 15.1^\circ$, the peak between $f_n = 8$ and $f_n = 9$ completely disappears while the peak at $f_n = 5$ remains but with a smaller magnitude. As α continues to increase, new peaks are observed between $f_n = 3$ and $f_n = 4$, and near $f_n = 7$. In addition, it is observed that the peak at $f_n = 2$ has higher magnitude than that at $f_n = 1$. Again, these variations clearly show that the lift signal is nonstationary even within one cycle of oscillation.

The power spectra at nine selected instantaneous times during one cycle of oscillation for Case 3 at $k = 0.02$ are shown in Figure 4.33a to Figure 4.33i. Although not as obvious as in the deep stall cases studied, the magnitude of the higher frequencies is found to change with time within one cycle of oscillation. At $\alpha = 13.4^\circ$, the magnitude of $f_n = 5$ to $f_n = 10$ is at its highest. During other times, a peak is observed at $f_n = 5$ when the magnitude of higher frequencies remain small. It is clear that the lift signal of both of the light stall cases and the deep stall cases is also nonstationary within one cycle of oscillation.

4.5.2 Nonstationary and Nonlinear Behavior of the Lift Signals

To further investigate the stationary/nonstationary and nonlinear behavior of an airfoil undergoing dynamic stall, CWT analysis of all cases at all reduced frequencies investigated are carried out and the results, including both pre-stall and stall cases, are displayed in Figure 4.34a-d to Figure 4.38a-d. Spectrogram, the variation of C_L and α with time within one cycle of oscillation are presented in each figure. Both the spectrogram and the C_L variation are plotted over the same time scale. There are five sets of figures, one for each case studied. In the following presentation, the five cases are divided into two groups for discussion. The reason is that the characteristics of the lift signals are quite similar within each group. The first group is the pre-stall cases, i.e., Case 1 and Case 2, while the second group includes the light-stall and deep-stall cases, i.e., Case 3, Case 4 and Case 5.

4.5.2.1 Pre-stall Cases

As seen in Figure 4.34a to Figure 4.34d for Case 1 and Figure 4.35a to Figure 4.35d for Case 2, the spectrogram shows a constant energy level over one cycle and there is only prominent peak observed at $f_n = 1$. This denotes that while energy is input into the airfoil at $f_n = 1$, the resulting lift at $f_n = 1$ dominates the spectra. In addition, this peak at $f_n = 1$ persists during the entire pitching cycle and the magnitude of the peak remains unchanged. Furthermore, the behavior is not affected by k. Thus, the signal is typical of that observed for the lift measured ahead of α_{ss}, is stationary and there is no energy transfer between frequencies. These results imply that the dynamic phenomenon is essentially a linear one and is consistent with the linear airfoil theory. Consequently, the C_L slope is 2π.

4.5.2.2 Light- and Deep-Stall Cases

Similar result for Cases 3 to 5 are shown in Figure 4.36a-d to Figure 4.38a-d, respectively. These cases differ from the results of Case 1 and Case 2 in several ways. The first difference is that there are two C_L peaks in one cycle compared to one peak for the pre-stall cases. For the light-stall case (Case 3), the first peak occurs around $\alpha = 11^\circ$ while this location of the first peak is decreased to about $\alpha = 10^\circ$ for the deep-stall cases (Case 4 and Case 5). The second peak occurs at $\alpha = 8^\circ$ for Case 3, but around $\alpha = 6.5^\circ$ for Case 4 and Case 5. Unlike the pre-stall cases, the location of these peaks change as k increases for all stall cases investigated. In other words, k has a definite effect on the behavior of the lift within one cycle of oscillation of the airfoil. However, this variation is less sensitive to changes in the amplitude of oscillation (compared Case 3 with Case 4).

The second difference is the time variation of the spectrogram within one cycle of oscillation (Figure 4.36a-d). While the level of the spectrogram remains essentially constant for the pre-stall cases, it varies significantly for the stall cases studied. The variation pattern differs from one k to the next and from one stall case to another. Similar behavior is observed in Case 4 (Figure 4.37a-d) and Case 5 (Figure 4.38a-d).

The third difference is the occurrence of a band of higher power at higher frequencies during upstroke followed by a second band near the end of the oscillation (Figure 4.36a-d). It is noted that the bands of higher power occur when there is a surge of lift during a cycle. When lift stalls, the high power is no longer seen at high frequencies. Energy is therefore transferred to other frequencies. Similar high power bands are found in Case 4 (Figure 4.37a-d) and Case 5 (Figure 4.38a-d) at the same k.

The fourth difference is the transfer of energy between frequencies for the stall cases. In Case 3 (Figure 4.36a) and Case 4 (Figure 4.37a) with $k = 0.005$, a lift peak occurs at $f_n = 3$ for the first half of the oscillation, but the power starts to diminish even before lift stall occurs. This indicates energy at $f_n = 3$ is being transferred to other frequencies. As k increases for Case 3, the surge of lift during down-stroke diminishes and the high power band during down-stroke disappears. It is also noticed that the lift at $f_n = 2$ and $f_n = 3$ decreases in power as k increases. Similar trend is observed in Case 4 except for $k = 0.04$. The same energy transfer between frequencies is also observed in Case 5. For example, at $k = 0.005$ (Figure 4.38a), it is noteworthy to observe that the spectrum is dominated by one peak at $f_n = 2$ and a significant peak around $f_n = 3$. The latter peak is not persistent and close to disappearing around mid cycle of the oscillation. Again, this shows that energy is transferred between frequencies.

It is obvious that compared to pre-stall cases, light-stall and deep-stall cases exhibit nonlinear behavior. The lift signals become nonstationary when the airfoil undergoes pitching motion that penetrates into the region beyond α_{ss}. In addition, energy transfer occurs between frequencies; thus the physics of the dynamic stall phenomenon can be said to be nonlinear.

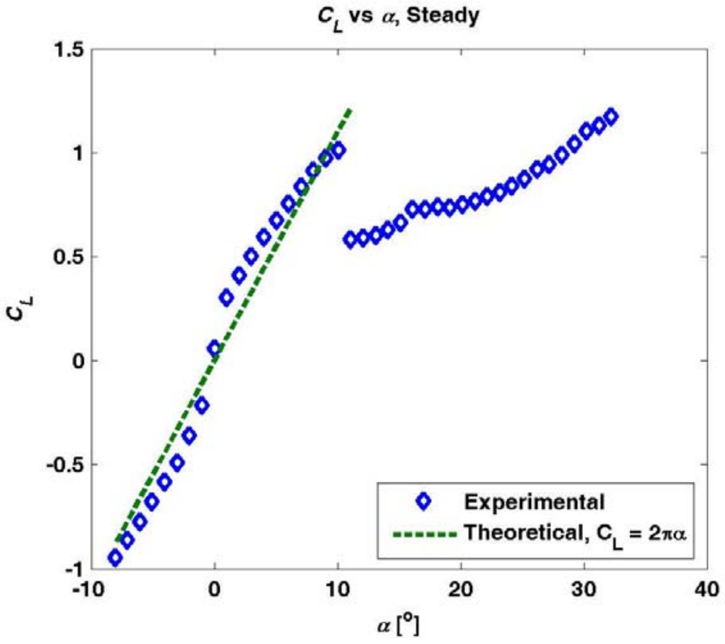

Figure 4.1 Steady C_L versus mean α

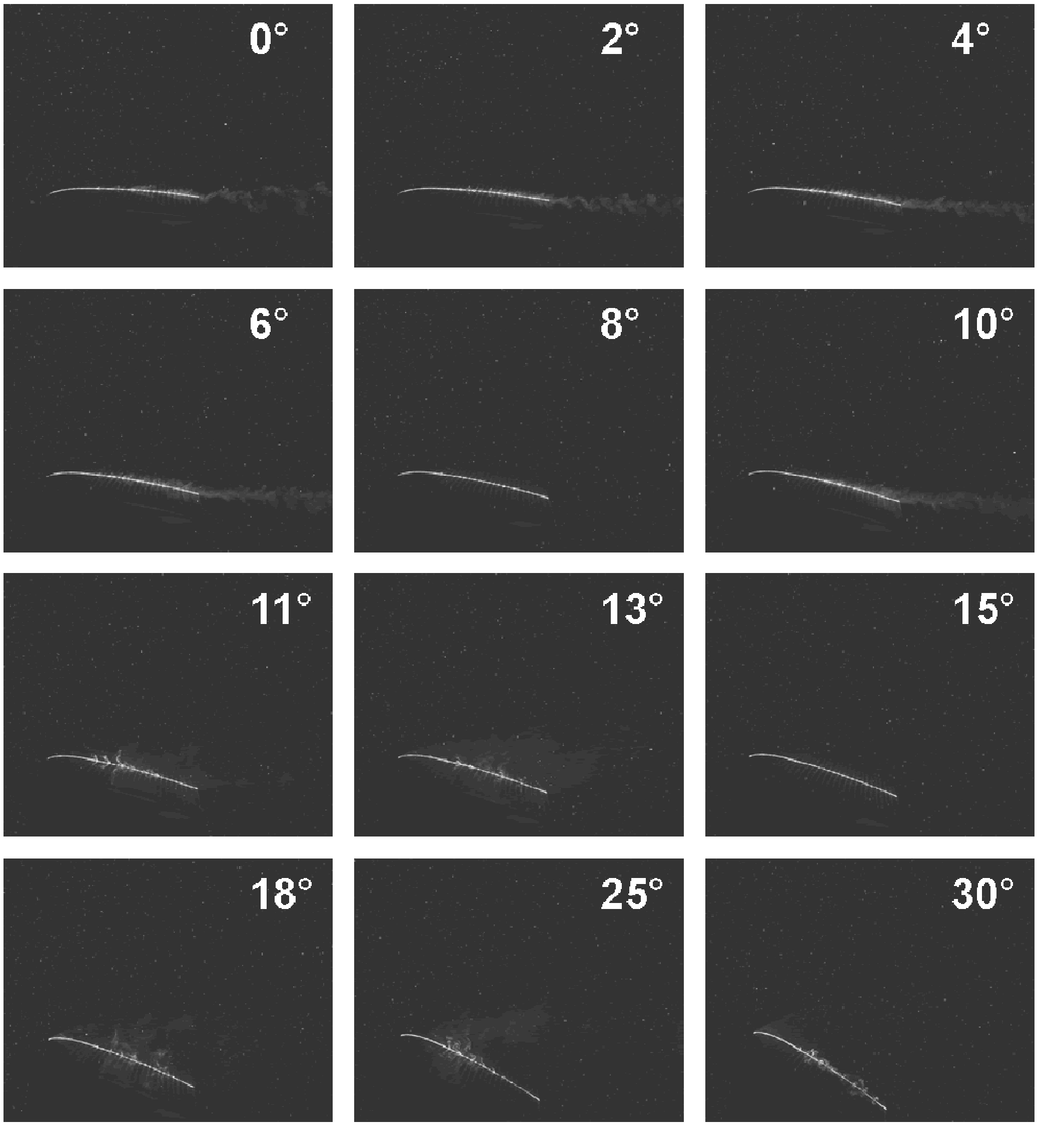

Figure 4.2 Visualization of the flow around a stationary airfoil at different mean α.

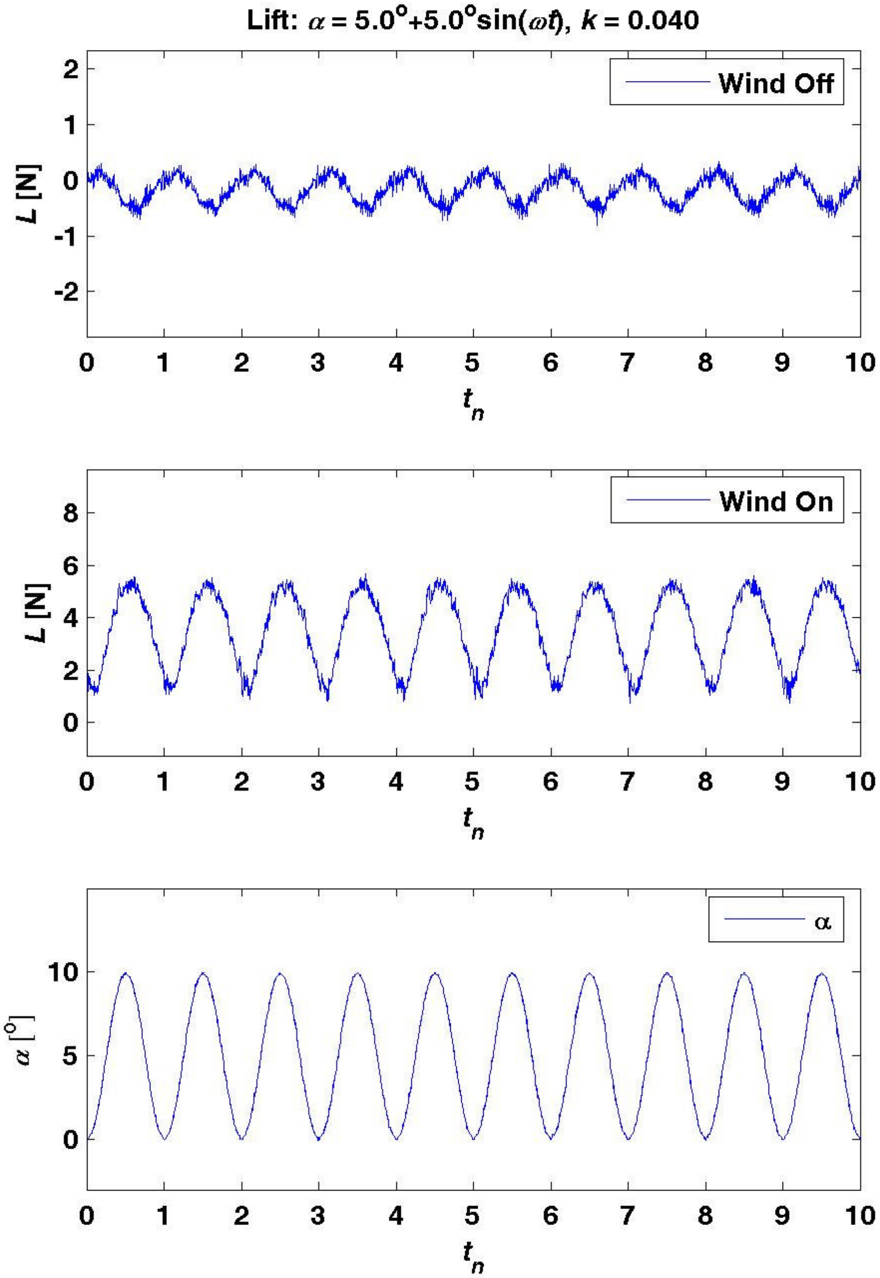

Figure 4.3 Lift time series under wind-off and wind-on conditions for Case 2 at *k* = 0.04.

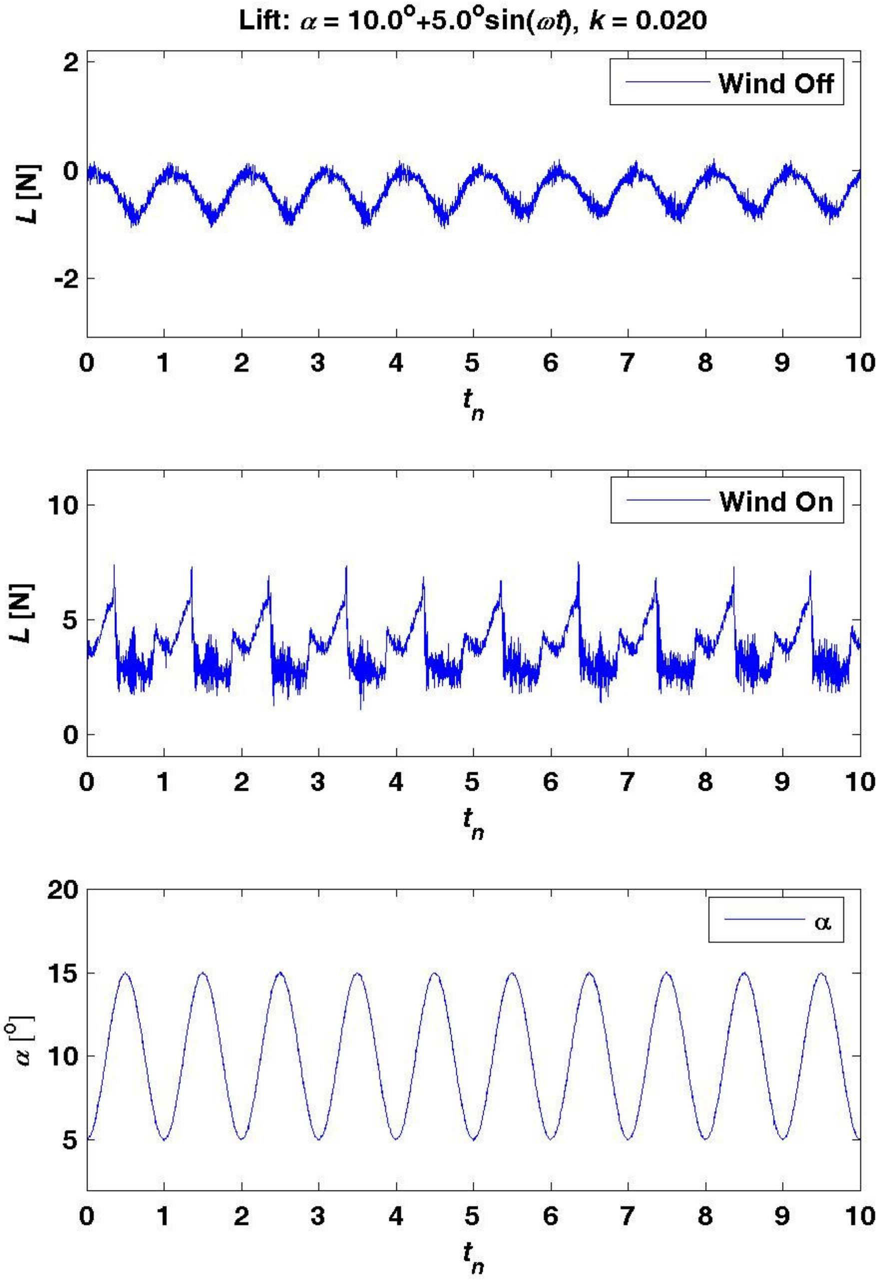

Figure 4.4 Lift time series under wind-off and wind-on conditions for Case 3 at *k* = 0.02.

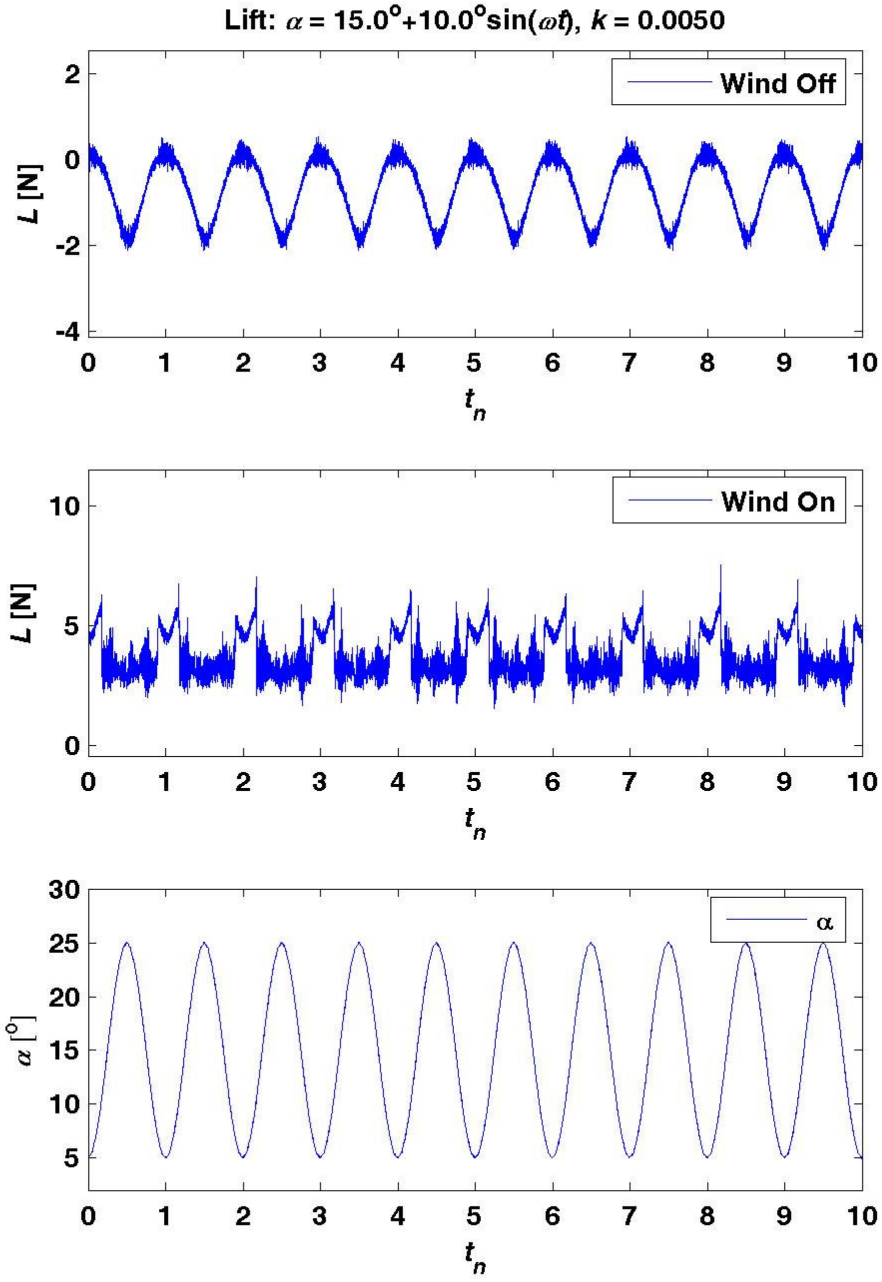

Figure 4.5 Lift time series under wind-off and wind-on conditions for Case 5 at *k* = 0.005.

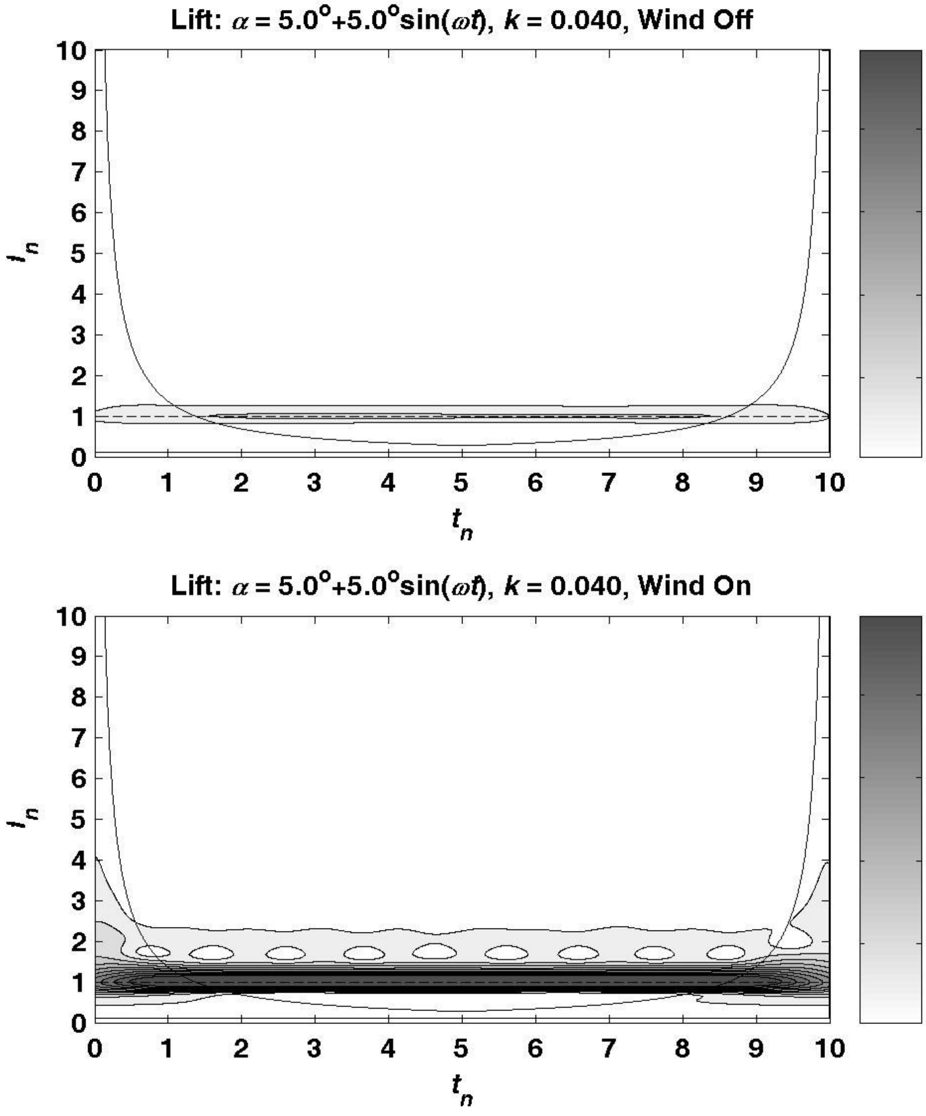

Figure 4.6 Spectrograms of lift under wind-off and wind-on conditions for Case 2 at *k* = 0.04.

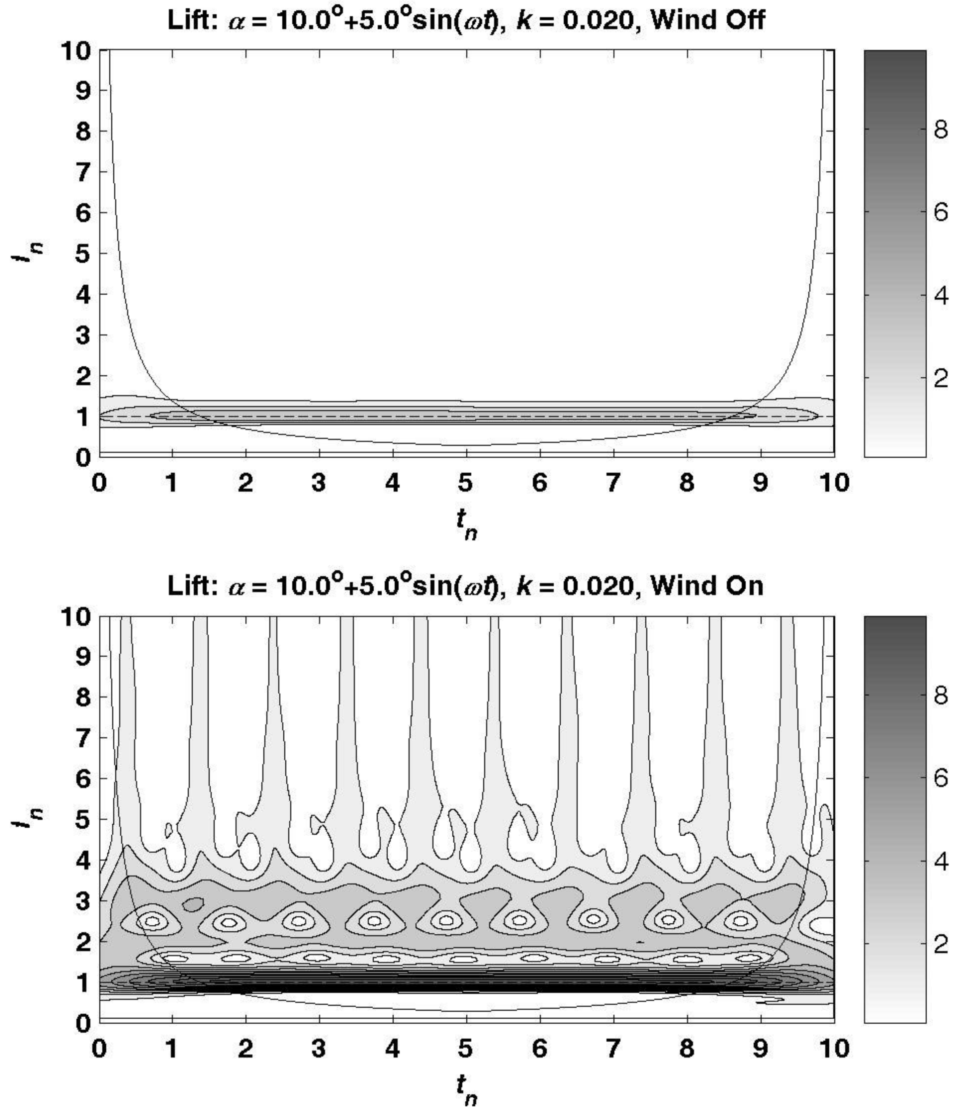

Figure 4.7 Spectrograms of lift under wind-off and wind-on conditions for Case 3 at k = 0.02.

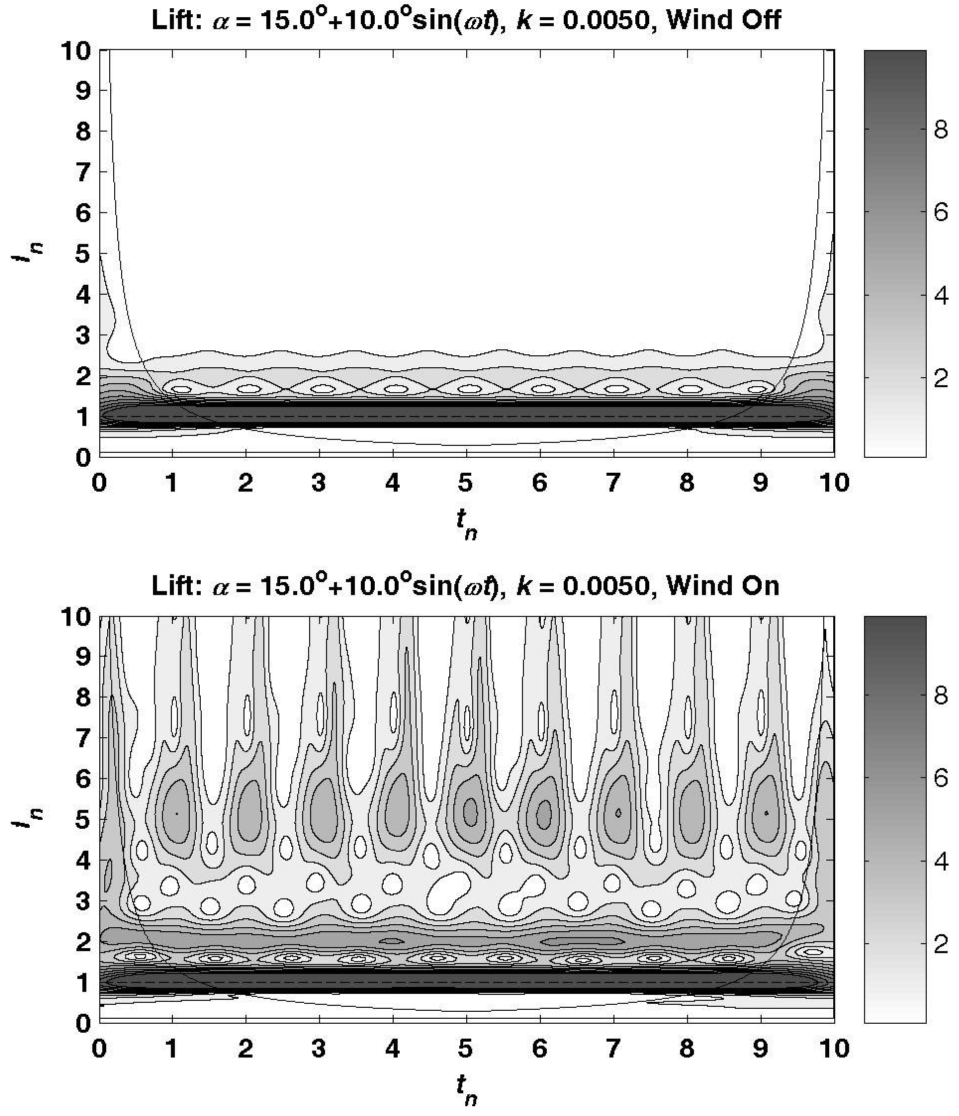

Figure 4.8 Spectrograms of lift under wind-off and wind-on conditions for Case 5 at *k* = 0.005.

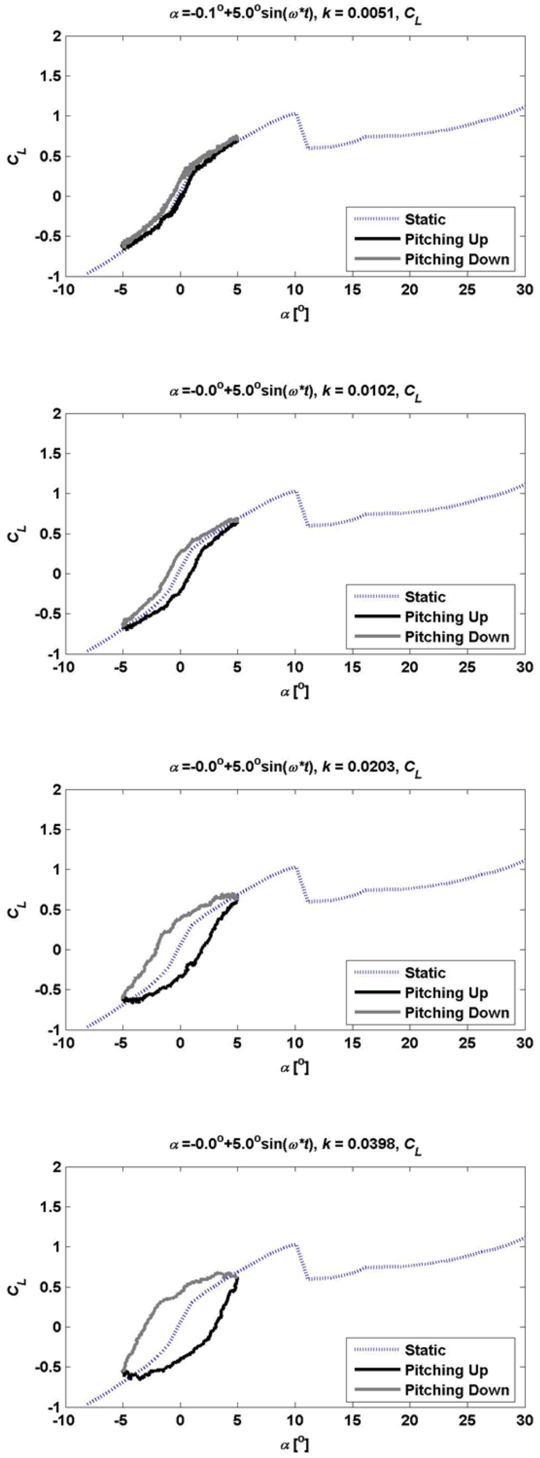

Figure 4.9 Phase-averaged lift curve for Case 1 at different *k*.

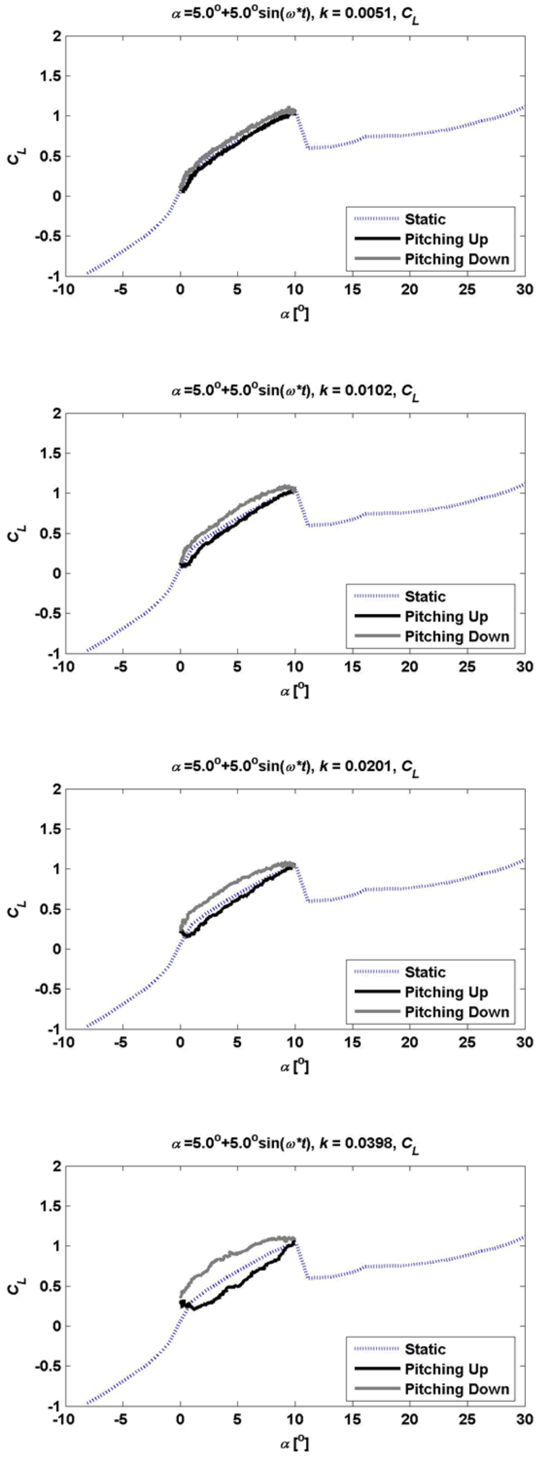

Figure 4.10 Phase-averaged lift curve for Case 2 at different *k*.

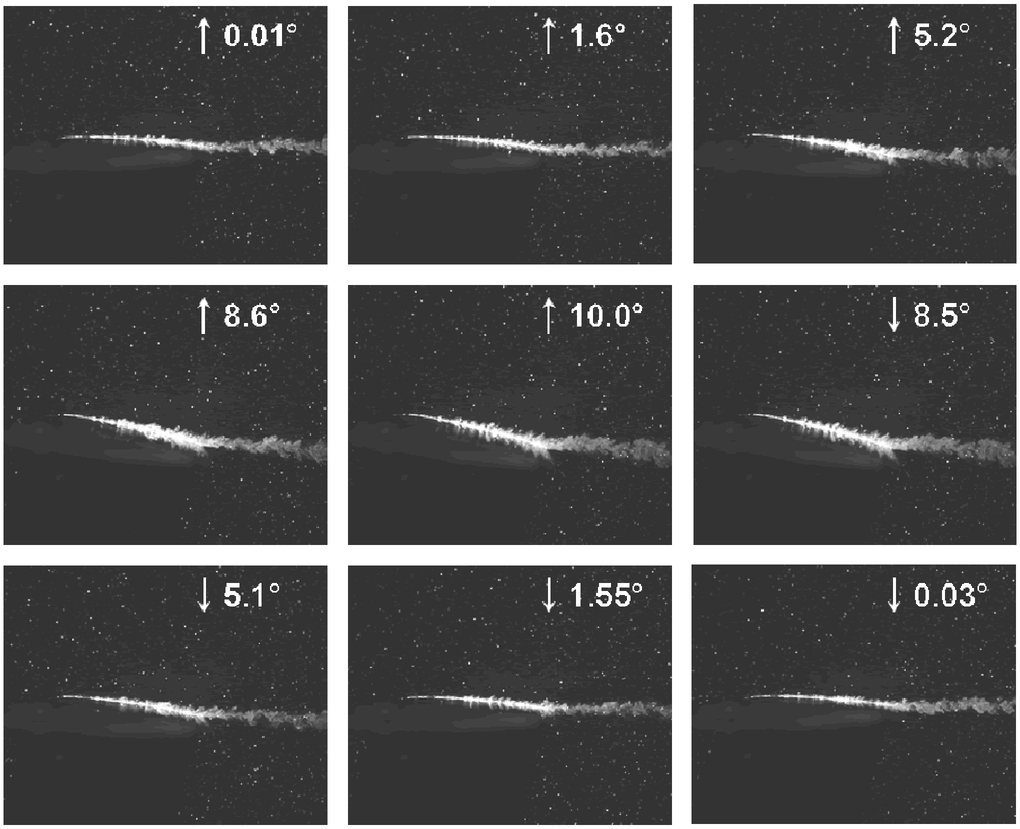

Figure 4.11 Visualization of flow around an oscillating airfoil for Case 2 at *k* = 0.04.

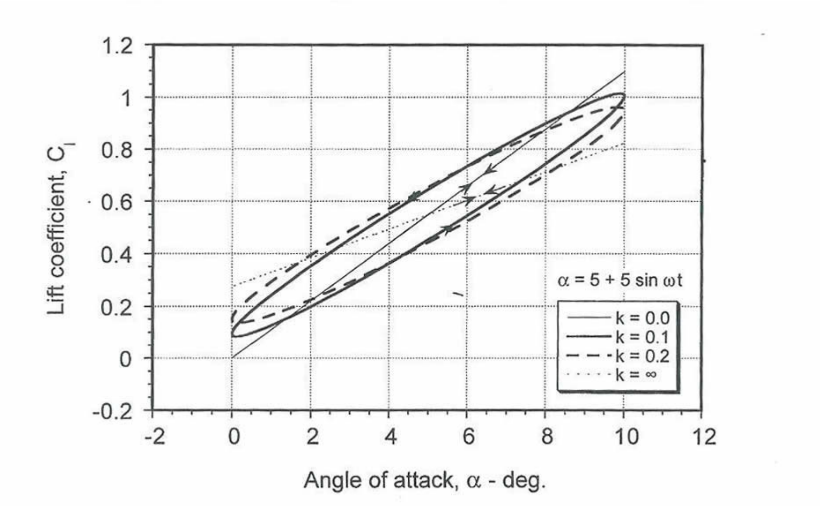

Figure 4.12 Lift hysteresis loop based on Theodorsen's model, courtesy of Leshiman (2000).

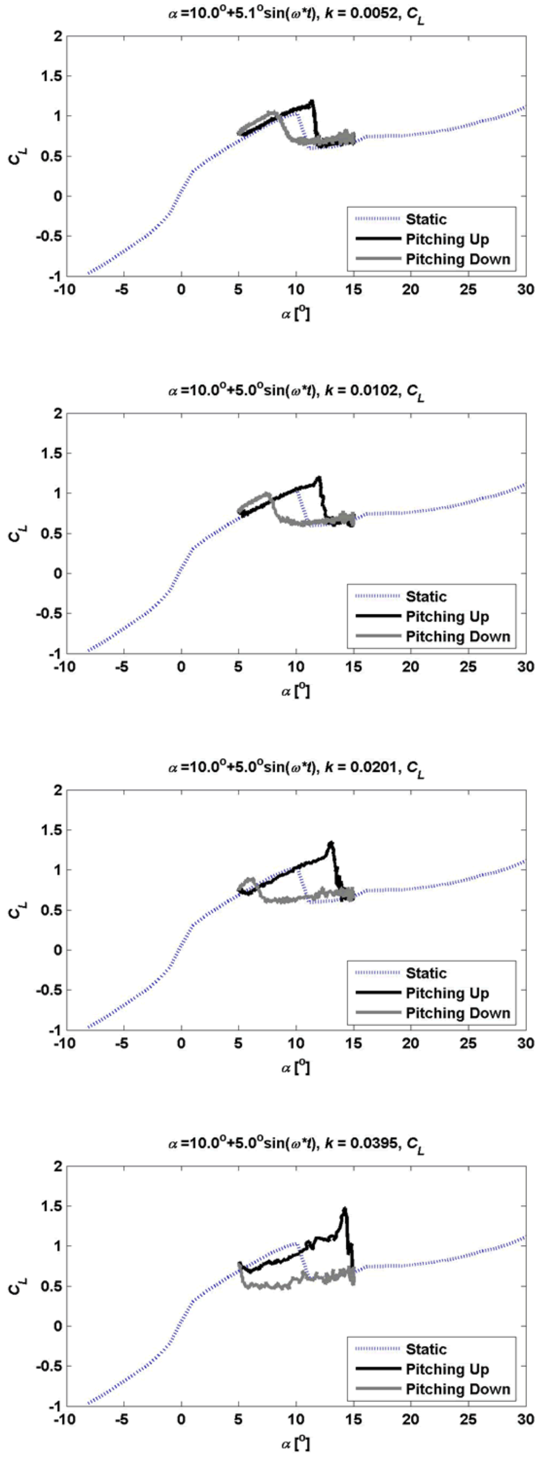

Figure 4.13 Phase-averaged lift curve for Case 3 at different *k*.

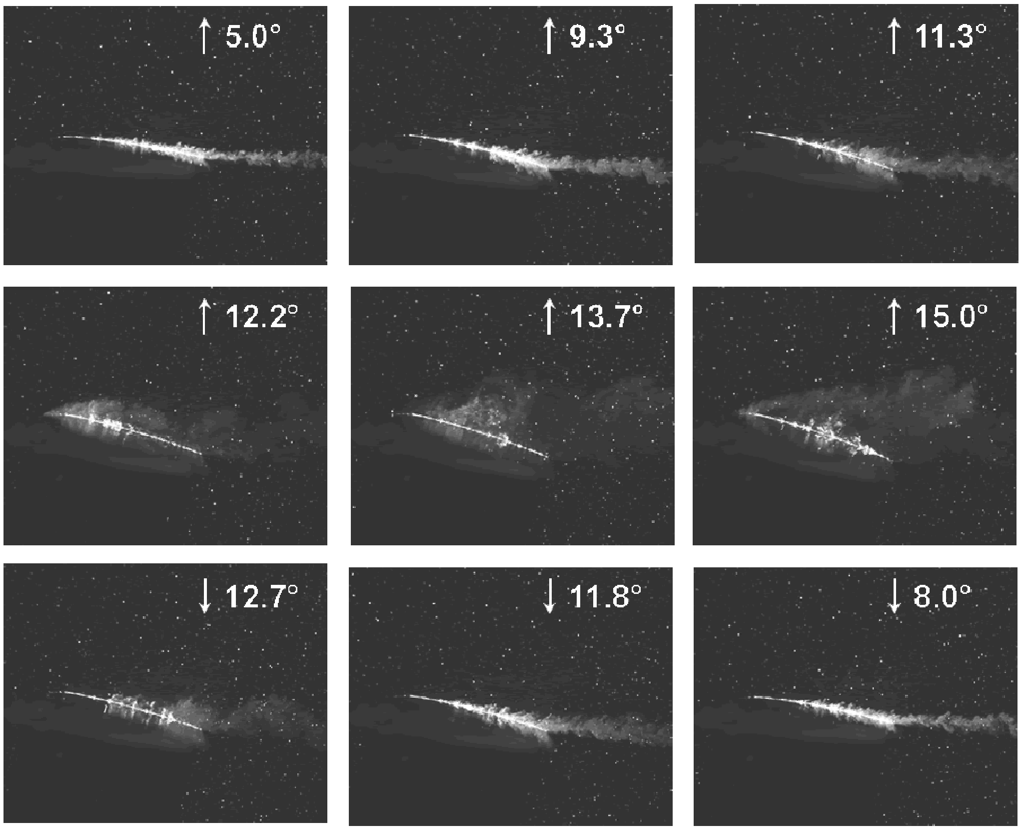

Figure 4.14 Visualization of flow around an oscillating airfoil for Case 3 at *k* = 0.005.

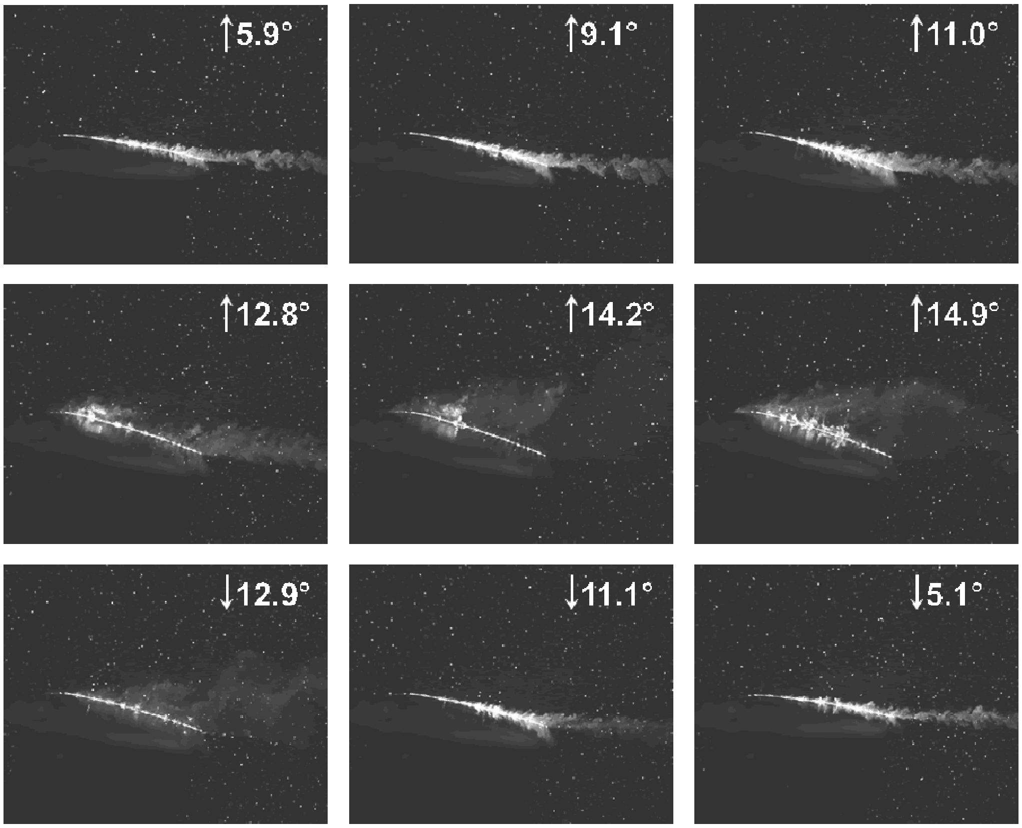

Figure 4.15 Visualization of flow around an oscillating airfoil for Case 3 at *k* = 0.04.

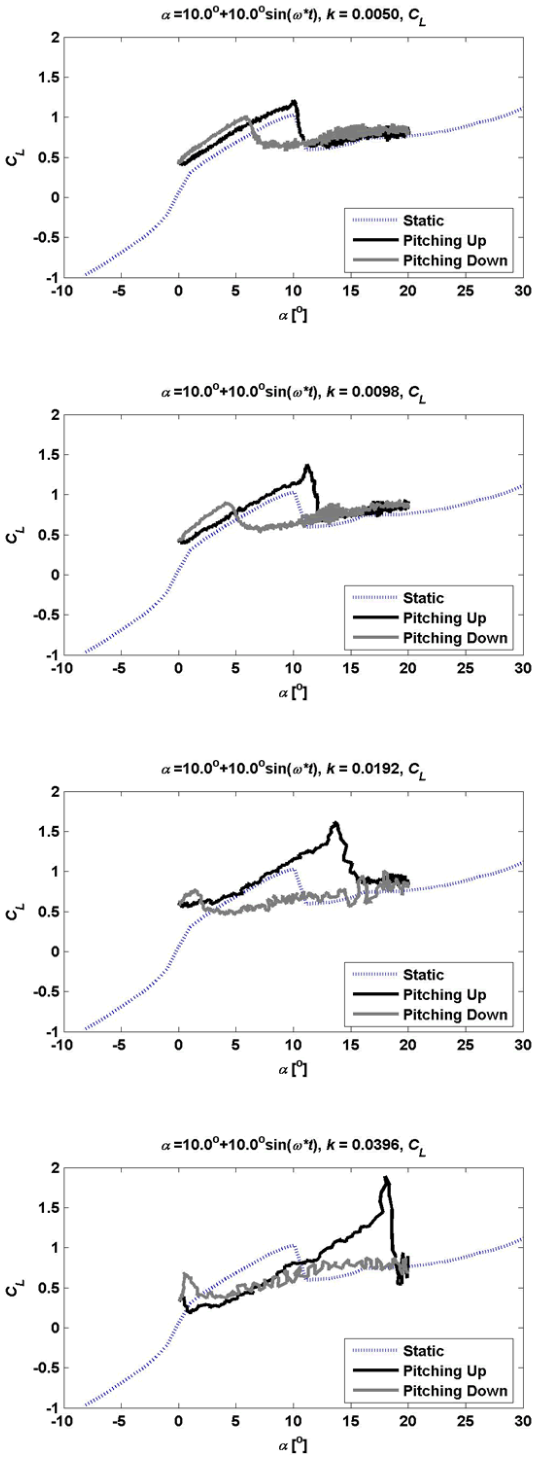

Figure 4.16 Phase-averaged lift curve for Case 4 at different *k*.

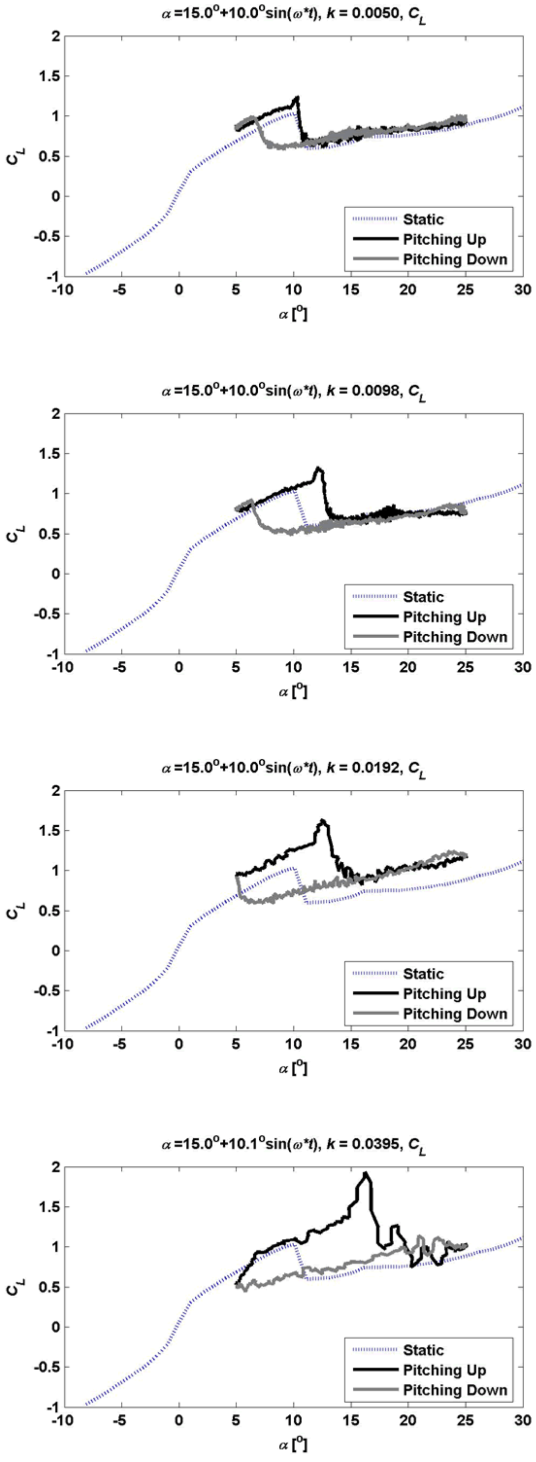

Figure 4.17 Phase-averaged lift curve for Case 5 at different *k*.

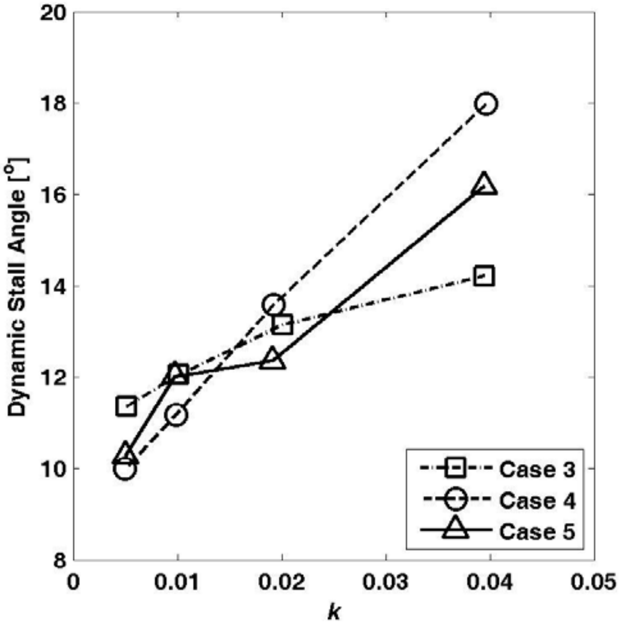

Figure 4.18 Stall angle as a function of reduced frequency *k*.

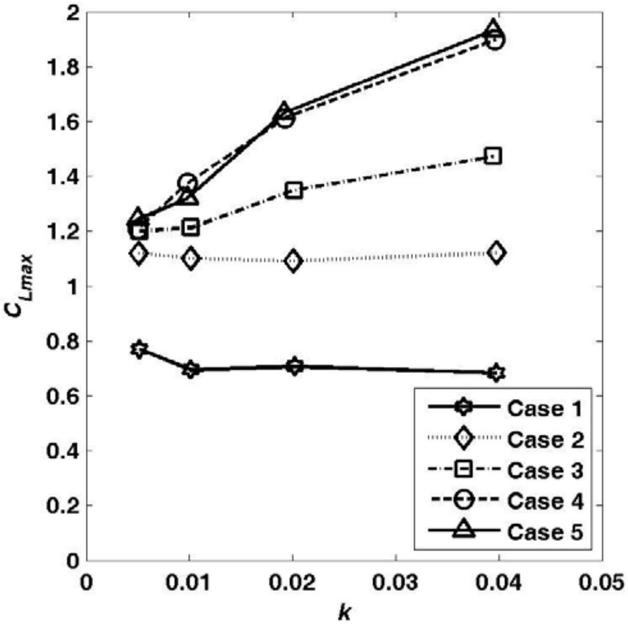

Figure 4.19 Maximum lift as a function of reduced frequency *k*.

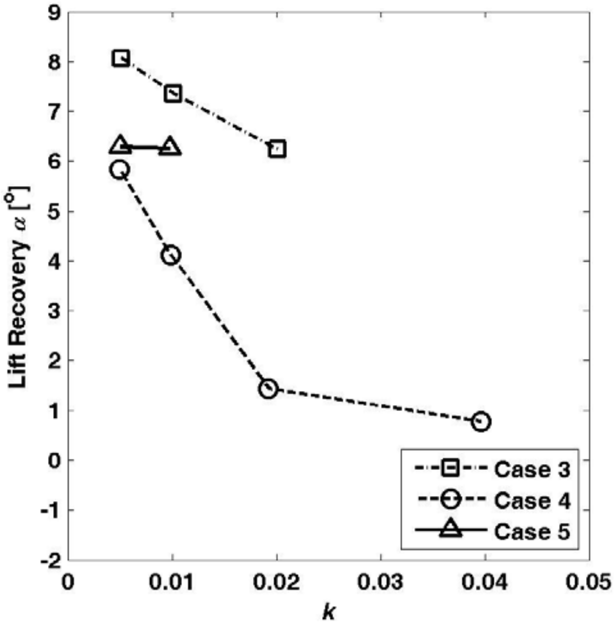

Figure 4.20 Lift recovery angle as a function of reduced frequency *k*.

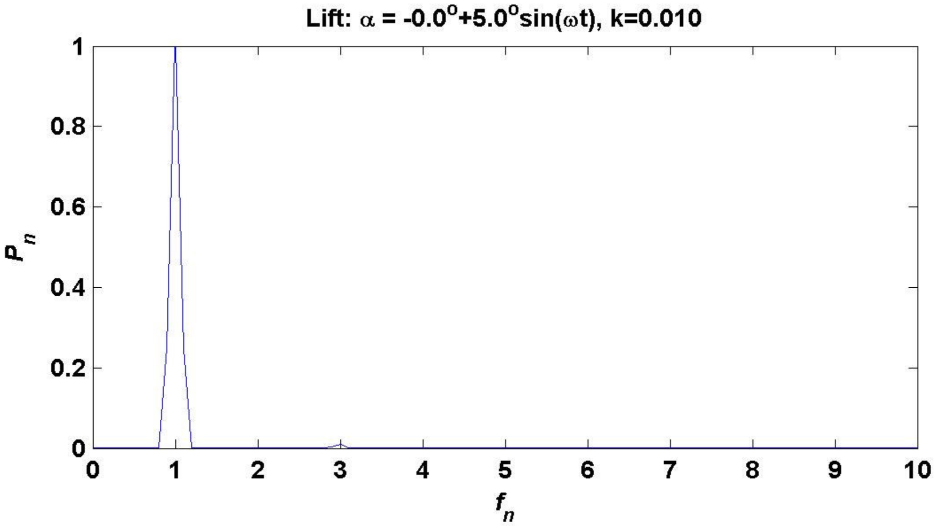

Figure 4.21 FFT-based power spectral density for Case 1 at *k* = 0.01.

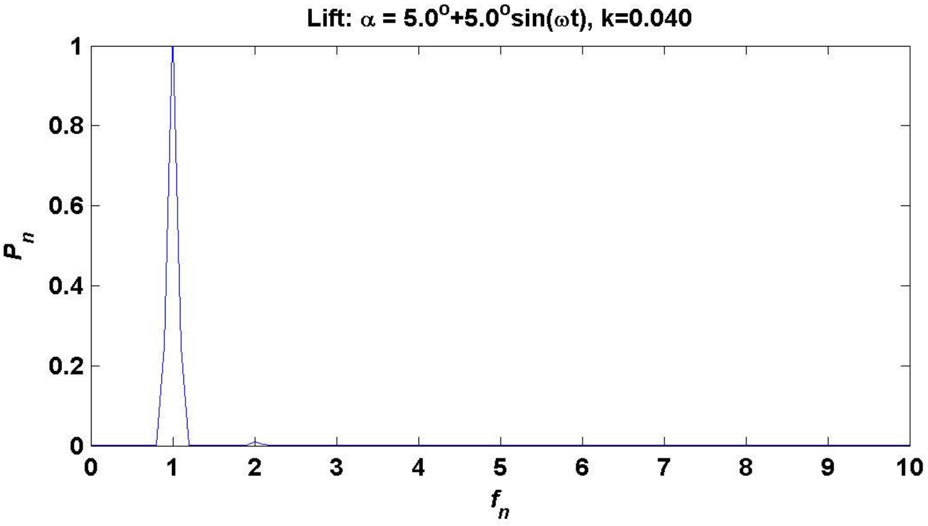

Figure 4.22 FFT-based power spectral density for Case 2 at *k* = 0.04.

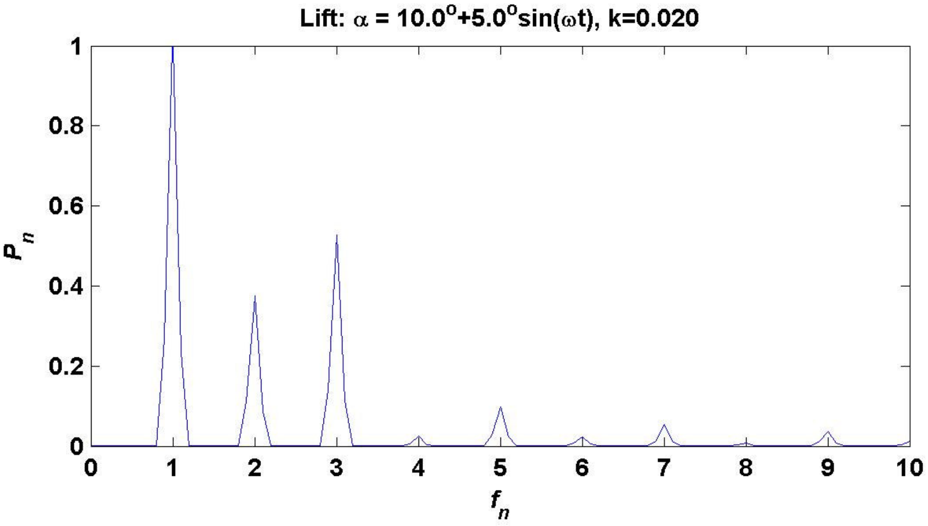

Figure 4.23 FFT-based power spectral density for Case 3 at *k* = 0.02.

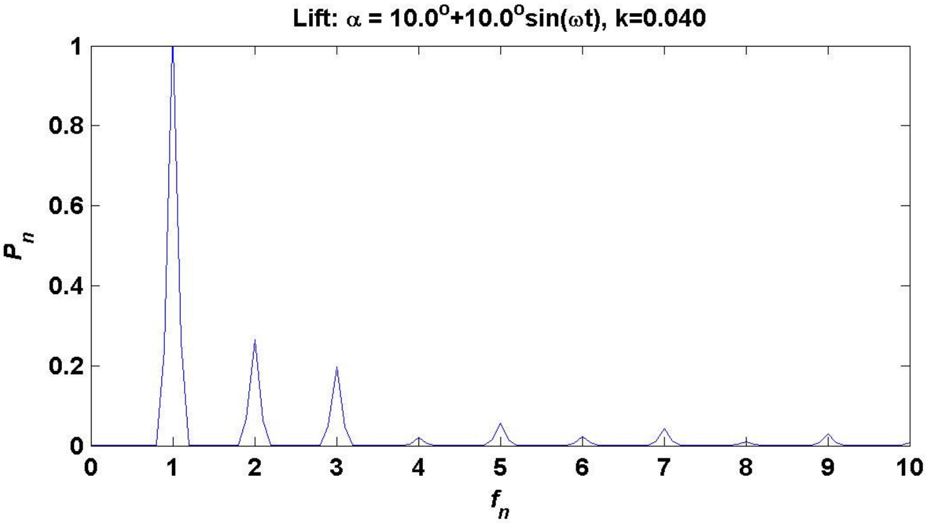

Figure 4.24 FFT-based power spectral density for Case 4 at *k* = 0.04.

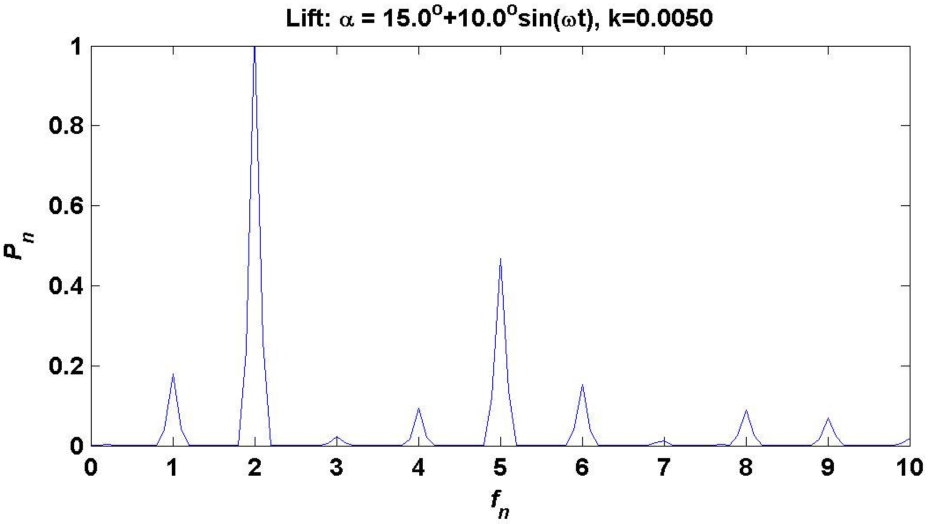

Figure 4.25 FFT-based power spectral density for Case 5 at *k* = 0.005.

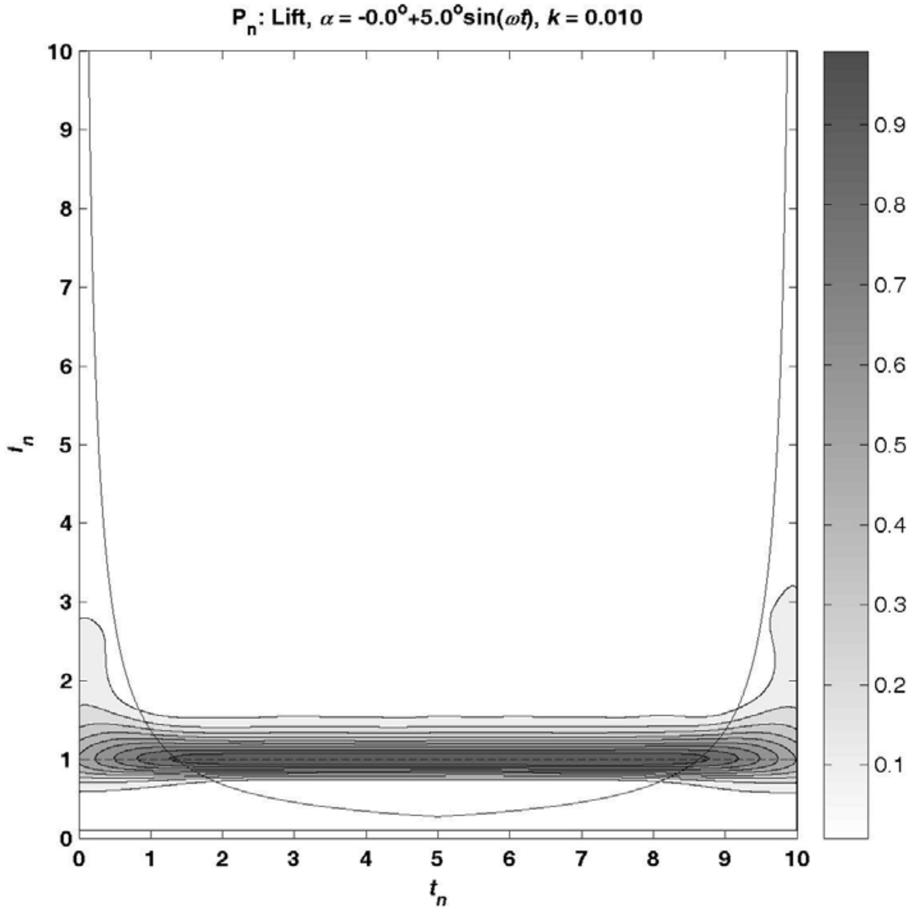

Figure 4.26 Spectrogram of the wavelet analysis of the lift time series for Case 1 at *k* = 0.01.

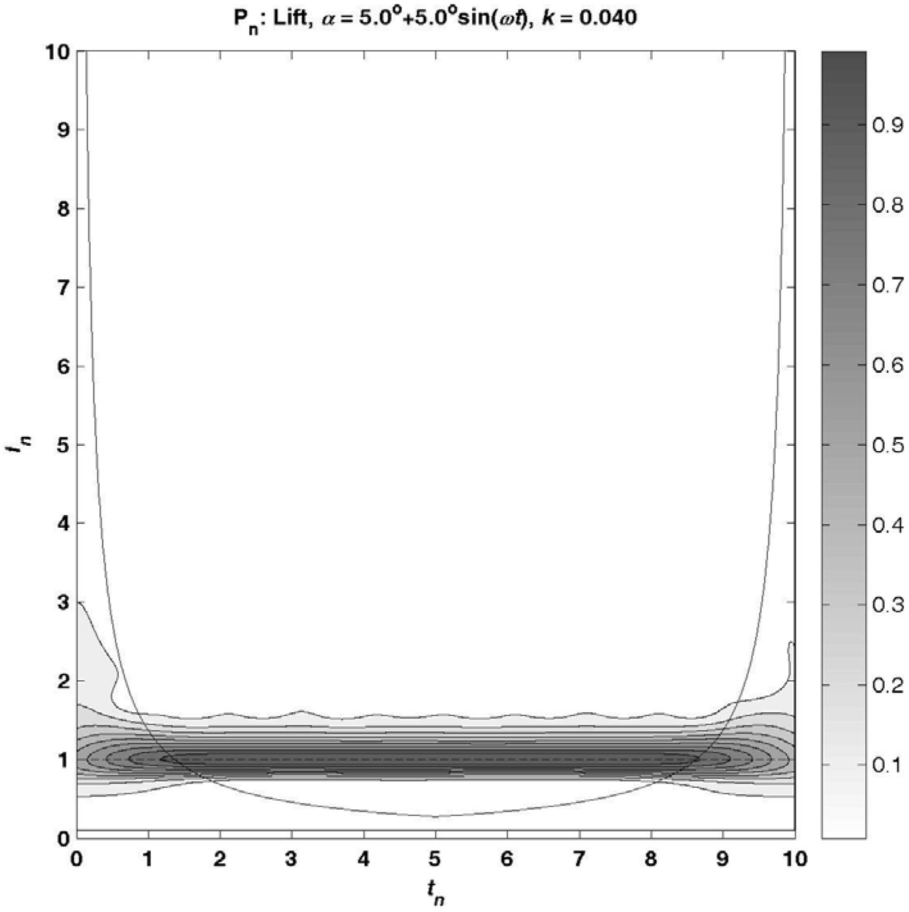

Figure 4.27 Spectrogram of the wavelet analysis of the lift time series for Case 2 at *k* = 0.04.

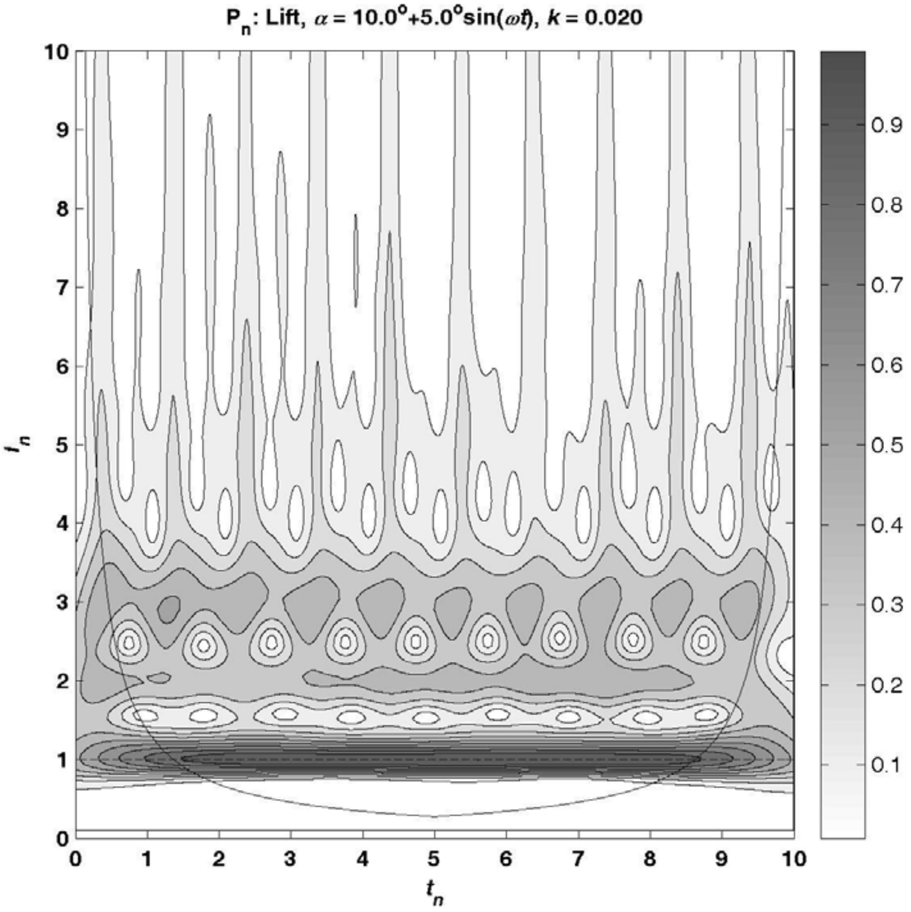

Figure 4.28 Spectrogram of the wavelet analysis of the lift time series for Case 3 at *k* = 0.02.

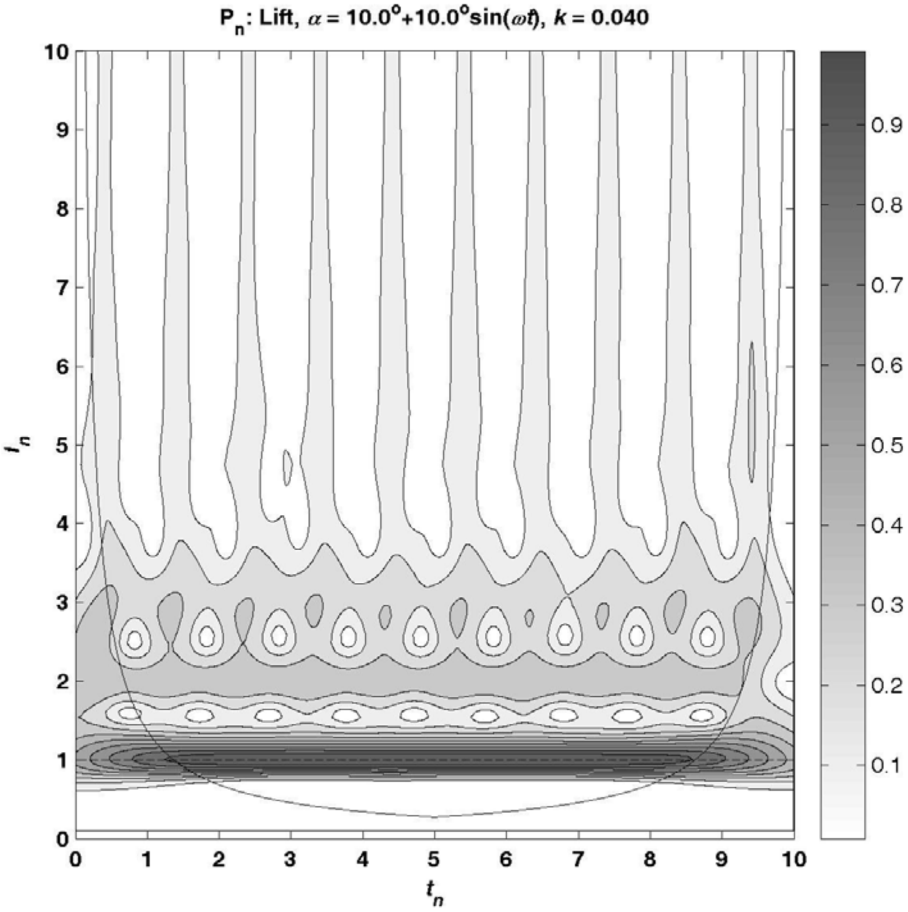

Figure 4.29 Spectrogram of the wavelet analysis of the lift time series for Case 4 at *k* = 0.04.

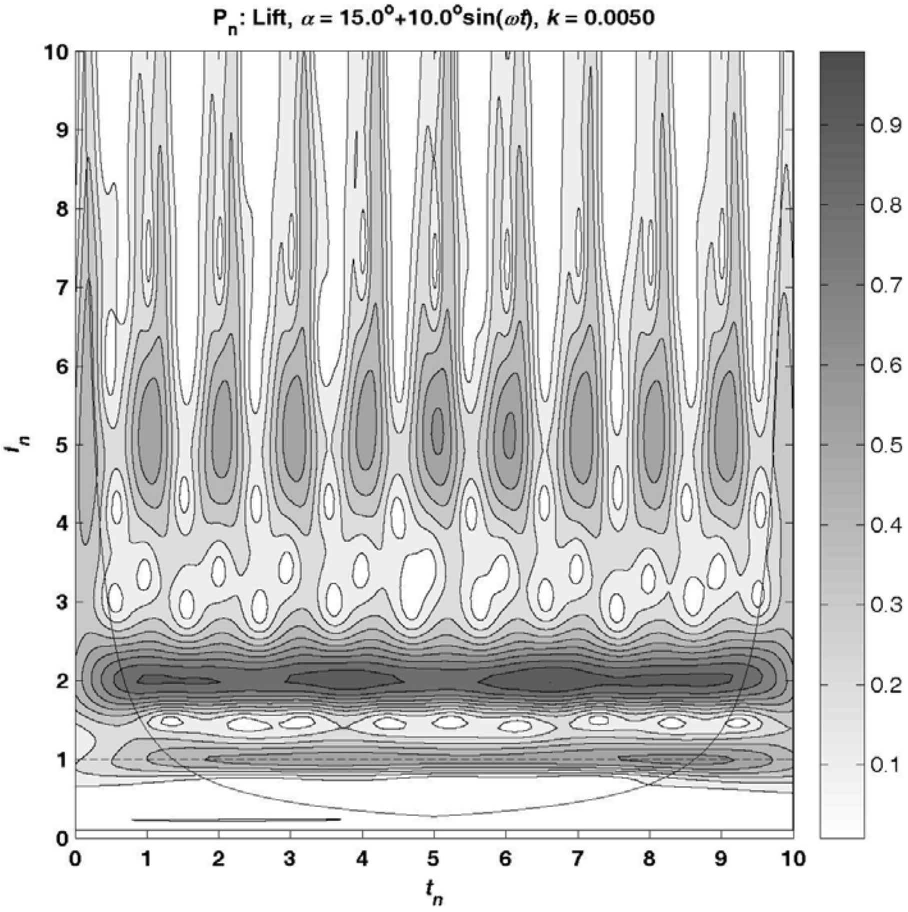

Figure 4.30 Spectrogram of the wavelet analysis of the lift time series for Case 5 at *k* = 0.005.

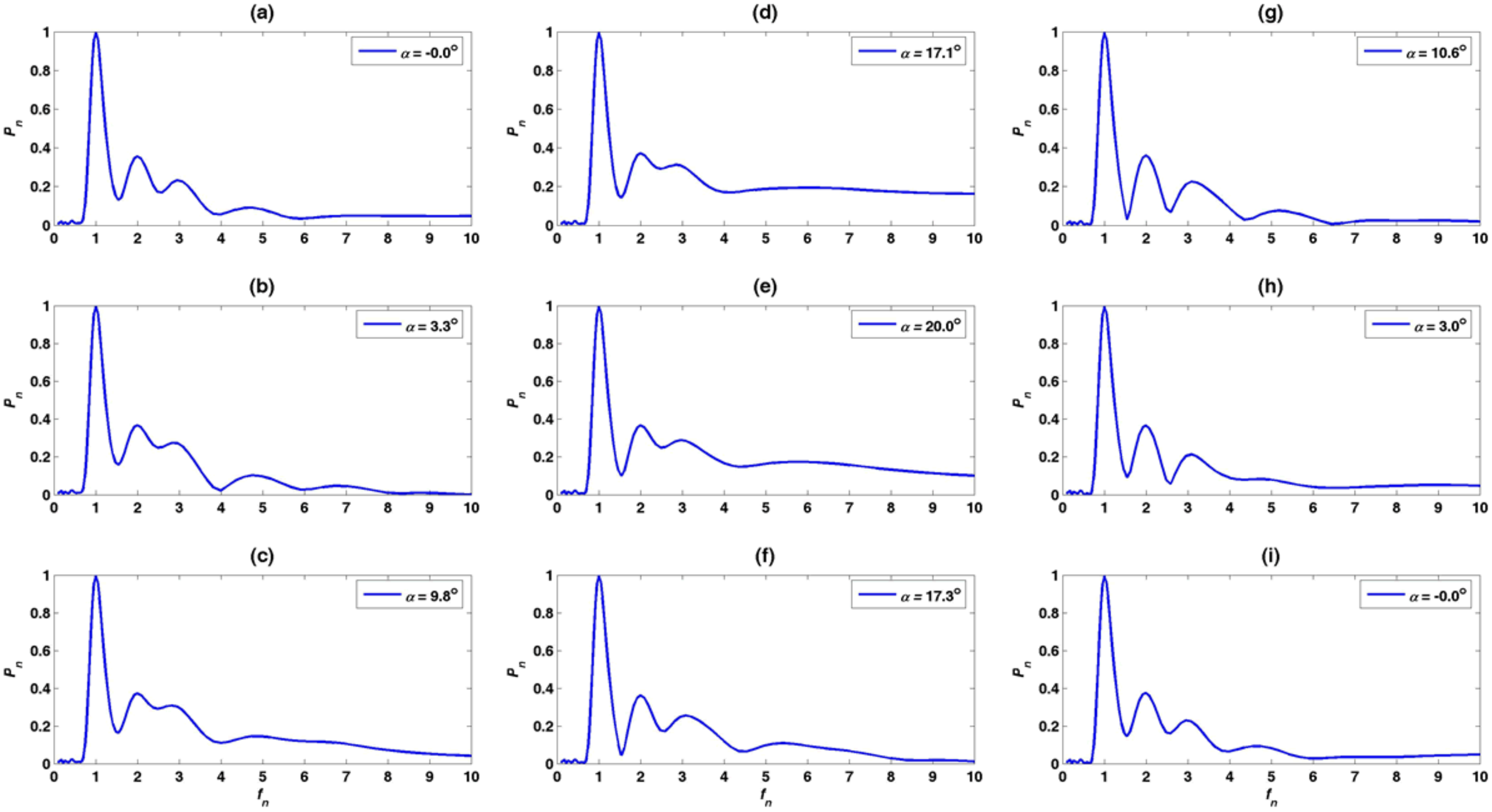

Figure 4.31 Power spectra at selected times for Case 4 at *k* = 0.04.

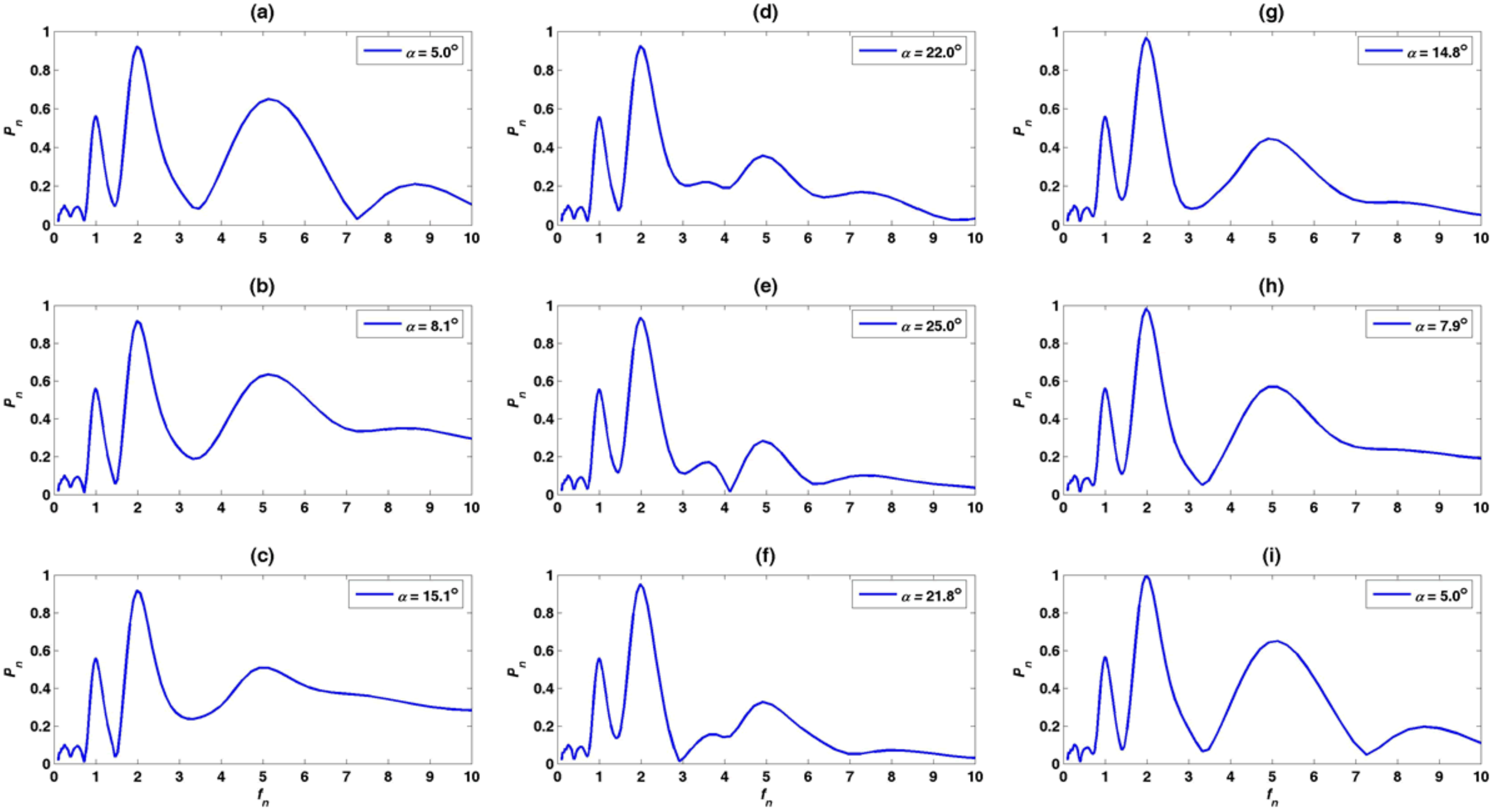

Figure 4.32 Power spectra at selected times for Case 5 at *k* = 0.005.

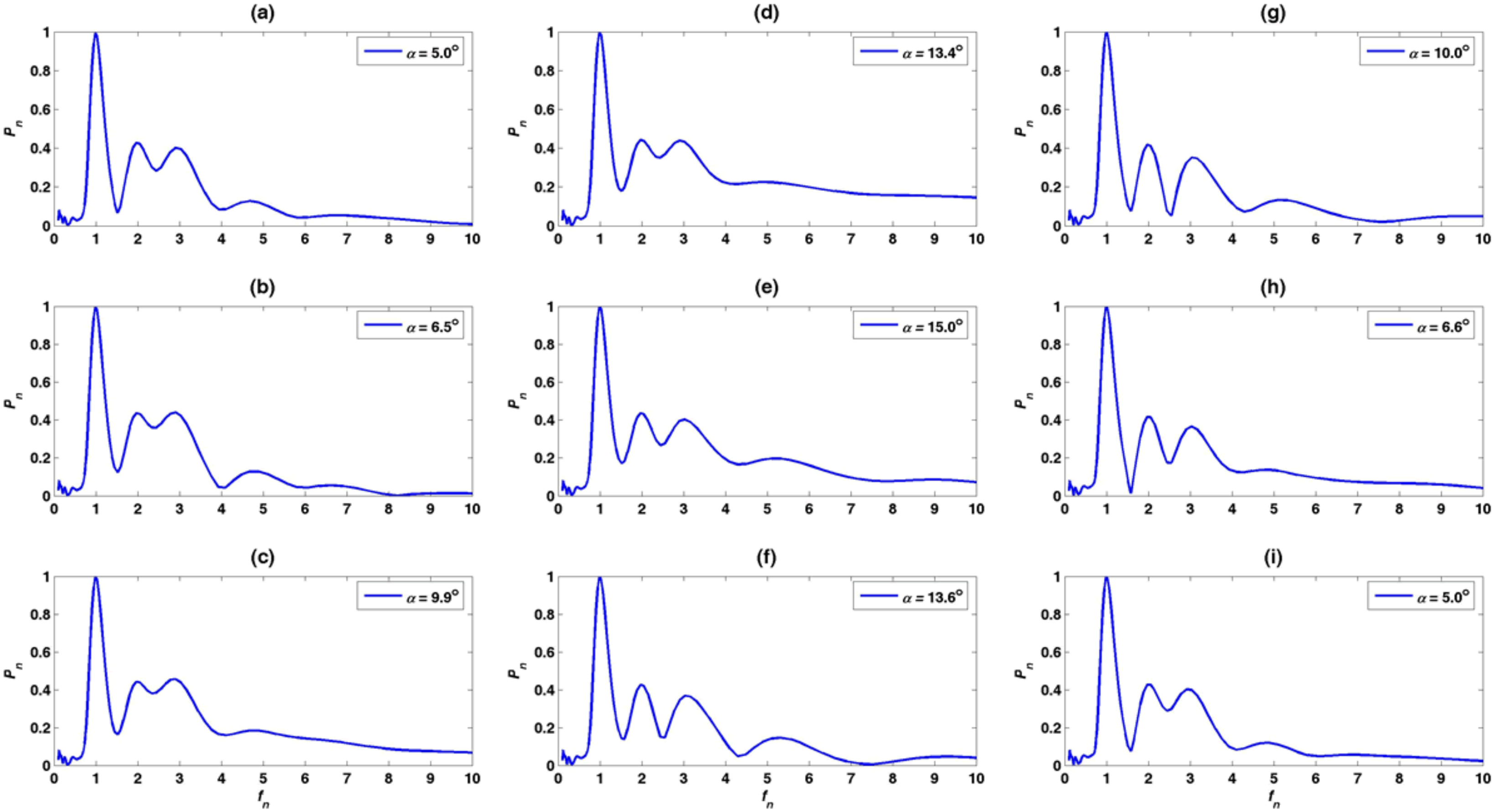

Figure 4.33 Power spectra at selected times for Case 3 at *k* = 0.02.

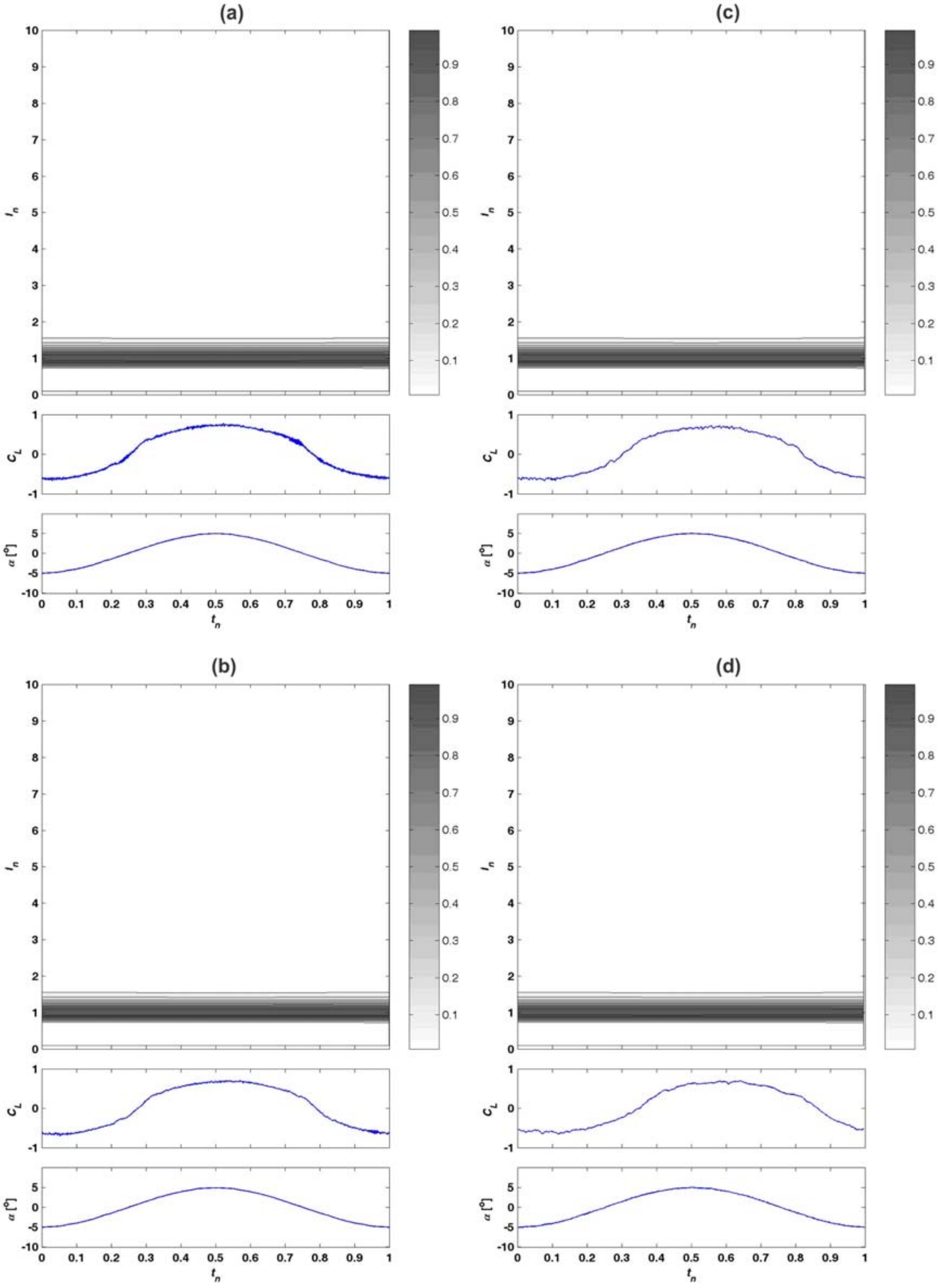

Figure 4.34 Spectrogram, C_L and α variation with t_n within one of oscillation for Case 1 at various k: (a) k = 0.005 (b) k = 0.01 (c) k = 0.02 (d) k = 0.04

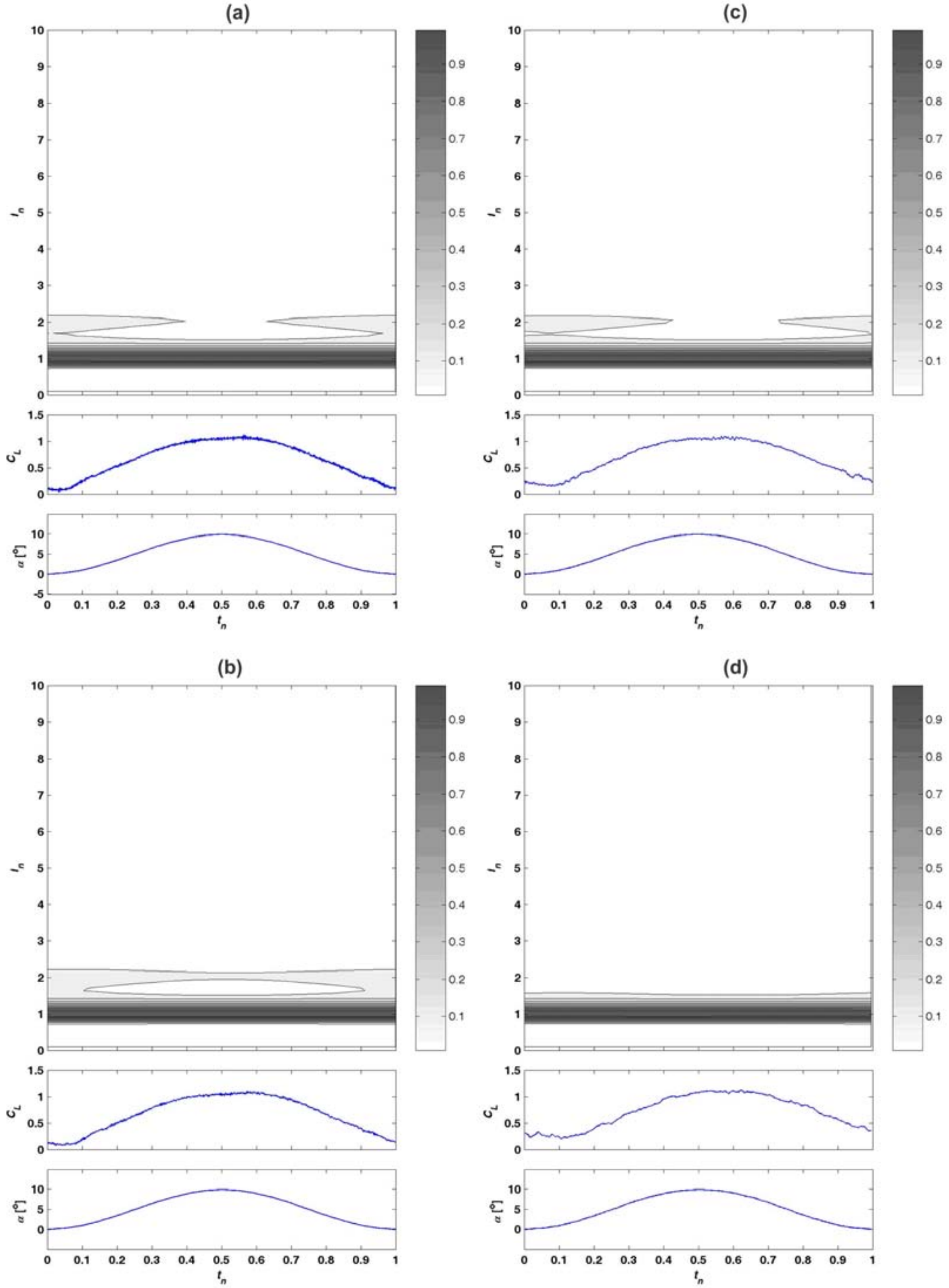

Figure 4.35 Spectrogram, C_L and α variation with t_n within one of oscillation for Case 2 at various k: (a) $k = 0.005$ (b) $k = 0.01$ (c) $k = 0.02$ (d) $k = 0.04$

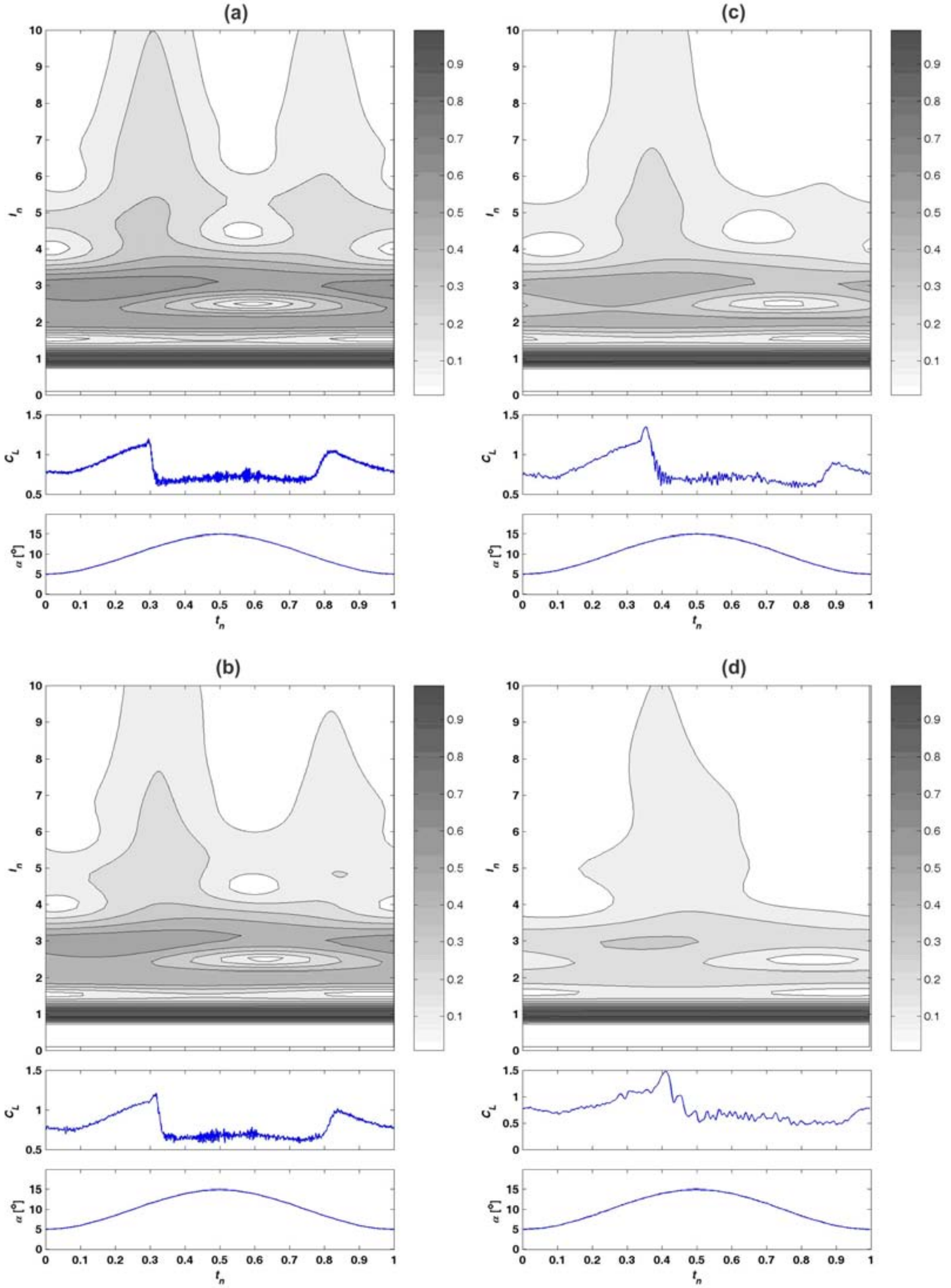

Figure 4.36 Spectrogram, C_L and α variation with t_n within one of oscillation for Case 3 at various k: (a) $k = 0.005$ (b) $k = 0.01$ (c) $k = 0.02$ (d) $k = 0.04$

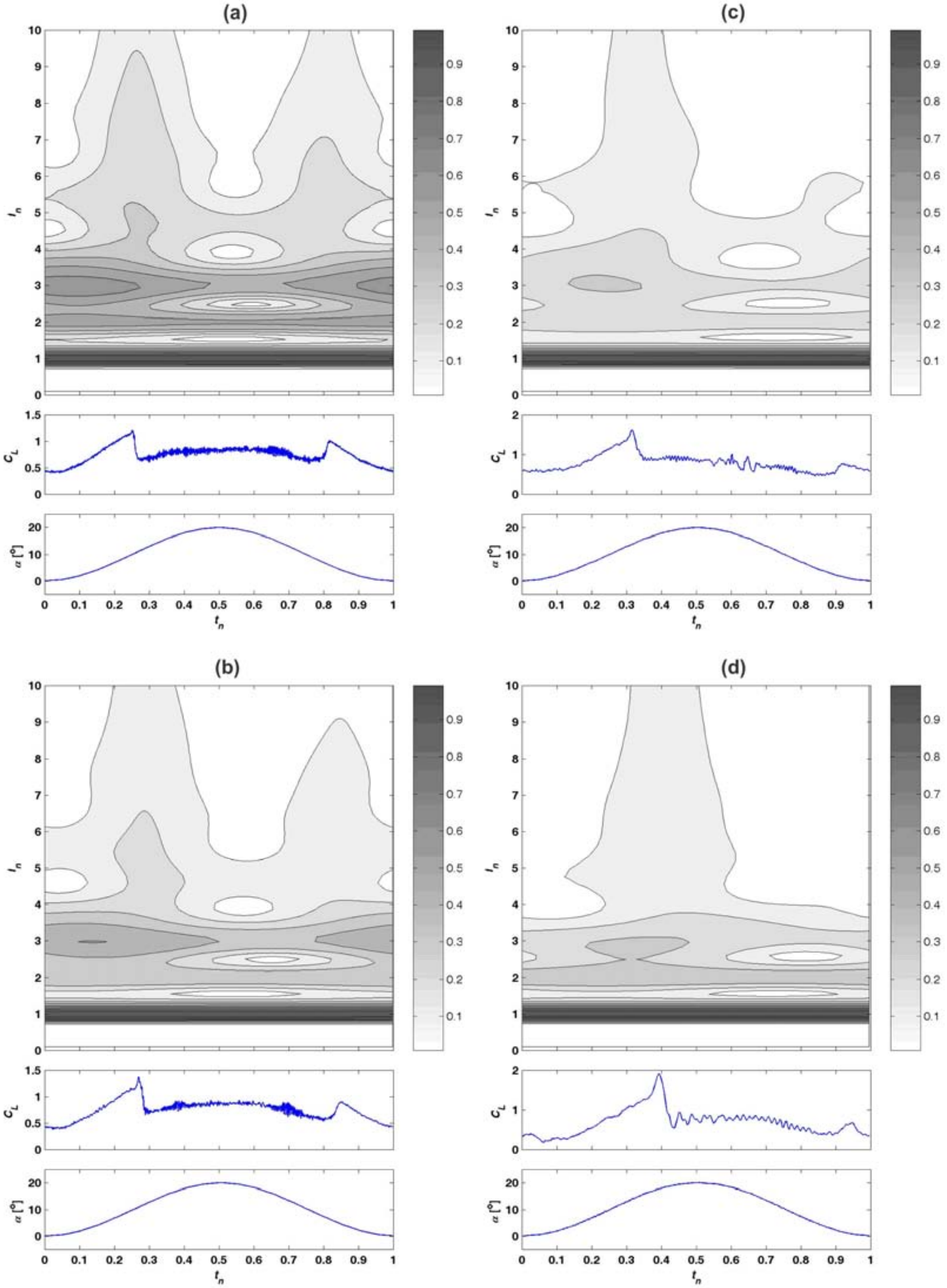

Figure 4.37 Spectrogram, C_L and α variation with t_n within one of oscillation for Case 4 at various k: (a) k = 0.005 (b) k = 0.01 (c) k = 0.02 (d) k = 0.04

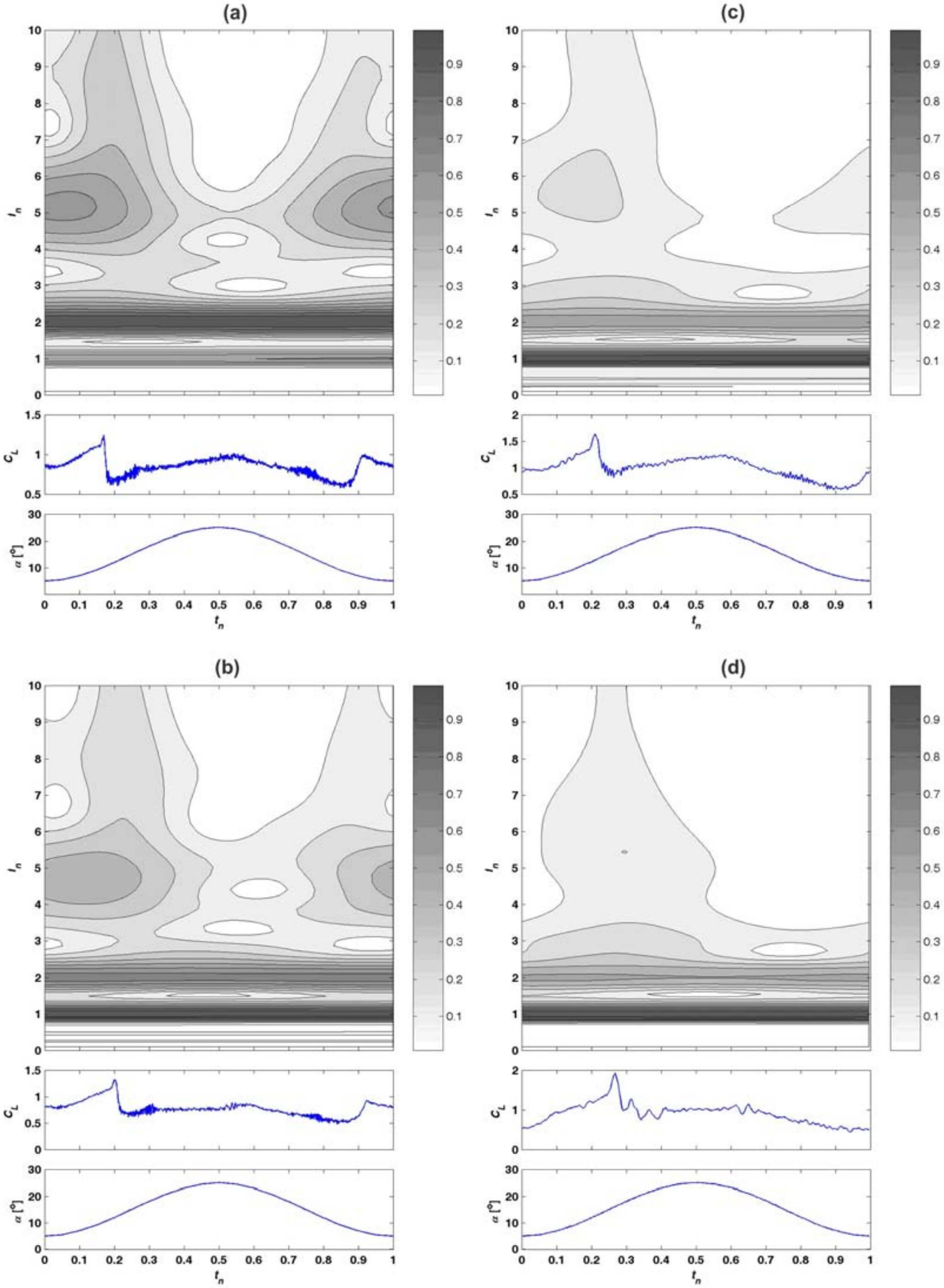

Figure 4.38 Spectrogram, C_L and α variation with t_n within one of oscillation for Case 5 at various k: (a) k = 0.005 (b) k = 0.01 (c) k = 0.02 (d) k = 0.04

CHAPTER 5 CONCLUSIONS AND FUTURE WORK

Dynamic stall occurs when an airfoil undergoes a rapid increase in the angle of attack. Large overshoots in lift, drag, and pitch moment take place and are followed by abrupt lift and moment stall. There is interest in making use of these large excursions of maximum lift to improve maneuverability of aircraft. However, the large air load associated with dynamic stall can cause severe structural damages to the aircraft. In view of this, an understanding of the characteristics of dynamic stall is necessary. The present study examines the frequency content of the unsteady lift signals in order to study the stationary nature of the aerodynamic responses of the pitching airfoil. In order to preserve the important information concerning the behavior of the fluctuating force as well as the high frequency components in the measured signals, a direct force measurement technique is used to better capture the actual aerodynamic responses of the test model.

In this chapter, conclusions are made on the direct force measurement technique and the measured lift signals of an airfoil undergoing dynamic stall. Effects of reduced frequency, mean angle, and amplitude of pitching motion on the stall process, and power spectra analysis of the lift measurements, as well as the nonstationary and nonlinear nature of the lift signals are summarized. Finally, suggestions on further work are stated.

5.1 Conclusions

5.1.1 Direct Force Measurement

A direct force measurement technique using piezoelectric load cells has been used to study the physics of dynamic stall at Re = $7.7\text{x}10^4$. It could be used in wind tunnel testing of a pitched airfoil undergoing periodic pitching oscillation and dynamic stall. In this study, the mean angle of pitching oscillation varies from 0° to 15° and the pitching amplitude is as large as 10°.

The static stall angle α_{ss} is determined to be 10° and the slope of the lift curve is found to be 2π. The measured α_{ss} is lower than that reported in the literature; however, the lower value is a consequence of early separation of the flow from the suction surface of the airfoil. Flow visualization provides supporting evidence to corroborate this conclusion.

Dynamic stall is created by pitching the airfoil at specified pitching reduced frequencies k, amplitude of pitching motion α_{amp}, and the mean pitching angle α_{mean}. Altogether, five different cases with four values k ranging from 0.005 to 0.04 are investigated. These five cases are chosen to cover pre-stall, light-stall, and deep-stall behavior. At least two of the five cases investigated have the same α_{mean} but different α_{amp}, and another two have the same α_{amp} but different α_{mean}. This way, the effects of k, α_{amp} and α_{mean} can be studied. It is found that the dynamic stall angle is significantly affected by k, so is the maximum lift coefficient C_{Lmax}. The dynamic stall angle increases with k but the effect for light-stall is much milder compared to deep-stall. Similar effect is also observed for C_{Lmax}; however k essentially has no effect on C_{Lmax}

in the pre-stall regime. Lift recovery from dynamic stall is delayed by increasing *k*. While in some cases at higher *k*, C_L fails to recover during down-stroke. On the other hand, α_{mean} has a slight effect on the dynamic stall angle but has little or no effect on C_{Lmax}, while α_{amp} has an effect on both the dynamic stall angle and C_{Lmax}. Both α_{amp} and α_{mean} have an effect on lift recovery.

5.1.2 Power Spectral Analysis

Power spectral analysis using FFT and CWT techniques has been carried out on the lift force signals. The power spectrum of both FFT and CWT of the pre-stall lift signal displays one single peak without other higher harmonics. Power spectrum of CWT also shows that the magnitude of the peak remains unchanged with time and this behavior is not affected by *k*. This single peak behavior indicates that the pre-stall lift is essentially stationary and linear. This spectral behavior progresses to one that exhibits multiple peaks in the light stall case shown by both FFT and CWT power spectrum. But CWT power spectrum is also able to show that, for the stall cases, the peaks and the associated power vary with time with concomitant transfer between frequencies. The variation pattern differs from one *k* to the next and from one stall case to another. Bands of higher power at higher frequencies occur when there is a surge of lift during a cycle and disappear when lift stalls, which indicates that energy is transferred between frequencies. The spectrograms deduced from CWT analysis show that the lift signal exhibits nonstationary and nonlinear behavior, and the nonstationarity and nonlinearity increase from light stall to deep stall.

5.2 Suggestions on Future Work

The direct force measurement technique used in the present study is proven to be viable to capture the frequency content of the lift signals, thus it is suggested that other parameters affecting the dynamic stall process, such as different airfoil profile, Reynolds number effect, as well as structural stiffness of the airfoil, should be investigated utilizing the same technique. By carrying out wavelet analysis, the nonstationary/nonlinear nature of dynamic stall associated with these parameters can be studied.

Wavelet analysis performed in this study shows clearly the nonstationary/nonlinear behavior of the lift signals of an airfoil undergoing dynamic stall. However, the underlying physics involved remain unknown. Hence, further investigations are suggested on the nonlinearity and the flow physics of the dynamic stall process.

REFERENCES

Albertson, J. A., Troutt, T. R., Siuru, W. D. and Walker, J. M. 1987 Dynamic stall vortex development and the surface pressure field of a pitching airfoil. *AIAA Paper 87-1333.*

Baban, F. and So, R. M. C., 1991 Recirculating flow behind and unsteady forces on finite-span circular cylinders in a cross-flow. *Journal of Fluids and Structures*, 5, 185–206.

Baban, F., So, R. M. C. and Otügen, M. V. 1989 Unsteady forces on circular cylinders in a cross-flow. *Experiments in Fluids*, 7, 293-302.

Carr, L. W. 1998 Progress in analysis and prediction of dynamic stall. *Journal of Aircraft*, 25(1), 6-17.

Carr, L. W., McAlister, K. W., and McCroskey, W. J. 1977 Analysis of the development of dynamic stall based on oscillating airfoil experiments. *NASA TN D-8382*.

Conger, R. N., and Ramaprian, B. R. 1994 Pressure measurements on a pitching airfoil in a water channel. *AIAA Journal*, 32(1), 108-115.

Dickinson, M. H., Lehmann, F.-O., and Sane, S. P. 1999 Wing rotation and the aerodynamic basis of insect flight. *Science*, 284, 1954-1960.

Farge, M. 1992 Wavelet transforms and their applications to turbulence. *Annual Review of Fluid Mechanics*, 24, 395–457.

Lam, K., Li, J. Y. and So, R. M. C. 2003 Force coefficient and Strouhal number of four cylinders in cross flow. *Journal of Fluids and Structures*, 18, 305-324.

Lam, K., Wang, F. H., Li, J. Y. and So, R. M. C. 2004 Experimental investigation of the mean and fluctuating forces of wavy cylinders in a cross-flow. *Journal of Fluids and Structures*, 19, 321-334.

Lau, Y. L., So, R. M. C. and Leung, R. C. K. 2004 Flow-induced vibration of elastic slender structures in a cylinder wake. *Journal of Fluids and Structures*, 19, 1061-1083.

Leishman, J. G. 2000 *Principles of Helicopter Aerodynamics*. Cambridge: Cambridge University Press.

Martin, J. M., Empey, R. W., McCroskey, W. J., and Caradonna, F. X. 1974 An experimental analysis of dynamic stall on an oscillating airfoil. *Journal of American Helicopter Society*, 19, 26-32

Mary, I., and Sagaut, P. 2002 Large Eddy Simulation of Flow around an Airfoil near Stall. *AIAA Journal*, 40, 1139–1145.

McAlister, K. W., Carr, L. W, and McCroskey, W. J. 1978 Dynamic stall experiments on the NACA 0012 airfoil. *NASA TP 100*.

Oshima, H., and Ramaprian, B. R. 1992 Measurements of the velocity and vorticity fields around a pitching airfoil. *AIAA Paper 92-2626*.

Panda, J. and Zaman, K. B. M. Q. 1994 Experimental investigation of the flowfield of an oscillating airfoil and estimation of lift from wake surveys. *Journal of Fluid Mechanics*, 265, 65-95.

Piziali, R. A. 1994 2-D and 3-D oscillating wing aerodynamics for a range of angles of attack including stall. *NASA Technical Memorandum 4632*.

Richter A. and Naudescher, E. 1976 Fluctuating forces on a rigid circular cylinder in confined flow. *Journal of Fluid Mechanics*, 78, 561-576.

Savkar, S. D., So, R. M. C. and Listzinger, T. A. 1980 Fluctuating Lift and Drag Forces Induced on Large Span Bluff Bodies in a Turbulent Crossflow. ASME HTD-9, 19-26.

Sin, V. K. and So, R. M. C. 1987 Local force measurements on finite-span cylinders in a cross-flow. *Journal of Fluids Engineering*, 109, 136-143.

So, R. M. C. and Savkar, S. D. 1981 Buffeting forces on rigid circular cylinders in cross flows. *Journal of Fluid Mechanics*, 105, 397-425.

So, R. M. C., Liu, Y., Cui, Z. X., Zhang, C. H. and Wang, X. Q. 2005 Three-dimensional wake effects on flow-induced forces. *Journal of Fluids and Structures*, 20, 373-402.

Torrence, C., and Combo, G. P. 1998 A practical guide to wavelet analysis. *Bulletin of the American Meteorological Society*, 79, 61-78

Walker, J. M., Helin, H. E., and Chou, D. C. 1985 Unsteady surface pressure measurements on a pitching airfoil. *AIAA Paper 85-0532*.

Wernert, P., Geissler, W., Raffel, M. and Kompenhans, J. 1996 Experimental and numerical investigations of dynamic stall on a pitching airfoil. *AIAA Journal*, 34(5), 982-989.

White, F.M. 1979 *Fluid Mechanics*. McGraw-Hill Book Company, New York, 499.

Zaman, K. B. M. Q., McKinzie, D. J. and Rumsey, C. L. 1989 A natural low-frequency oscillation of the flow over an airfoil near stalling conditions. *Journal of Fluid Mechanics*, 202, 403-442.